An NMR-compatible Bioartificial Liver for Metabolomic Investigation of Drug Action

Rex E. Jeffries

A dissertation submitted to the faculty of the University of North Carolina at Chapel Hill in partial fulfillment of the requirements for the degree of Doctor of Philosophy in the Department of Biomedical Engineering

Chapel Hill
2009

Approved by

Advisor: Jeffrey M. Macdonald, Ph.D.

Reader: Paul B. Watkins, M.D.

Reader: Oleg V. Favorov, Ph.D.

Reader: Michael P. Gamcsik, Ph.D.

Reader: Shawn Gomez, Ph.D.

Abstract

Rex E. Jeffries: An NMR-compatible Bioartificial Liver for Metabolomic Investigation of Drug Action
(Under the direction of Jeffrey M. Macdonald, Ph.D.)

NMR-compatible bioartificial liver (BAL) studies have been performed for thirty years and still have not been maintained beyond 8hrs. This doctoral work describes the engineering efforts in creating a long-term NMR-compatible BAL. Four general types of BALs have been reported: suspension, microcarrier, membrane, and entrapment. Reasons and efforts toward establishing a fluidized-bed entrapment bioreactor, which maintains hepatocytes entrapped in alginate for 30 hrs, and likely for long-term, are described. The electrostatically-encapsulated cells generate 1.5 mls of 500 μm diameter spherical encapsulates, containing about 10,000 cells each, in abou 5 minutes. These encapsultates containing entrapped cells are then incolulated into a 10 mm glass NMR tube and are percholate in the bottom of the glass tube forming the fluidized-bed.

To demonstrate the power of the NMR-compatible BAL in toxicity studies using in vivo 31P and 13C NMR spectroscopy, a rat hepatoma cell line, JM1, was used. The encapsulated cells were maintained overnite (16hrs) with 3-13C-cysteine and u-13C-glucose replaced in the perfused media, and production rates for glutathione, the body's primary antioxidant, and lactate, an anaerobic glycolytic end-product common in cancer, were determined. The next day (16-20 hrs) when [3-13C-cysteinyl]glutathione was at 13C isotopic steady-state and the JM1 cells were at metabolic steady-state, the effects of two doses of

bromobimane, a glutathione depleting agent, and three different doses of acetaminophen on the in vivo 31P and 13C NMR spectra were determined. The application of this time series data to toxicodyanamics and toxicokintetics is discussed. This is the first study demonstrating with 1 minute temporal resolution, the non-steady-state real-time toxicokinetics of glutathione.

Once the NMR-compatible BAL was demonstrated with a relatively easy liver cell-type to culture, a cell line (i.e., JM1), the fluidized-bed bioreactor was established with primary rat hepatocytes. Liver is exquisitely sensitive to oxygen tension and ranges from 8% to 3% across its capillary-bed, yet all previous NMR-compatible BAL studies have all gasified the perfusion media with 95% oxygen. Therefore, the effect of four oxygen concentrations (20%, 35%, 55%, and 95%) on viability was monitored by in vivo 31P NMR. Only the 35% and 55% oxygen treatments maintained hepatocytes viability for 28 hours and likely beyond with no change in ß-nucleotide triphosphate levels. Analysis of the in vivo 13C NMR data for the 55% oxygen treatment revealed synthetic rates for lactate and glutathione demonstrating differentiated functions were present and quantifying the function. This is the first demonstration of any primary hepatocyte culture being beyond 8 hrs in a NMR-compatible BAL.

Dedication

This work is dedicated to my wife, Sheronda, for her encouragement to pursue my dreams and for providing a constant example of what can be achieved through hard work and determination. I also dedicate this work to my wonderful children, Jacob and Lee, for being my little troopers throughout this journey and for their uplifting hugs and kisses that kept me going each day. Last, but not least, are my greatest supporters throughout my existence in this world, my parents, who instilled in me the manhood, scholarship, perseverance and uplift that enabled me to achieve this prestigious accomplishment.

Acknowledgements

This work could not have been achieved without the guidance and support I have received from so many exemplary academicians, laboratories, family, and friends. I would therefore like to thank the administrators Nancy McKinney, Sharon Womble, Harriett Brewer, Iris Holt and James Jordan for helping me with the 'How to' of graduate school. Thanks to the instructors, notably Oleg Favorov and Shawn Gomez, in the Department of Biomedical Engineering for teaching this old dog some new tricks. A special thanks to Greg Young of the UNC Biomolecular NMR Laboratory Core Facility for all of his assistance with my NMR experiments and more importantly, for his trust in allowing me to place the bioreactor in the magnet. Thanks to Michael Gamcsik for his apprenticeship in NMR-compatible bioreactor fabrication. Thanks to Ehkson Holmuhamedov of the Cell and Developmental Biology Imaging Facility for training on confocal microscopy. Thanks to Lee Graves in the Department of Pharmacology for use of his cell culture facilities. Special thanks to Andrey Tikunov for the oxygen sensor development and Peter Pediaditakis for the pathology instruction and numerous liver isolations. An especial thanks to Paul Watkins of the UNC General Clinical Research Center for believing in the research project, providing financial support, and tutelage in Hepatology. Huge thanks to my lab mates Chris Seagle, Jason Winnike, Justyna Wolak, Brian Dewar, Kayvan Keshari, and Haakil Lee for their friendship and assistance. Sincere thanks to my line brothers Kenneth Lewis, Isaac Green, Ellis Nunery, Charles Curry, Marquette Chester, David Snow and chapter brothers Wayne

Dallas and Ron Loftin of Omega Psi Phi Fraternity, Inc for helping me ‘See It Through’. Much love to my brother Charles (a.k.a. Butch) and sister, Paula, for their unconditional love, protection, guidance, and support my entire life. A heartfelt, “Thank you” to my aunts, uncles, cousins, in-laws, and enormous circle of friends for all that you have done; especially cousins Tim and Rick who were the keepers of my sanity throughout this undertaking. Thanks to my special neighbor, Ms Jackie Wallace, for her continual encouragement and embracement of my family. Thanks to my spiritual counselor, Josiane d’Hoop for getting me through the emotional roller coaster ride of the past 2 years. A most humble and appreciative, “Thank you” to my mentor and friend, Chancellor Harold Martin (NC A&T), for all his guidance over the past 25 years and for providing a shining example of high attainment. Lastly, thanks to my sensai, Jeffrey Macdonald, for the following:

- Going against the norm and providing me the opportunity to work in his lab
- Sharing his limitless knowledge of metabolism, bioreactors, and NMR
- His resourcefulness in identifying successful funding opportunities
- Helping me push through the painstaking challenges of this project
- His positive energy throughout the continual trial and error of experiments
- Being my biggest advocate and never giving up on me
- And most importantly…his kindness, integrity, and friendship

Table of Contents

List of Tables……...vii

List of Figures……viii

List of Abbreviations and Symbols....……vxi

1 Introduction..... 1

1.1 *In Vivo* Nuclear Magnetic Resonance (NMR) Spectroscopy 1

1.1.1 Proton NMR (^{1}H) 2

1.1.2 Phosphorus-31 NMR (^{31}P) 4

1.1.3 Carbon-13 NMR (^{13}C)..... 7

1.2 Metabolomics 8

1.2.1 Analysis of Footprint (or media)..... 9

1.2.2 Analysis of Fingerprint (or Tissue) 12

1.3 NMR-compatible Bioartificial Liver (BAL)* 13

1.3.1 Suspension..... 19

1.3.2 Entrapment Compared to Membrane BALs..... 20

1.3.3 Microcarrier..... 25

1.3.4 Membrane..... 27

2 Bioreactor Development and Design Considerations..... 29

2.1 Rationale and Goals..... 29

2.2 Electrostatic Encapsulation..... 30

2.2.1 Encapsulate Diameters 32

2.2.2 Calcium Chloride ($CaCl_2$) as a Gelling Agent 35

2.2.3 Barium Chloride ($BaCl_2$) 37

2.2.4 Oxygen Concentrations 39

2.3 Iterative Design Toward the Final Fluidized-Bed Design 41

2.3.1 Gondola (packed-bed) 41

2.3.2 Perforated polyethylene plug 43

2.3.3 Fluidized-bed 44

2.3.4 Flow rates 45

2.3.5 Materials 46

2.3.6 Open vs Closed System 47

2.4 Concluding Remarks and Final Design 49

3 NMR-compatible Bioartificial Liver for Real-Time Toxicokinetics and Toxicodynamics 50

3.1.1 Acetaminophen (APAP) 53

3.1.2 Fluxomics 54

3.1.3 Methods 54

3.1.4 JM1 Cell Culture 55

3.1.5 Encapsulation 55

3.1.6 In Vivo ^{31}P and ^{13}C NMR Spectroscopy 56

3.1.7 Drug Treatment 56

3.2 Results 58
3.3 Discussion 68
4 Effect of Oxygen in a NMR-compatible Fluidized-bed Bioartificial Liver 70
4.1 Introduction 70
4.2 Methods 72
4.2.1 Bioreactor Design and Life Support System 73
4.2.2 Hepatocyte Isolation Procedure 73
4.2.3 Encapsulation Methods 74
4.2.4 In Vivo ^{31}P and ^{13}C NMR Spectroscopy and BAL Operation 75
4.2.5 High Resolution ^{1}H NMR Spectroscopy 77
4.2.6 Histology In Vivo ^{31}P NMR Spectroscopy 77
4.2.7 Oxygen Electrode Construction and Measurement 78
4.2.8 Modeling of Oxygen Gradients in the Encapsulates 79
4.3 Results 80
4.4 Discussion 91
5 Conclusions 96
5.1 Future Studies 96
5.1.1 Problems and changes to existing hardware (APAP sticking) 96
5.1.2 Pulse sequence and elimination of media signal (Software) 97
5.1.3 Calibration of in vivo data (Extracts) 97
5.1.4 Data analysis and metabolic model 98

6 References..... 100

List of Tables

TABLE 1-1: COMPARISON OF BIOREACTOR CATEGORIES 19

TABLE 2-1: RESULTS OF TWO ALGINATE GELLING SOLUTIONS 39

List of Figures

FIGURE 1-1 PROTON NMR SPECTRUM OF BAL PERFUSION MEDIA 4

FIGURE 1-2 REPRESENTATIVE ^{31}P SPECTRUM OF JM1 CELLS 5

FIGURE 1-3 INTRACELLULAR PH 6

FIGURE 1-4 13C GLUCOSE LABELING OF PRIMARY RAT HEPATOCYTES 8

FIGURE 1-5 THE THREE BAL DESIGNS DESCRIBED IN THIS REVIEW 17

FIGURE 1-6 GENERIC BIOREACTOR LIFE-SUPPORT LOOP AND BIOREACTOR. 18

FIGURE 1-7 INOCULATION OF THE HYBRID HOLLOW-FIBER BIOREACTORS. 21

FIGURE 1-8 COMPARISON OF IN VIVO ^{31}P MR SPECTRA 22

FIGURE 1-9 AN IN VIVO ^{13}C MR SPECTRUM OF THE FLUIDIZED-BED BIOREACTOR. 24

FIGURE 2-1 ELECTROSTATIC BEAD SPRAY DESIGN. 31

FIGURE 2-2 CONFOCAL IMAGES OF 10 MM THICK SLICES 34

FIGURE 2-3 A 9 μM CRYOSTAT SLICE OF AN ENCAPSULATE STAINED WITH H&E STAIN (60X MAGNIFICATION). 36

FIGURE 2-4 A 9 μM CRYOSTAT SLICE OF ENCAPSULATED RAT HEPATOCYTES USING 150 MM $BACL_2$. 38

FIGURE 2-5 GAS EXCHANGE MODULE (GEM) 40

FIGURE 2-6: THE GONDOLA DESIGN. 42

FIGURE 2-7: THE ADDITION OF POLYETHYLENE PLUG. 43

FIGURE 2-8: THE FINAL FLUIDIZED-BED DESIGN 45

FIGURE 3-1 (**A**) GLUTATHIONE, A TRIPEPTIDE (Γ-GLUTAMYL-CYSTEINYL-GLYCINE). (**B**) BROMOBIMANE 52

FIGURE 3-2 ACETAMINOPHEN METABOLISM AND TOXICITY PATHWAYS. 53

FIGURE 3-3 EXPERIMENTAL PROTOCOL 57

FIGURE 3-4 THREE DOSES OF ACETAMINOPHEN DRUG TREATMENT WITH ^{31}P AND ^{13}C NMR ACQUISITIONS. 58

FIGURE 3-5 THE METABOLIC MODEL OF BROMOBIMANE-GLUTATHIONE CONJUGATION AND EXCRETION. 59

FIGURE 3-6 EXPERIMENTAL PROTOCOL AND ^{31}P NMR SPECTRA OF EACH BROMOBIMANE TREATMENT.. 60

FIGURE 3-7 OVERNIGHT ^{13}C TIMECOURSE AND EQUATIONS 61

FIGURE 3-8 TOXICOKINETICS OF BROMOBIMANE DRUG TREATMENTS. 62

FIGURE 3-9 SUMMARY OF TOXICOKINETICS STUDY 63

FIGURE 3-10 ^{31}P NMR SPECTRA PRE/POST APAP DOSING, A) 2 MM, B) 25 MM AND C) 50 MM. 64

FIGURE 3-11 TOXICOKINECTICS OF APAP DRUG TREATMENT. 65

FIGURE 3-12 TARGETED PATHWAYS OF ACETAMINOPHEN METABOLISM. 66

FIGURE 3-13 MEDIA ANALYSIS OF APAP METABOLITES BY ^{1}H NMR. 67

FIGURE 3-14 GLUCOSE CONSUMPTION AND LACTATE PRODUCTION 68

List of Abbreviations and Symbols

γ	gyromagnetic ratio
μ	magnetic moment
ρ	Pearson's correlation coefficient
Σ	sum
1D	one dimensional
180x	180° NMR irradiation pulse
2D	two-dimensional
90x	90° NMR irradiation pulse
ADP	adenosine diphosphate
APAP	N-acetyl-para-aminophenol (acetaminophen)
ATP	adenosine triphosphate
B0	applied magnetic field
cw	continuous wave
DNA	deoxyribonucleic acid
FID	free induction decay
FT	Fourier transform
GSH	reduced glutathione
GST	glutathione-S-transferase
I	nuclear spin number
LB	line broadening
M	molar

MHz	megahertz
NAC	N-acetyl cysteine
NAPQI	N-acetyl-para-benzoquinone imine
NOE	nuclear Overhauser effect
NOESY	nuclear Overhauser effect spectroscopy
NMR	nuclear magnetic resonance
NSAID	nonsteroidal anti inflammatory drug
P	angular momentum
P1	NMR irradiation pulse
P450	cytochrome P450 enzymes
PC	principal component
PCA	principal components analysis
ppm	parts per million
RF	radiofrequency
RNA	ribonucleic acid
S/N	signal to noise ratio
SULT	sulfotransferase
T	Tesla
TMAO	trimethylamine N-oxide
TSP	trimethylsilyl propionic acid
UDP	uridine diphosphate
UGT	UDP-glucuronosyl transferase

1 Introduction

1.1 *In Vivo* Nuclear Magnetic Resonance (NMR) Spectroscopy

Nuclear magnetic resonance (NMR) is a physical phenomenon first described by Felix Bloch and Edward Mills Purcell in 1946. They shared the 1952 Nobel Prize for physics for their discovery. NMR is used as a spectroscopy technique to obtain physical, chemical, and electronic information about molecules. NMR is also the technology on which Magnetic Resonance Imaging (MRI) is based. NMR spectroscopy is based on the magnetic properties of nuclei. Therefore it is feasible on any nucleus possessing a magnetic moment. When placed in a strong, external magnetic field, the nuclei can be observed by the absorption and emission of electromagnetic radiation in the range of radiofrequencies, or megaHertz. This induced energy difference between nuclear spins states, known as Zeeman levels, is very small when compared with other forms of spectroscopy or imaging, and therefore NMR is a relatively insensitive technique. However, this minimal perturbation of spins is what makes NMR ideal for *in vivo* measurements because it is noninvasive and nondestructive, unlike mass spectrometry (MS) or computer tomography (CT).

For *in vivo* applications the most common and informative nuclei metabolically are proton (^{1}H), carbon-13 (^{13}C), phosphorus (^{31}P) and sodium (^{23}Na). Even though the number of relevant nuclei is limited a large number of metabolites can be detected simultaneously. ^{1}H NMR and magnetic resonance spectroscopic imaging (MRSI) allows the detection of a number of important metabolites associates with physiological function such as, neurotransmitters in brain (1), and biomarkers of cancer from the end product of glycolysis,

lactate, or lipid intermediates for membrane synthesis (2). Energetically important metabolites, intracellular and extracellular pH, magnesium concentration and reaction fluxes can be observed with ^{31}P NMR (3,4). Likewise, ^{13}C NMR enables the noninvasive investigation of important metabolic pathways, like the tricarboxylic acid cycle (TCA), in vivo.

The Larmor equation can be used to determine the amount of energy needed for a given nucleus to resonate. The equation describes the relationship between the strength of the magnetic field, B_0, and the precessional (Larmor) frequency, ω_0.

$$\omega_0 = \gamma B_0 \qquad \textbf{Eq. 1}$$

The gyromagnetic ratio, γ, is the ratio of the magnetic moment to the angular momentum of a particle, and is constant for a given nuclei. For example, ^{1}H has γ = 4, 258Hz/G, or 26.751 (x10^{7}rad/(T x s) and is used as a reference for all other nuclei, and is set to 1. The relative sensitivity of other nuclei can be determined by comparing their respective γ, and the natural abundance of the isotope of interest. The absolute sensitivities derived from gyromagnetic ratios and natural abundance of ^{1}H, ^{31}P, ^{23}Na, and ^{13}Care 1, 0.0925, 0.063, and, 0.000176, respectively, but only ^{13}C is not 100% naturally abundant, it 1.1% naturally abundant, whereas ^{12}C is 98.9% abundant (http://www.pascal-man.com/periodic-table/periodictable.html). If 13C were 100% fractionally enriched or abundance like ^{1}H, ^{31}P, ^{13}C, and ^{23}Na its relative sensitivity would be 0.0159.

1.1.1 Proton NMR (^{1}H)

In vivo ^{1}H NMR is a powerful technique to observe, identify, and quantify a large number of biologically important biochemicals in intact tissue since nearly all biochemicals contain protons. Besides the low-abundance hydrogen isotope tritium, the proton nucleus is

the most sensitive nucleus for NMR both in terms of high natural abundance (>99%) and intrinsic NMR sensitivity (high gyromagnetic ratio). However, the application of ^{1}H NMR to intact tissue *in vivo* is challenging for the following reasons:

1. The water resonance (~55 M) is several orders of magnitude larger than the low concentration metabolites (~0.01 M) thereby making it difficult to detect them.
2. Large lipid signals can overwhelm small metabolite signals.
3. Heterogeneous magnetic field will significantly decrease the spectral resolution.

These challenges must be addressed with water suppression and spatial localization techniques as well as methods to optimize the magnetic field homogeneity. In addition, the chemical shift range is only 8 ppm for nonexchangeable protons thereby making it difficult to separate and quantify a large number of overlapping metabolites. Hence, spectral editing techniques must be utilized to separate metabolites and spectral processing methods such as, baseline correction, phase/frequency adjustment, line shape correction and residual water removal are required for quantification of ^{1}H NMR spectra.

For NMR-compatible bioartificial liver (BAL) experiments, there is only report published using suspended hepatocytes with no perfusion, and investigated the effect of acetaminophen. The cells quickly became hypoxic as indicated by large lactate peaks and no visible antioxidants, such as glutathione (5). ^{1}H NMR is mainly utilized to analyze the media and cell extracts in order to quantify various metabolites of interest, such as glucose, lactate and alanine. **Figure 1.1** shows a typical ^{1}H NMR spectrum acquired from the BAL perfusion media during an experiment using primary rat hepatocytes. Some of the main peaks are labeled. The large peak at 0 ppm is a chemical shift and concentration reference, trimethylsilyl[2,2',3,3' deutero]propionic acid (TSP), added to the samples. Relative

abundance of aromatic (6-9 ppm) and aliphatic (0-6 ppm) compounds can quickly be determined from the spectrum by comparison of peak areas divided by the number protons represented by the respective (6).

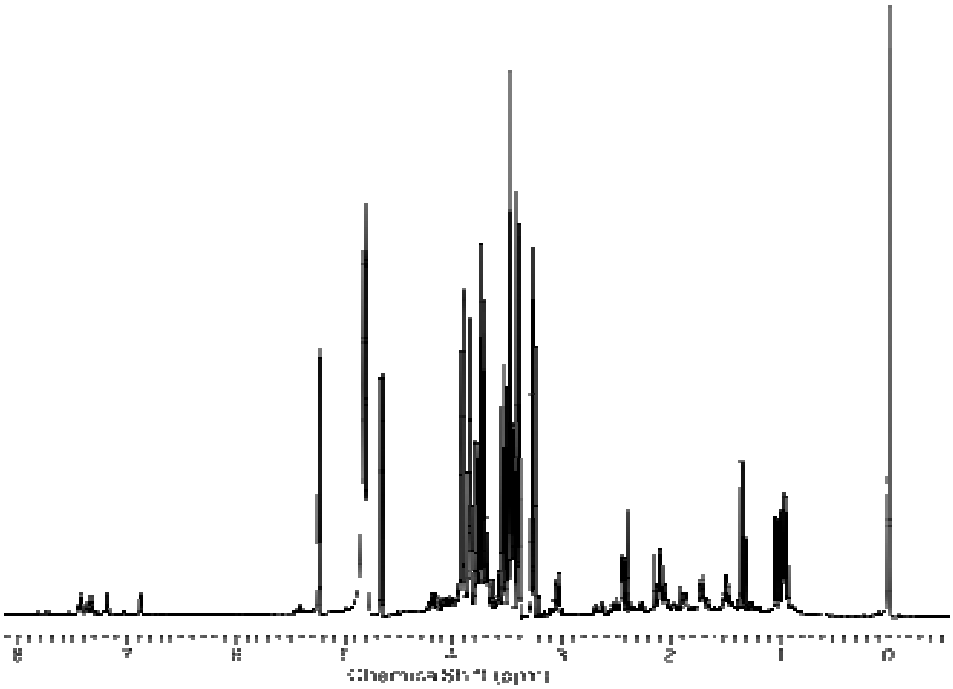

Figure 1-1 Proton NMR spectrum of BAL perfusion media

1.1.2 Phosphorus-31 NMR (^{31}P)

The 1D ^{31}P NMR experiment is much less sensitive than ^{1}H but more sensitive than ^{13}C. 31P is a medium sensitivity nucleus that yields sharp lines and has a wide chemical shift range. The relatively high sensitivity of phosphorus NMR (ca 7% of protons) along with a 100% natural abundance enables the acquisition of high-quality spectra within minutes. The chemical shift dispersion is relatively than ^{1}H - about 30 ppm for the important *in vivo* resonances. The ^{31}P MR spectrum contains viability information by monitoring ß-NTP over time (7), which is approximately 80% adenine triphosphate (ATP) in liver (8). ^{31}P NMR is

very useful in bioenergetics because it is capable of detecting all metabolites involved in energy metabolism, such as adenosine triphosphate (ATP), inorganic phosphate (Pi) and the sugar phosphates, but also the phospholipid intermediates, phosphoryethanolamine (PE), phosphorylcholine (PC), glycerophosphethanolamine (GPE), and glycerolphosphocholine (GPC). A representative in vivo ^{31}P NMR spectrum of alginate encapsulated rat hepatoma cells (JM1) is shown in **Figure 1.2.**

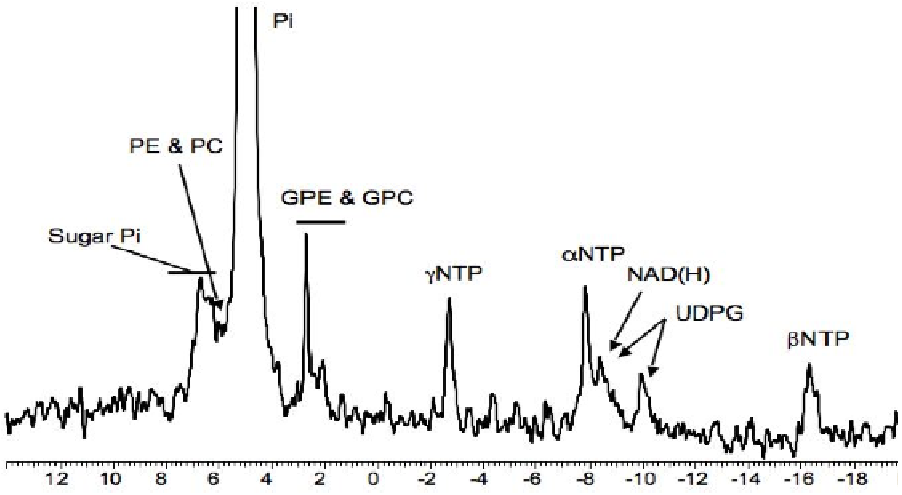

Figure 1-2 Representative ^{31}P spectrum of JM1 cells after 9 hours in the NMR compatible bioreactor.

1.1.2.1 Intracellular pH

Physiological parameters like intracellular pH and ionic (e.g. magnesium) strength have a direct effect on the exact chemical shift position of almost all resonances. Moon and Richards (9) used ^{31}P NMR on intact red blood cells and showed how the intracellular pH can be determined from chemical shift differences. The resonance of inorganic phosphate (Pi) is most commonly used because 1) its second exchangeable proton, or pK_{A2}, is in the physiological range (pK_{A2} = 6.77), 2) it is readily observed in most tissues, and 3) its

chemical shift has a large dependence on pH. Hence, pH can be described by a modified Henderson-Hasselbach relationship as:

$$pH = pK_A + \log\left((\delta - \delta_{HA}) / (\delta_A - \delta)\right) \qquad \textbf{Eq. 1.1}$$

where δ is the observed chemical shift, δ_A and δ_{HA} are the chemical shifts of the unprotonated and protonated forms of compound A and pK_A the logarithm of the equilibrium constant for the acid-base equilibrium between HA and A. **Figure 1.3** shows a 31P NMR spectrum of an MCF-7 breast cancer cell line. The pH is usually determined from the chemical shift between phosphocreatine (PCr) and Pi. However, PCr is completely absent in ^{31}P NMR spectra of liver since creatine kinase is not expressed (10), therefore the α-NTP resonance is used as an internal chemical shift reference (-7.50 ppm).

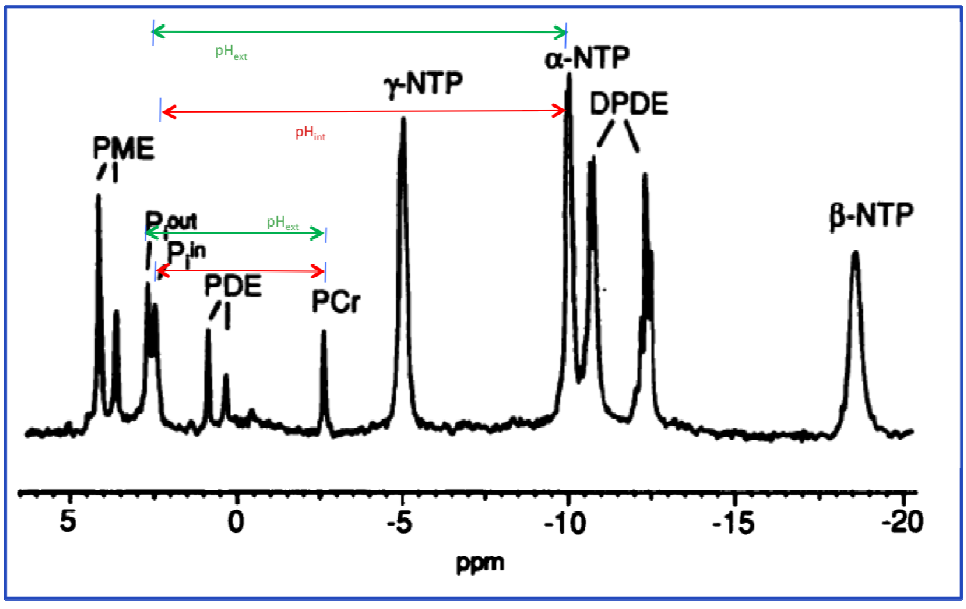

Figure 1-3 Intracellular pH as determined by the chemical shift between Pi and reference resonance.

1.1.3 Carbon-13 NMR (^{13}C)

Since almost all metabolically relevant compounds contain carbon, ^{13}C NMR is in principle able to detect many metabolites, thus offering complementary information to that obtained with ^{1}H/^{31}P NMR. Although 1H and 31P NMR have been successfully utilized in numerous in vivo studies, they are still limited in that ^{1}H NMR is hindered by the small chemical shift range and ^{31}P NMR originates from only a small number of low molecular weight compounds. ^{13}C NMR has a large spectral range (>200 ppm), narrow line widths and a relative low sensitivity, due to its 1.1% natural abundance and low gyromagnetic ratio (γ_{13C}/γ_{1H}) = 0.251, resulting in a absolute sensitivity of 0.000176, as described above. The low sensitivity can, however, be overcome by polarization transfer, averaging, increasing number of nuclei by fractional enrichment thereby resulting in resonances with excellent spectral resolution and biochemical information.

In fact, the power of ^{13}C NMR lies in its low natural abundance, where is unique in that ^{13}C-labeled precursors allow for the detection of metabolic fluxes. For example, in animals and humans carbohydrate reserves are mainly stored as glycogen. In fact, it is very abundant in muscle and liver, reaching concentrations up to 30-100 mmol kg^{-1} and 100-500 mmol kg^{-1}, respectively (11). A representative ^{13}C NMR spectrum (nt=384) of encapsulated primary rat hepatocytes is shown in **Figure 1.4**. The spectrum illustrates glycogen synthesis resulting from U-13C-glucose consumption during hours 1-12 of infusion.

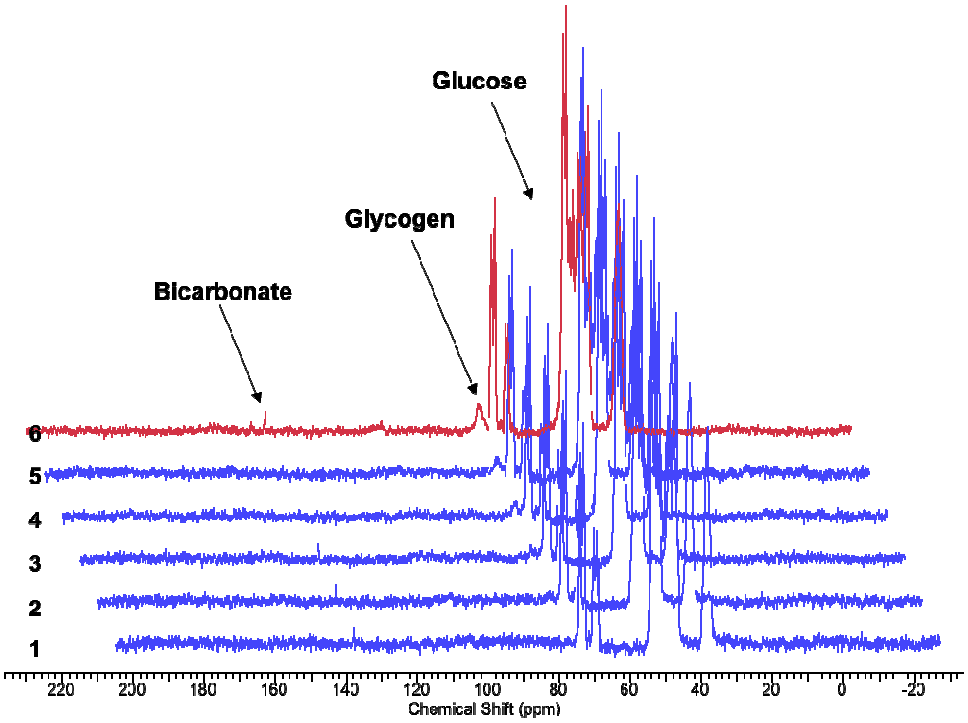

Figure 1-4 13C glucose labeling of primary rat hepatocytes in NMR-compatible bioreactor. (Blue spectra) Taken every hour following initial infusion of U-13C-glucose over 5 hours. (Red spetra) Cumulative spectra of 8 hours (time 6-12 hours) of U-13C-glucose.

1.2 Metabolomics

Metabolites are defined as low molecular weight compounds that are not genetically encoded but are produced and modified by cells under a given set of physiological conditions (12-15). The word *metabolome* has been coined to designate the entire ensemble of metabolites present in and derived from a given living organism (12). Metabolomics utilizes several methods to quantify cell metabolites in order to determine how metabolite interactions and levels influence phenotypes. Although these methods have been in use since the early days of biochemistry, only recently have attempts been made at detecting changes by simultaneously analyzing large numbers of metabolites, mostly by methods based on mass spectrometry (MS) and nuclear magnetic resonance (NMR) (16). Due to its integrated

measurement of cellular phenotype, metabolomics is highly suited to quantitative analysis and description. It is considered to be more discriminatory than transcriptomics or proteomics because it is downstream, therefore changes in the metabolome are amplified relative to changes in the transcriptome or proteome. This results in a more easily measureable change even when changes in metabolic fluxes are neglible (17).

Currently, metabolomics is a hypothesis generation strategy, as there is limited knowledge of expected metabolic differences (15). Typically, metabolic profiling is used to detect a wide range of metabolites covering a number of different metabolic classes to provide as large an overview of metabolism as achievable. After a well-designed experiment is performed, the data is interrogated to define metabolic differences observed (18,19). The intracellular metabolome (endometabolome) and extracellular metabolome (exometabolome or 'metabolic footprint' (20,21)) can be studied, giving clues to metabolic pathways utilized within the cell and the effects cells may be having on their environment through released products (22,23).

1.2.1 Analysis of Footprint (or media)

It is important to differentiate between intracellular and extracellular metabolites because they can play different roles. Assessment of the intra-cellular metabolome requires technically demanding processes including: metabolic quenching, cell lysis and metabolite extraction. An alternative method is to study the extra-cellular metabolome which is easier to sample and analyse, and allows high-throughput investigations. This approach uses tissue or cell culture in a metabolite-complex medium, allowing the intra-cellular metabolism to be investigated by analysis of the extra-cellular metabolome – an approach termed 'metabolic

footprinting' (15). Metabolic footprinting as described relies not on the measurement of intracellular metabolites but on the monitoring of metabolites consumed from, and secreted into, the growth medium. To maximize the excretion of metabolites 'overflow' metabolism is stimulated by adding to the fully defined medium various carbon compounds that 'probe' metabolically active networks in the same way that an engineer might probe an electrical circuit (24).

In an extracellular environment, any changes in the level of extracellular metabolites will directly reflect any modification of the environment caused by activities of the cells present in the system. For example, nutrients will be consumed and many extracellular metabolites are formed as byproducts from the activity of metabolism. Cells fine-tune their metabolism according to the environment to maximally exploit natural resources. Metabolic footprinting represents the effect of a particular cellular metabolism on the environment, leading to a direct and mutual relationship between the set and level of extracellular metabolites and the intracellular metabolism. The release of metabolites that are part of the central carbon metabolism (e.g. acetate and lactate) allows the cells to maintain biochemical balance, thereby assuring the optimal operation of the metabolism. Furthermore, the presence of metabolites that are not expected to be secreted or excreted by cells (e.g. phosphoenolpyruvate, pyruvate,..) can be used as a marker of cellular lysis, thereby providing information about particular growth conditions, such as pH and osmolarity, that might indicate cellular stress (25).

The main program to which metabolic footprinting data will contribute strongly is the generation and testing of mathematical models of cell behavior, whose interleaving with 'wet' experiments is the hallmark of systems biology (26,27). Therefore, measurement of the

metabolic footprint before, or as well as, measurement of the intracellular (or endo-) metabolome can provide a useful set of constraints for metabolic models. Searching parameter space to optimize a metabolic model that can reproduce experimental data is difficult (28). However, once the model can reproduce the exometabolome accurately, many of the parameters will be sufficiently well determined to provide good starting points for the fine-tuning with which they can also reproduce the endometabolome, first as steady-state 'snapshots' (29) and then as time series.

NMR analysis of media has determined that the TSP used as a concentration calibrant will bind to the proteins in the serum added to the media, but as long as appropriate pulse sequences and serum concentrations are less than 10%, as in this study, metabolite concentrations can be quantified (Seagle et al., 2008). In addition, the bioartificial liver permits the biosystem boundaries to be clearly defined and biochemical input ca be controlled, thereby a mass balance can be easily obtain as compared to a whole organism.

Effectively, metabolic footprinting is what the classic metabo(n)omic studies do when the urine is analyzed, wherein the effects of toxins on target organ are identified by classifications by principle components analysis for correlating of urine metabolites to organ toxicity (30). Also, TCA intermediates in urine could come from just about any organ, so when differences in the levels of TCA intermediates were mutant mice versus the wild type (31), it is difficult to correlate that to an organ or metabolic mechanism. The problem is that this is an indirect measure of what one would like to measure – the metabolome in the target organ(s) of interest.

1.2.2 Analysis of Fingerprint (or Tissue)

Metabolomics offers some unique advantages over other –omics disciplines (15) and one of the main approaches of metabolomics for disease diagnostics is metabolic fingerprinting. Metabolic fingerprinting is the rapid classification of samples according to their origin or biological provenance (13) where it is not initially necessary or feasible to determine the levels of metabolites individually but to develop a high-throughput technique that enables a snap-shot of the metabolic composition at a given time. Changes from 'normality' are detected and correlated with disease progression or remission; the latter may be surgical intervention, pharmacological or nutritional. The bottom line of metabolic fingerprinting is to obtain enough information to unravel (otherwise hidden) metabolic alterations, without aiming to get quantitative data for all biochemical pathways. Therefore, the resolution of the analytical devices must be high enough to handle critical information. Such devices as nuclear magnetic resonance, mass spectrometry, or Fourier transform infrared spectroscopy (FT-IR) provide this resolution.

However, metabolic fingerprinting can easily be over-interpreted, since signals suitable for distinguishing among samples might not be biologically relevant, or might not be applicable when distinguishing among samples from other species (or situations). For example, Warne and others (32) studied metabolic effects by NMR after dosing earthworms with toxins. By pattern recognition, they noted elevated levels of glucose, citrate, and succinate as potential biomarkers for toxicity. The are clearly many situations where intermediates of the TCA cycle become elevated and generalizations about the suitability of this method for establishing the mechanism of toxic action should be avoided. For example, without ^{13}C tracers and relying just on concentration it is impossible to determine whether

glucose, citrate, and succinate increased due to inhibition or an increase in metabolic activity of the glycolysis and the TCA cycle.

In the realm of functional genomics, NMR was used to detect metabolic phenotypes in yeast mutants that did not show obvious visible phenotypes. However, the informative power of NMR was not sufficient in this instance to quantify individual metabolite levels; analysis of enzyme levels had to be applied additionally (17). This technique has since been extended to examine the structure of metabolic pathways and the network of metabolism in yeast (33). Therefore, metabolic fingerprinting ultimately benefits from transcriptomics or targeted proteomics to identify enzyme levels, however, use of ^{13}C-labeled nutrients and determination of flux within the metabolic fingerprint in combination with concentration, quantifies the real activities of these enzymes *in vivo*. In fact, quantifying enzyme activity *in vivo* is the ultimate goal of proteomics, which simply quantifies concentration. In summary, there are many technical challenges that need to be addressed in order to generate comprehensive metabolomic data, however, metabolic fingerprinting is gaining considerable interest across a wide variety of disciplines with biomarker discovery for disease prognosis, diagnosis and therapy monitoring, and the addition of flux is essentially *in vivo* proteomics and permits a comprehensive phenotype to be identified.

1.3 NMR-compatible Bioartificial Liver (BAL)*[*]

MRS studies of cell preparations permit the control of cell composition, and contributions from immune, endocrine, paracrine, and physico-chemical parameters not afforded in intact or perfused organ systems [for reviews (34-39)]. Since 1973, four

[*] Portions of Section 1.3 were selected from a review that was submitted to ***NMR in Biomedicine*** on March 31, 2010, "*Three Decades of NMR-compatible Bioaritificial Liver*" by RE Jeffries and JM Macdonald.

categories of MR-compatible mammalian cell perfusion systems have evolved (9): (1) suspension (40), (2) entrapment (41-44), (3) microcarrier (37,45), and (4) membrane (46). **Table 1-1** contains some MR and physiological metrics for comparison of these various bioreactor categories.

Although MR-compatible bioartificial livers (BALs) have been used for three decades (47,48), the lack of long-term cell viability and simplicity of bioreactor operation has hindered its widespread application in the pharmaceutical industry. Initially, MR-compatible bioreactors for hepatocytes, or bioartificial liver (BAL), used hepatocyte suspensions, but function and viability only persisted for several hours before hypoxia caused cell death (5,40,49,50). This is because suspension bioreactors are the only category in **Table 1-1** without perfusion, and therefore the mass transfer is the worse of all the categories. However, from an MRS standpoint, they easy to operate, have excellent the global density (i.e., the percent of sensitive volume in the coil filled by cells) leading to a superior signal-to-noise ratio, and can be packed in a 5 mm NMR tube, so standard high resolution NMR spectrometers can be used leading to superior resolution and sensitivity.

The goal of these early studies was not to maintain long-term viability, but to obtain short-term metabolic information, and a few hours is all that was required for this goal. This simple BAL evolved to perfusion systems where hepatocytes were entrapped in collagen threads (51-57), alginate spherical encapsulates (58-60), or inoculated into membrane bioreactors (7). The most widely applied method for metabolism studies is the entrapment technique whereby cells are immobilized in threads of agarose (61) or alginate (41,43). All early BAL studies used non-physiological concentrations of oxygen, typically 95:5 oxygen:carbon dioxide (carbogen) (47) in order to overcome hypoxia, whereby in vivo, the

blood has hemoglobin to reduce the oxygen gradient across the liver (**Table 1-1**). Also, simple salt solutions or non-basal media solutions had been used (**Table 1-1**), which is not permissive for long-term cultures, and more typical of toxicology studies (Macdonald et al., 2002). More recently, with the advent of tissue engineering, MRS and especially MRI have been used as tools to characterize the bioreactor with MRS focusing on ^{31}P and viability (5,7,49-58), with no reported studies of ^{13}C, ^{15}N, ^{1}H or ^{19}F to characterize tissue engineered BAL function. Although recently dynamic nuclear polarization ^{13}C MRS has been used to determine flux rates in alginate-encapsulated rat hepatoma cells perfused in a fluidized-bed BAL (62), this review will focus on primary hepatocytes. ^{1}H MRI has been used to obtain inoculation efficiency and distribution, as well as quality assurance data (7), and velocity-encoded MRI has been used to define the flow characteristics (63), while diffusion-weighted MRI or other forms have not yet been applied to a BAL. One reason for this lack of research is that conventional BAL systems do not fit in vertical bore magnets and require horizontal bore magnets, which typically do not have a second broadband channel and/or one does not have easy instructions on making BALs MRS- and MRI- compatible. This review will give an easy step-by-step approach to making any BAL MR-compatible and present examples of applying multinuclear MRS protocols to monitor viability and function of several BAL designs, as well as MRI applications to characterize inoculation efficiency and distribution in opaque materials, quality assurance, flow dynamics, and oxygen distribution.

Since suspension BALs were the first design attempted and are not feasible systems for long-term maintenance of liver cells in tissue engineering (**Table 1-1**), they will not be used for demonstration of MRS and MRI applications in this review. Rather, three bioreactors corresponding to membrane, microcarrier, and entrapment, which have been

MRS- and MRI- tested in the author's laboratory, will be used to demonstrate the applications of MRS and MRI, while demonstrating the effects of various bioreactor parameters on hepatocyte viability, such as, diffusion distance, shear forces, channeling, and the effect of gelling or aggregation of hepatocytes. **Figure 1-5** includes diagrams and photos of the three bioreactors that will be discussed as examples of three of the four categories outlined in **Table 1-1**: (1) the hollow fiber membrane bioreactor inoculated with ***microcarriers***, (2) the ***membrane*** multi-coaxial hollow fiber bioreactor, and (3) the fluidized bioreactor consisting of alginate ***entrapped*** hepatocytes.

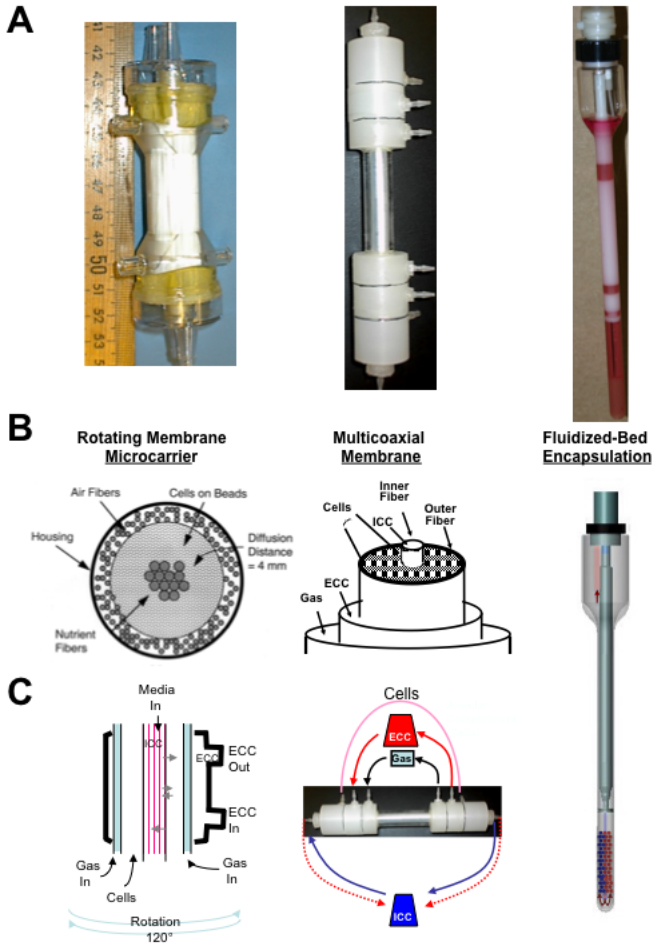

Figure 1-5 The three BAL designs described in this review: hybrid hollow fiber-microcarrier, multicoaxial hollow fiber membrane, and fluidized-bed encapsulation bioreactors. Three photos of the bioreactors (**A**) with details of their design (**B**) and flow patterns (**C**).

A drawing of a generalized perfusion loop for a BAL is shown in **figure 1-6** with the various components. Everything present in a standard life-support unit of a BAL system is present in the MR-compatible system, except the perfusion lines are lengthened and the recommended heating and oxygenation are in parallel and near the magnet. There are two benefits to this: (1) the perfusion media can be maintained at room temperature inhibiting bacterial growth and degradation of media components, such as glutamine, and (2) there is no out-gassing in the bioreactor due to a change in solubility of oxygen caused by a drop in temperature in the magnet. An MR-compatible, autoclaveable gas exchange/heater module

has been described that solves these issues (64). It is very important to place a bubble trap just before the media line enters the bore at the top of the vertical-bore magnet. Bubbles can get trapped inside the BAL and destroy spectral quality due to enormous magnetic susceptibility effects caused by the air-water interface.

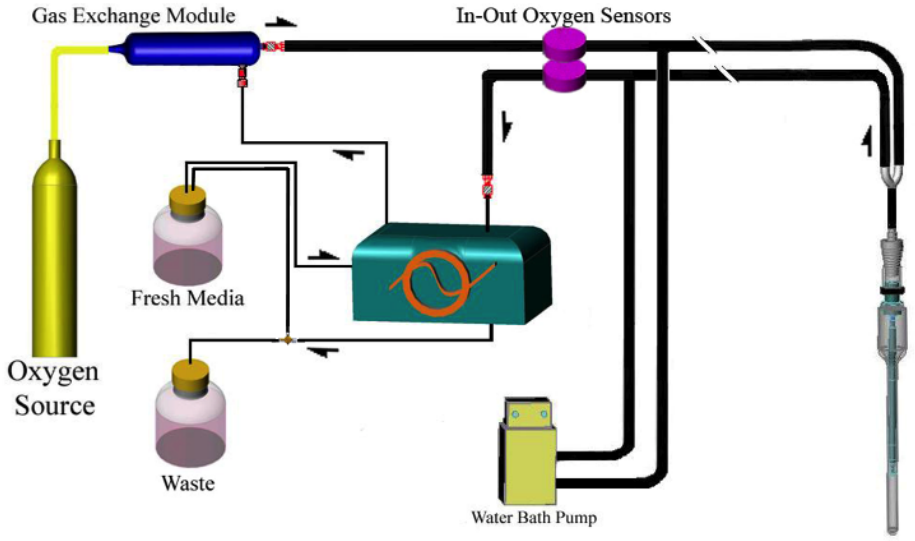

Figure 1-6 Generic bioreactor life-support loop and bioreactor. Block diagram of the bioreactor loop showing the major components and with a gas exchange module that heat and oxygenates the media simultaneously (12) so that media can be maintained at room temperature.

Figure 1-6 shows in-line oxygen electrodes to monitor oxygen consumption. This is difficult with Clark electrode for long-term tissue engineering studies as the membrane become fouled and if one monitors media oxygen levels periodically via tee connections throughout the study period, these are potential sources of contamination. If oxygen consumption is desired, a non-invasive fluorescent oxygen sensor is recommended – they do not consume oxygen during the measurement, unlike the Clark electrode, which becomes important for small volumes. At the very least it is essential to measure the drop in oxygen

concentration from the gas exchange module down the water-jacketed line to the bioreactor, since polyethylene tubing is extremely permeable to oxygen and will diffuse into the water-jacket fluid, typically decreasing the oxygen concentration once entering the BAL. Autoclaveable FEPT tubing (0.0313" inner diameter) is recommended which is less oxygen permeable than polyethylene tubing. A 20% drop from 95% oxygen exiting the gas exchange module and traveling down a 3 foot length of tubing at 3 ml/min and 37˚ C to the bioreactor is not unexpected. Once this drop in oxygen concentration is measured and flow rate remains constant, then one could assume this value for the length of the experiment. Use of the fluidized-bed BAL (**Fig. 1-5A and 1-5C**), described below in the entrapment bioreactor category, fits inside a standard 10 mm NMR probe and is lowered from the top of the magnet as is typical for vertical bore magnets and uses the spectrometer VT system to help maintain the temperature [see (62)] (**Fig. 1-6**).

Table 1-1: Comparison of bioreactor categories

Type	Ref.	Species	Media	% O_2	Duration	Biomass SNR	NMR Resolution	Mass Transfer
Suspension	a	Rat	KHR	20%	4 hr	Excellent	Excellent	Poor (30 mm)
Microcarrier	b	Rat	DMEM	20%/40%	20 hr	Good	Poor	Poor (5 mm)
Entrapment	c	Rat	KHR	95%	6 hr	Good	Good	Poor (0.5-1.5mm)
Membrane	d	Rat	KHR	95%	6 hr	Poor	Poor	Excellent (0.2mm)

[a] Cohen et al, 1978, 1979; Brooks et al, 1985, Nicholson et al, 1985; [b] This publication [c] Farghali et al, 1991, 1993, 1996; Gasbarini et al, 1992a, 1992b, 1993, 1996; Capuani et al, 2000; Falasca et al, 2001; [c] Macdonald et al, 1998.

1.3.1 Suspension

As shown in **Table 1-1** suspension BALs were the first attempted by Cohen and others at the end of the 1970s (Cohen et al, 1978, 1979), and later by Nicholson and others in the mid-1980s (Brooks et al, 1985, Nicholson et al, 1985). It became clear quickly that this BAL was not useful beyond several hours, since the hepatocytes were suspended in a 5mm NMR tube

and became hypoxic immediately. In fact, considering the relatively high oxygen demand of hepatocytes (Macdonald et al., 1999), it is amazing any physiologically relevant data was obtained from these studies. By the end of the 1980s, perfused BALs were introduced and suspension BALs became obselete.

1.3.2 Entrapment Compared to Membrane BALs

As mentioned above, the first ^{31}P and ^{13}C MRS of a MR-compatible BAL was published over three decades ago (49). The biolimiting nutrient has always been oxygen, and in order to overcome the large diffusion distances, higher concentrations of oxygen have been used for long-term viability. Although some attempts have been made to use oxygen carriers in the encapsulation matrix to increase oxygen (65), the incorporation of perfluorinated hydrocarbons to increase oxygen delivery to hepatocytes has been inconclusive. Perfluorinated hydrocarbons do not exhibit the Bohr effect associated with hemoglobin, and at lower oxygen tension, they do not release oxygen thereby leading to higher levels of hypoxia compared to their absence (66). Nevertheless, their use in media is advantageous, however, nearly 60% is required in perfused organs (67) and perfluorinated hydrocarbons have toxic side effects (68). Therefore BAL studies have focused on modulating oxygen tension (69). Although membrane bioreactors typically have the best mass transfer because homogeneous diffusion distances can be maintained, they suffer from poor SNR due to insufficient global density, and often have significant bulk magnetic susceptibility that diminishes resolution (**Table 1**).

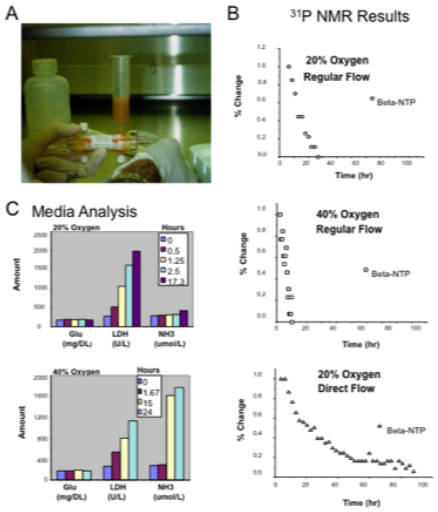

Figure 1-7 Inoculation of the Hybrid hollow-fiber bioreactors with hepatocytes mixed with microcarriers (**A**). Graphs of β-NTP/β-NTP from first spectrum from hepatocytes perfused with media subjected to 20% and 40% oxygen and 40% oxygen but directly perfused through the cell compartment (**B**) and the respective analysis of media components showing the 20% and 40% oxygen treatment with regular flow configuration showing the increase in lactate dehydrogenase validating the decrease in of β-NTP (**C**).

One advantage of a fluidized-bed bioreactor is the SNR is good, while maintaining the diffusion distance of a membrane bioreactor, by simply maintaining a homogeneous diameter while thoroughly percolating the beads in the fluidized bed. In fact, if the diameter is 0.5 mm, this is the distance across the liver acinus and the diffusion gradients associated with the three zone of the liver acinus can be recreated with a sphere (**Fig. 1-5B**, right). For example, **figure 1-8A** is a comparison of a fluidized-bed bioreactor at 9.4 T and the coaxial bioreactor obtained at 4.7T. Although the field strength was half with the hollow fiber bioreactor, the time to acquire the ^{31}P NMR spectra was 15 min and 60 min, respectively, demonstrating both the superior SNR and resolution of the fluidized bed. At a diameter of less than 700 µm the alginate microspheres are solid throughout, otherwise they can have a molten core (70).

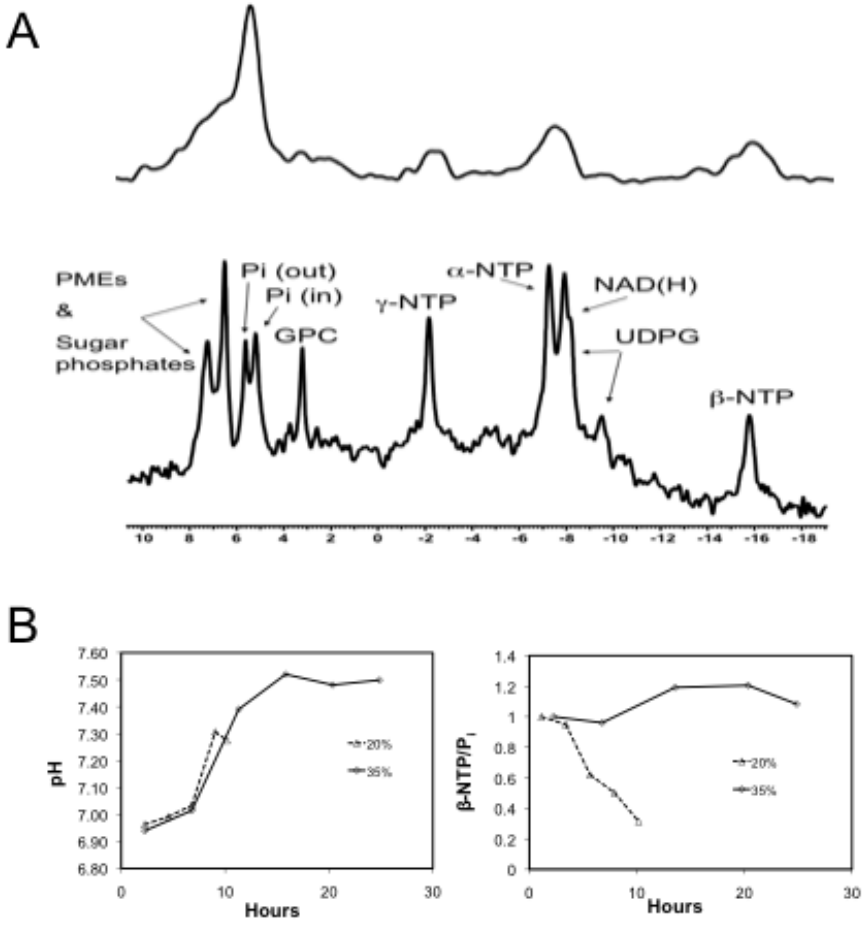

Figure 1-8 Comparison of in vivo ^{31}P MR spectra from hollow fiber membrane bioreactor (29) and the fluidized-bed bioreactor obtained in 60 min versus 30 min, demonstrating the superior SNR and resolution (**A**). Graph of intracellular pH of hepatocytes perfused with media subjected to 20%, and 35% oxygen (**B**), treatments.

1.3.2.1 ^{31}P MRS Resolution, SNR, Viability and pH

Comparison of the ß-NTP time course between 20% versus 35% oxygen in the perfusion media of the fluidized-bed BAL revealed that the hepatocytes died at ca 10 hr after inoculation and remained viable for the course of the experiments, about 28 hrs, respectively (**Fig. 1-8B**, top graph). Our data suggests that during the first 5 hr of perfusion with 35%

oxygen the hepatocytes recover from the hypoxic isolation process (**Fig. 1-8B**) and the 31P MRS spectrum (**Fig. 1-8A**) is similar to the ^{31}P NMR spectrum from intact liver (7). Calcium was used for the other oxygen treatments since previous alginate encapsulated bioartificial livers systems more commonly used calcium (59,71), and potential barium toxicities could be avoided. Although calcium is an extremely potent intracellular secondary messenger, both calcium and barium have such high affinities for the carboxylate groups that they are relatively unavailable, or the encapsulate would lose integrity and disintegrate. Although the hepatocytes were maintained for 28 hours with little change in the ß-NTP peak area (**Fig. 1-8B**), they exhibited a high degree of anaerobic glycolysis not typical in liver as indicated by the analysis of media (72) whereby 100% of the consumed glucose could be accounted for by the production rates of lactate and alanine.

1.3.2.2 ^{13}C Metabolism

Previous in vivo ^{13}C MRS studies of MR-compatible BAL focused on the perturbation of intermediary metabolism due to xenobiotic exposure (5,48-50,73). With the advent of perfusion of bioreactors 13C signal from cells and media were distinguished by utilization of diffusion-weighted pulses (74). 13C studies were all performed in suspension bioreactors, primarily for metabolism studies as mentioned above. In fact, O'Leary and others (75) were the first to analyze the media stream in real time by putting the bioreactor loop through the ^{13}C NMR probe. In fact, media is called the metabolomic footprint of cell culture and analyzed by itself as a measure of BAL performance (72). **Figure 1-9A** is ^{13}C NMR of the fluidized-bed BAL containing alginate-encapsulated rat hepatocytes and perfused with u-^{13}C-glucose showing the time course of ^{13}C-glucose incorporation into C1 of

glycogen (ca 102 ppm). The peak reach a steady-state of incorporation by about 6 hrs, and the rate of glycogen synthesis can be deterimined by fitting the peak area to an exponential. **Figure 1-9B** is the same fluidized-bed BAL, but containing a rat hepatoma cell line, JM-1. The spectrum shows the various ^{13}C resonances representing the alpha and beta conformations of 2-^{13}C-glucose. The inset time course on the upper right is the C2 position of lactate (ca 69 ppm) excreted from the hepatocyte cytosol into the media. In fact, ^{1}H NMR of the media and the cell extract at the end of the experiment established that this signal was almost entirely from the media. The rate of formation is linear and can be used to help determine the function of the hepatocytes. Normally rat hepatocytes should not produce lactate, since liver is involved in the Cori cycle for conversion of lactate derived from exercising muscle to glucose.

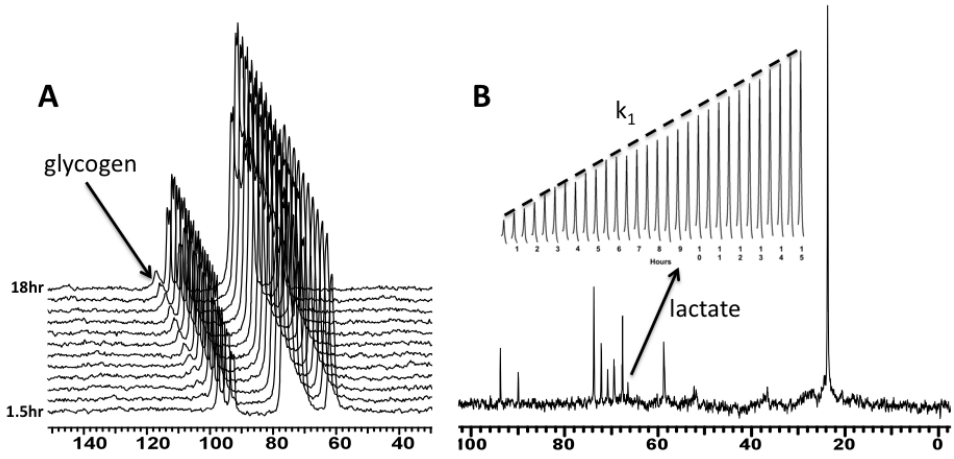

Figure 1-9 An in vivo ^{13}C MR spectrum of the fluidized-bed bioreactor immediately after inoculation with 500 µm diameter electrostatically-encapsulated alginate beads containing 3.5 x 107 rat hepatocyte per ml and perfused with 25 mM u-^{13}C-glucose (**A**). The 18 hr time course of portion of the ^{13}C NMR spectra containing C1-glycogen at 102 ppm is inset to the left of the full spectrum. *In vivo* ^{13}C MR spectrum of perfused JM-1 cells and the 15 hr time course of lactate above the spectrum (**B**).

Lactate production is typical of cancer cells, and thus was not detected in the ^{13}C MR spectral time course of perfused primary rat hepatocyte shown in **figure 1-9A**, and is an ideal functional assay of BALs and especially for determining if the culture is hypoxic. In fact, this ^{13}C MRS assay is ideal for dynamically changing oxygen content of media as the cultures grow or depending on cell distribution within the bioreactor, since this could be performed in essentially real-time, while oxygen concentration is increased or decreased.

1.3.3 Microcarrier

Ugurbil and others (76) first introduced microcarrier beads whereby mouse embryo fibroblasts were grown on the surface of polymeric beads and placed in a MR-compatible perfusion chamber for study. With microcarriers and encapsulates, a packed bed is perfused. In the former, the global density is hindered due to the fact that cells only attach to the outside of the microcarrier, with microcarrier material void of cell signal the global density is low, and thus SNR is adversely affected (**Table 1-1**). Membrane bioreactors typically separate the cells from the flowing perfusion solution by permeable membranes, allowing diffusion of nutrients and waste, but restraining the cells in the bioreactor. A hollow-fiber bioreactor is a membrane system that consists of a bundle of permeable hollow fibers running axially (46) or radially (77) through the housing and are typically capped by epoxy or thermal welding, and media or gas typically travel through the fiber lumen (78). The hybrid hollow fiber-microcarrier bioreactor (Genespan Inc, Bothell, WA) is shown in **figure 1-5A**, wherein there is an annular ring of polyethylene oxygenation fibers (300 µm outer diameter) and a central bundle of nutrient delivery cellulose acetate hollow fibers (**Fig. 1-5B** and **1-5C**), and microcarriers rest in between the two bundles and rotates 120˚ on a rocker bed. **Figure 1-**

7A shows the bioreactor being inoculated via the side port with hepatocyte-coated dextran microcarriers, and in the three experiments presented in **figure 1-7B** a total of 500 million rat hepatocytes were inoculated in each bioreactor.

1.3.3.1 Viability by ^{31}P MRS and Effect of Diffusion Distance

The first ^{31}P MRS studies of hollow fiber were used not only to monitor cell viability, but cell growth within the opaque hollow fiber bioreactors (79,80). Gillies and others (34) subsequently refined the MR-compatible design to optimize global density (i.e, the percent of volume within the MR probe consisting of cell mass), and enabled cell culture for many months to reach tissue densities. The first MR-compatible hollow fiber BAL was published by Macdonald and others (7). As an example of how ^{31}P MRS can be used in the development of BALs, data from experiments with a hybrid hollow fiber-microcarrier bioreactor with various oxygen concentrations and flow configuration were performed by Dr. Macdonald while a post-doctoral fellow in Dr. Reid's laboratory. In general, oxygen is always the rate-limiting nutrient in BALs and typically a distance beyond ca 200 µm is considered hypoxic (81). In order to address this issue, the 10 cm space between oxygen and nutrient fibers (**Fig. 1-5B**) was affected by 30-60 Hertz 120˚ rotation on a rocking stand and microcarriers containing hepatocytes were inoculated into this space (**Fig. 1-5C**).

Two oxygen concentrations were tested in the hybrid, hollow-fiber microcarrier BAL, 20% and 40% oxygen in 5% carbon dioxide with the remainder in nitrogen. The ^{31}P MRS spectra were obtained immediately after inoculation as shown in **figure 1-7C**. **Figure 1-7B** are time courses of the ß-NTP peak area relative to the ß-NTP peak area obtained in the first spectrum, and are expressed as the percent change. In all cases the ß-NTP decreased precipitously with 20% and 40% oxygen. **Figure 1-7C** display the results of analysis of

media components, showing the increase in LDH in both 20% and 40% oxygen treatment, confirming cell death. One of the main problems with hepatocytes is that the cell surface adhesion proteins, such as cadherin, cause the hepatocytes to aggregate and in fact, this is the mechanism by which liver spheroids are produced (82). Since the hepatocytes are on the surface of the collagen coated microcarriers, and even though the bioreactor is constantly rotated 120˚ on a rocker (**Fig. 1-5A**, bottom) at a period of 30 Hz, the hepatocytes still gel in the bioreactor. The gel was so solid that in a third experiment, the side port was perfused and a small portion of hepatocyte near the perfusion channel remained viable for three days (**Fig. 1-7B**, bottom graph), completely eliminating the usefulness of the hollow fiber bioreactor. In fact, this gelling phenomenon makes it impossible to suspend hepatocyte-covered microcarriers in a fluidized-bed bioreactor without gelling (**Table 1-1**), and has required alginate encapsulation methods to be employed to avoid aggregation phenomena (see below).

1.3.4 Membrane

MRS and MRI in the field of tissue engineering have primarily studied membrane BALs, in the form of a hollow fiber bioreactor. Hollow fiber bioreactors typically have sufficient mass transfer, but relatively poor global densities and thus poor SNR for MRS (**Table 1-1**), because much of the sensitive volume within the MR probe is filled with bioreactor material. A coaxial hollow fiber bioreactor is composed of a fiber within a fiber and is shown in **figure 1-5B** and can replicated the dimension of the liver lobule (47). The first published MRIs of a hollow fiber bioreactor were of a coaxial design to investigate fiber concentricity and cell distribution (83). They found that although central fibers were constructed asymmetrically, the cell culture of a mouse hybridoma cell line apparently

centered the fiber. Since the bioreactor was opaque and composed of polypropylene, MRI was the only method to observe the soft tissue cultured cells in the annular space between fibers (**Fig. 1-5B**).

2 Bioreactor Development and Design Considerations

2.1 Rationale and Goals

Experiments were conducted with a focus on developing an electrostatic encapsulation matrix that could be used to provide a stable microenvironment for cellular growth, proliferation, and differentiation while shielding the contained cells from shear forces associated flow environments. In addition, the diffusion of oxygen into encapsulates was studied with respect to diameter size and oxygen concentration. Electrostatic encapsulation technology is reproducible and controllable thus generating beads that are uniform in size, in contrast to emulsion techniques (that give particles of nanoscale dimension). Organized in 3D systems, such encapsulates were studied by measuring metabolites in the media and cell simultaneously within an NMR-compatible bioreactor. The encapsulations used in experiments described in this chapter were comprised of primary rat hepatocytes.

The metabolic energy status of the entrapped cells was monitored using *in vivo* ^{31}P NMR spectroscopy. Inorganic phosphate, ATP, sugar phosphates, phospholipid intermediates, and pH were measured to evaluate the efficiency of the bioreactor perfusion system. In addition, custom Clark oxygen electrodes were fabricated to monitor the input and output oxygen concentration of the perfusion media. Lastly, histology was performed, pre and post experiment, to assess cell viability and conditions within the encapsulate matrix.

The specific goals of this research were as follows:

1. Develop an encapsulation methodology and gelling agent to produce consistent diameters, maximum longevity of encapsulate integrity, and robust mass transfer of nutrients.
2. Extend the time course of survival of encapsulated primary hepatocytes to days, which is well beyond the longest duration of 8-10 hours described in previous studies.
3. Develop an NMR-compatible cell culture environment to enable real-time toxicodynamic and toxicokinetic observation.
4. Establish an NMR metabolomic method for elucidating the toxic mechanisms of drug-induced liver injury.

2.2 Electrostatic Encapsulation

Electrostatic encapsulation is a proven technique for immobilization of various cell types, such as yeast cells (Serp et al 2000) and mammalian cells (Chandrasekaran et al 2006). It is a first choice for immobilization in medicine due to its advantages. One of which is that it can produce alginate microbeads down to 100 or even 50 µm in diameter (Manojlovic et al 2004) in comparison with other extrusion techniques. Smaller beads offer many advantages, such as better mass transfer of nutrients and oxygen (84). Further, the technique is easy to use under sterile conditions.

The production process is performed under mild stress conditions without the use of any organic solvents that can inhibit cell activity and cause serious damaging effects. It has been proven that the application of high electric potential does not damage cells. Therefore, no loss in cell activity or viability occurs after immobilization. The rate of production of the

technique is high enough to produce microcapsules in the scale needed for bioreactor applications. In addition, the electrostatic extrusion technique has been shown to have high entrapment efficiency with almost no loss in cells during processing.

Electrostatic droplet generation (**Fig. 2-1A**) is based on the use of electrostatic forces to disrupt a liquid filament at the capillary–needle tip and form a charged stream of small droplets (Woods et al 1999). It is a complex process involving a number of parameters such as applied electrostatic potential, needle diameter, electrode distance and geometry, polymer solution flow rate, as well as properties including surface tension, density, and viscosity (Zhang et al 2009). The addition of a cell suspension within the polymer further complicates matters by affecting both polymer properties and the extrusion process (i.e. micro-hydrodynamics within the capillary via electrostatic and physical interactions of the cells (Manojlovic, 2006; Seagle, 2007). Experiments were conducted with the electrostatic encapsulation system (**Fig. 2-1B**) developed by Seagle (85).

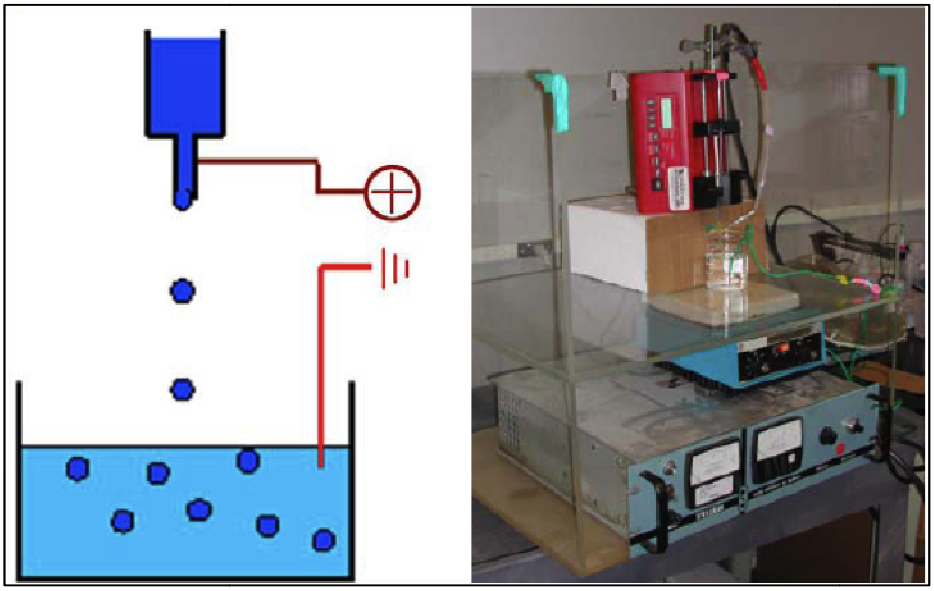

Figure 2-1 Electrostatic bead spray design (**A**) and open-front encapsulation setup (**B**).

2.2.1 Encapsulate Diameters

Encapsulations may provide stable microenvironments for cellular growth, proliferation, and differentiation while shielding the contained cells from shear forces associated flow environments and may provide an immuno-protective barrier to recipients of cells implanted in encapsulated form. Organized in 3D systems, such encapsulates can be studied by measuring metabolites in the media effluents from traditional culture plates and bioreactors. In these studies, encapsulation of the cells was utilized for maintaining large numbers of cells within a confined hydrogel architecture which would provide protection from shear forces while still allow for diffusion into and out of the construct. The guidelines for encapsulation materials and geometry were initially established as the following:

1. Matrix material should be biocompatible. No materials should be used that would be toxic to contained cells or tissues that encapsulations may be implanted into/onto.
2. Encapsulation geometry should be spherical. Spherical geometry should allow for encapsulations to stack in regular patterns while providing space between adjacent encapsulations for media flow.
3. Encapsulate radius should be no greater than maximal gas diffusion distance into the encapsulation. This standard should prevent necrotic and apoptotic products resulting from an anoxic or hypoxic core from affecting more superficial viable cells in the encapsulation.

One of the inherent difficulties in the development of bioartificial organs is designing structures that provide environments that mimic *in vivo* conditions. Diffusion distance in

bioartificial tissues and systems is one such challenge. While scalability of a system is often viewed as one of the success measures in tissue engineering, size and scalability, are often restricted by the maximum distance that nutrients can diffuse or penetrate into tissue or matrix from a media flow. The nutrient possessing the smallest diffusion coefficient, therefore, determines the maximum measurement available for determining distances between cells and nutrient sources in a bioartificial tissue or organ design. In the case of the liver, natural architecture reveal that convective flow channels are separated by a distance of no more than 100 microns (μm) (86). This relatively tight packing of hepatocytes in a highly channeled structure ensures adequate blood flow to the liver which is essential when considering that in rats, for example, the liver uses between 1/5 and 1/3 of total body oxygen consumption (87).

Historically, the problem presented by the oxygen diffusion coefficient has resulted in bioreactor designs with distance suitable to provide appropriate oxygen concentrations to cells but challenged where scalability is concerned. A possible solution that provides reasonable proximity between cells and nutrient rich media, while also allowing for greater ease of scalability, utilizes spherical encapsulations of cells in permeable hydrogels superfused with media. Such a system would employ uniformly sized spheres such that a three-dimensional array of spheres would allow for media flows to pass through the spaces created between adjacent spheres. As is the case with any bioartificial system with a linearly flowed media system, nutrient concentrations drop as media traverses over or through the matrix. This most certainly would occur in a stacked sphere system. The rate at which nutrient depletion would occur is directly related to the number of cells per unit volume that reside in the spheres. A unique difference exists for systems that use spherical

encapsulations. Because the cells are contained within the hydrogel rather than loaded on the surface, cells are not subjected to the shear forces presented by the moving flow of media. Because of this isolation from flow, encapsulated systems may utilize higher flow rates than those employed by superficially mounted cell systems. Higher flow rates would allow for higher nutrient concentrations at all distances from the flow source as compared to traditional low flow of stagnant systems.

The electrostatic encapsulator design, mentioned above, was used with the following parameters: 1) power supply voltage = 3.5 kV, 2) syringe pump speed = .714 mL/min, 3) 150mL of $CaCl_2$ gelling bath in a 250 mL beaker, and 4) distance from syringe tip to surface of gelling bath = 2.5 cm. These parameters produced sodium alginate encapsulated hepatocytes with uniform spherical radii of 250 μm, the limit of oxygen diffusion in BALs (McClelland, 2003), which is a function of its diffusion coefficient and consumption rate (**Figure 2-2A, 2-2B**).

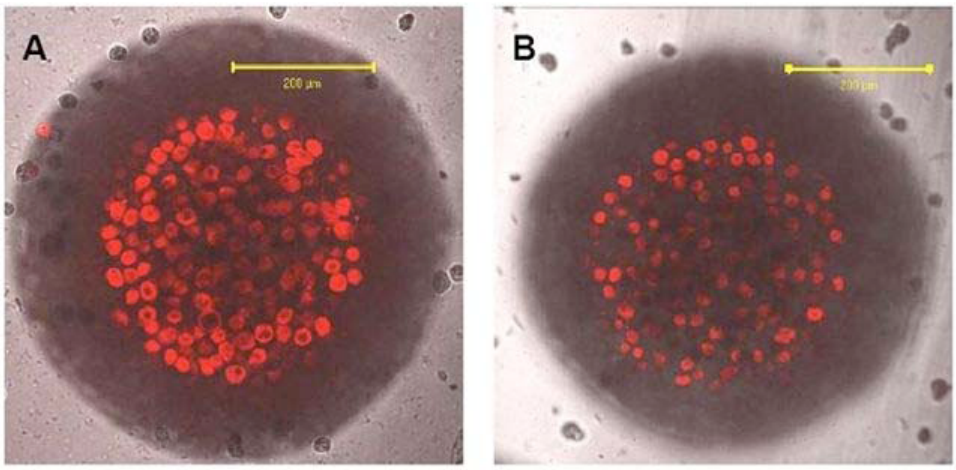

Figure 2-2 Confocal images of 10 μm thick slices through a 500 μm diameter alginate encapsulate containing $3.5x10^7$ rat hepatocytes/ml (**A**) and $2.0x10^7$ rat hepatocytes/ml (**B**). The distribution of hepatocytes in red, shows that they are tightly packed.

2.2.2 Calcium Chloride ($CaCl_2$) as a Gelling Agent

Polyelectrolyte complex systems have often been used as gel materials. Among them, calcium alginate is the most commonly employed system for its easiness in gel formation. Upon contact with polycation (Ca^{2+}), liquid alginate solutions immediately transform into gel by binding between guluronic acid blocks in alginate and Ca^{2+}. The chains in alginate polymers can be described as a varying sequence of regions termed M blocks, G blocks, and MG blocks, with no regular repeat unit. In the presence of divalent ions, water solutions of polysaccharides form hydrogels via ionic interactions between acid groups on G blocks and the chelating ions, generally Ca^{2+} (Eiselt et al 2000).

Therefore the mechanical properties of these physically cross-linked, calcium alginate gels are dependent on the proportion and length of the G blocks in a given alginate chain (Gombotz and Wee 1998). There is a hypothesis that calcium ions bind only between G blocks of more than 20 units, and at high calcium concentrations, multiple cross-linking among alginate chains is possible, thus forming a polymer network (Kong et al 2003). The network structure of these viscoelastic solids have been described by the "egg-box" model (Grant et al 1973). Gelation kinetics and mechanical properties of final Ca-alginate microbeads can also be influenced by the presence of cells. Although most studies of alginate bead production have been carried out in an excess of hardening solution (ie, $CaCl_2$) over prolonged times in order to ensure complete gelation (Martinsen et al 1989), immobilization of highly sensitive mammalian cells (eg, primary hepatocytes) can require minimal exposure to $CaCl_2$ solution. Assessment of gelation kinetics can be therefore essential for optimization of immobilization techniques for these cells in order to prevent toxic damage.

Initial encapsulation experiments utilized a bead gelling bath consisting of 150mM $CaCl_2$ in deionized water (dH_2O). This produced spherical beads with an average diameter of 500 μm and resulted in successful bioreactor perfusion experiments of up to 13.5 hours in duration, with primary rat hepatocytes. Histology of 9 μm sections of the beads prior to bioreactor inoculation revealed that the cells were bursting inside the encapsulate, leaving a significant amount of debris as shown in **figure 2-3**. The cells that did not burst were viable as reflected by the dark nuclei and vibrant color of the cytoplasm. However, this bursting reduced the overall cell density within the bioreactor as well as the SNR resulting in suboptimal NMR spectra.

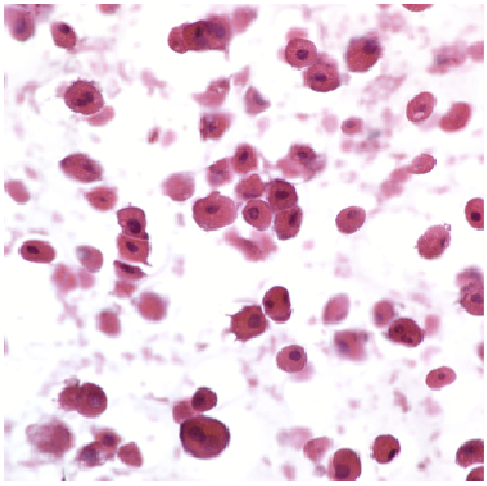

Figure 2-3 A 9 μm cryostat slice of an encapsulate stained with H&E stain (60x magnification).

Subsequent encapsulations were performed with 150 mM $CaCl_2$ in S&M, which is a solution consisting of HEPES, NaCl, KCl and NaOH. This ensured that the cells would no longer burst and also resulted in more consistent, uniformly spherical beads.

2.2.3 Barium Chloride ($BaCl_2$)

As noted in the literature, $BaCl_2$ concentrations >10 mM can be toxic to hepatocytes if exposed for 24hrs. Therefore the initial encapsulation work was performed with a gelling bath of 10 mM $BaCl_2$ in S&M. However, the resulting beads were not formed very well with most of them experiencing significant distortion. Subsequent encapsulations were performed with a 150 mM $BaCl_2$ bath that generated spherical beads more consistently than that of the 150 mM $CaCl_2$ treatment mentioned earlier. As can be seen in **figure 2-4**, this method resulted in beads containing cells as viable as those of the $CaCl_2$ method. The toxicity issue was addressed by only leaving the newly formed beads in the gelling bath for <3 minutes and immediately removing them, then rinsing with DMEM to dilute the $BaCl_2$ to a nominal concentration. The Ba-Alginate bonds began to break when the beads were perfused with DMEM causing the barium to be dissolved into the media causing encapsulates to fall apart. To combat this mass balance effect, 10 mM $BaCl_2$ was added to the DMEM, but likely due to the bicarbonate that is in the stock DMEM media as a CO_2-CO_3^{-2}-HCO_3^{-1}-H_2CO_3 pH buffer, $BaCO_3$ precipitated out of solution making the DMEM cloudy and reducing the effect concentration.

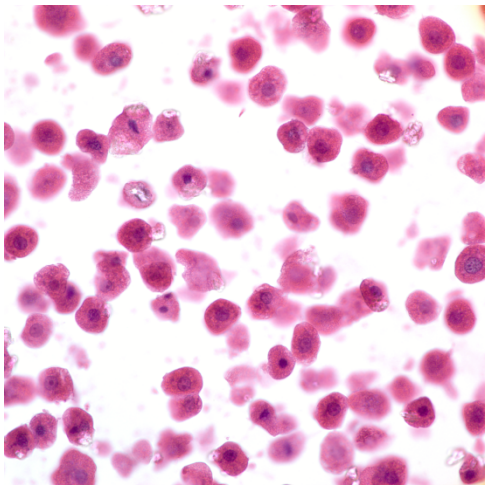

Figure 2-4 A 9 μm cryostat slice of encapsulated rat hepatocytes using 150 mM $BaCl_2$.

Other studies of hepatocytes utilized HEPES as a pH buffer in the DMEM perfusion media in the bioreactors, which has does not use the bicarbonate pH buffering system. With that in mind, various gelling bath and perfusion media combinations were prepared to determine the most reliable solution to this dilemma. Two concentrations of $BaCl_2$ and $CaCl_2$ were used as well as two perfusion medias, DMEM and HEPES. Beads were formed without cells and placed into various 15 mL centrifuge tubes containing a combination of solutions mentioned above. **Table 2-1** illustrates the outcome of this study. There was a low degree of precipitation into the media when utilizing a 10 mM $BaCl_2$ gelling bath and a high degree of precipitation with the 150 mM $BaCl_2$ treatment. In contrast, is the 10 mM $CaCl_2$ treatment resulting in no precipitation and the 150 mM $CaCl_2$ treatment with low precipitation. However, in all cases, the beads eventually fell apart due to the dissolution of the cations out of the alginate into the perfusion. This phenomenon was addressed by adding 5 mM $CaCl_2$ to the perfusion media. The final encapsulation protocol utilized a 150 mM

$CaCl_2$ in the gelling bath to stay consistent with the literature, and 5 mM $CaCl_2$ added to the DMEM perfusion media.

Table 2-1: Results of two alginate gelling solutions containing the divalent cations of barium and calcium.

Conc (mM)	$BaCl_2$				$CaCl_2$			
	DMEM		HEPES		DMEM		HEPES	
	With Beads	Without Beads	With Beads	Without Beads	With Beads	Without Beads	With Beads	Without Beads
10	^	^	^	^	-	-	-	-
	+	+	+	+	-	-	-	-
150	^	^	^	^	^	^	^	^
	+++	+++	+++	+++	+	+	+	+
Degree of precipitation: -, none; +, low; ++, medium; +++, high **Time to precipitation:** -, no delay; ^, delayed								

2.2.4 Oxygen Concentrations

Encapsulation devices are often hindered by the inability to achieve sufficient oxygen levels for sustaining long-term cell survival both *in vivo* and *in vitro*. A successful device depends on permeability, mechanical properties, immune protection, and biocompatibility (88,89). Metabolic functionality is controlled by the transport of nutrients and oxygen, with oxygen availability the primary dominant limitation (88,90). Maintenance of sufficient oxygen levels in the encapsulation device is critical to avoid local domains of necrotic and/or hypometabolic cells. There are significant limitations with most cell encapsulation devices due to internal oxygen mass transfer limitations (91).

In vivo studies measured rat hepatocyte physiological oxygen concentrations from 13% (v/v) arterial to 4% (v/v) hepatovenous, which modulate carbohydrate metabolism (92,93). Oxygen tension also plays a significant role in gluconeogenesis and glycolytic activity of hepatocytes (94,95). The cell microenvironment is dependent on both nutrient and

oxygen availability within the encapsulation device and the surrounding medium. Oxygen supply and transport can be enhanced through several means including medium sparging (96), perfusing oxygen through silicone tubing (97), minimizing encapsulation geometry (98), or using oxygen-rich membranes (99,100). Despite research efforts in these areas, oxygen transport remains one of the main limitations in maintaining cell viability and functionality.

All of the studies performed in this research were conducted with the use of a previously developed (44) gas exchange module (GEM) to oxygenate the perfusion media (**Figure 2-5**). It utilizes silastic tubing to enable the diffusion of oxygen into the media stream. Custom flow-through oxygen probes were also fabricated by Dr. Andrey Tikunov (University of North Carolina) and placed in-line with both the input and output media streams. This provided real time oxygen measurements to characterize the actual performance of the perfusion system.

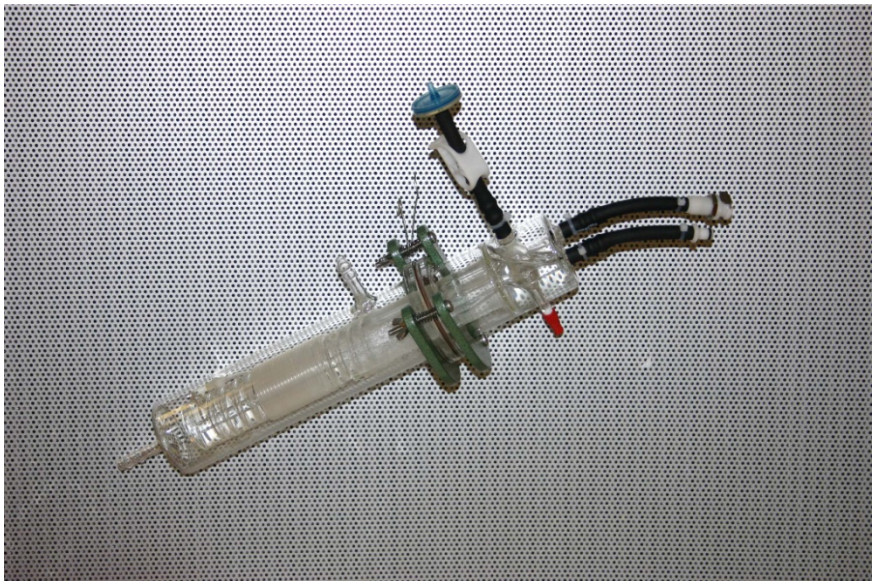

Figure 2-5 Gas exchange module (GEM)

Although the concentration of oxygen at the output of the GEM would reconcile with that of the oxygen being perfused in the GEM, it was not the concentration in the bioreactor. It was discovered that the three foot length of waterjacketed perfusion tubing extending from the GEM to the bioreactor was permeable to oxygen and affected the final oxygen concentration in the bioreactor. Initial experiments were conducted with 95% oxygen, 5% carbon dioxide as this was the prevalent gas mixture used in all of the previous studies of hepatocytes in perfused NMR-compatible bioreactors. Air, or 20% oxygen, or a mixture of 75% nitrogen, 20% oxygen and 5% carbon dioxide was used as was a third oxygen treatment using 65% nitrogen, 35% oxygen and 5% carbon dioxide. In each case the oxygen concentration was determined in the bioreactor. The various types of tubing material tested are given below. The Cole-Parmer catelog gives a nice summary of tubing gas permeabilities, but as will be described, those that list impermeable to oxygen, actually are permeable to some degree. Bev-a-line™ seems to be one that is truelly impermeable.

2.3 Iterative Design Toward the Final Fluidized-Bed Design

2.3.1 Gondola (packed-bed)

The majority of perfused NMR-compatible bioreactors are configured with both an upper and sometimes lower baffle to constrain the cells within a known region. This design has certain drawbacks, one of which is difficulty in inoculating the bioreactor with cells. The first baffle must be inserted into the NMR tube just enough to leave room above it for loading of the cells. However, when the cells are loaded and the second baffle is slid down to seal the cells within the NMR tube, the cells begin to blow past the second baffle before it can seal off the volume of cells.

This issue was addressed by Dr. Michael Gamcsik (North Carolina State University) with an NMR-compatible bioreactor design, called the 'Gondola'. This design incorporates a cylindrical, boat-like enclosure that is sealed on both ends with baffles, but has a small length-wise opening to enable loading of cells (**Figure 2-6**). The enclosure consists of polyethylene tubing that is secured to the baffles on each end with heat-shrink tubing to form a tight seal. This allows the bioreactor to be inoculated prior to sliding it into the NMR-tube, thereby preventing any cell (bead) blowout. An 8 mm NMR-compatible bioreactor was constructed using this design and several trials were executed. This is a packed-bed bioreactor, in that the gondola is fully loaded with cells to maximize the density and in turn, the SNR. Unfortunately, channeling of media occured upon perfusion with culture media, allowing the media to take the path of least resistance through the packed-bed of encapsulated cells, which caused heterogeneous distribution of nutrients and oxygen.

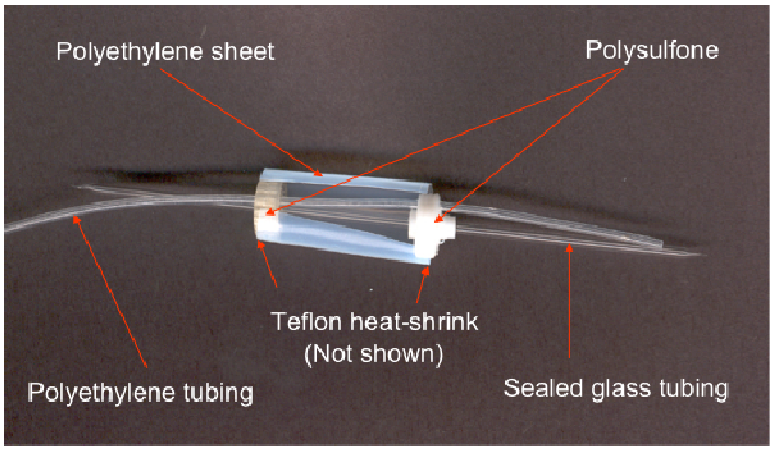

Figure 2-6: The gondola design of Dr. Gamcsik alleviated the problem of loading the bioreactor.

2.3.2 Perforated polyethylene plug

A modification of the gondola design was fabricated to alleviate the packed-bed and channeling of media. The lower baffle and gondola were replaced with a short piece of polyethylene heat-shrink tubing forming a small, cylindrical cavity that is an extension of the upper baffle whose ports have been enlarged to allow an increased rate of media flow (**Figure 2-7**). Then a porous polyethylene rod was cut the same length as that of the cavity and inserted to prevent the beads from flowing through the larger ports of the modified upper baffle. This acted as a flow distributor, typical of packed-bed BALs, which eliminated channeling (Macdonald et al., 1998).

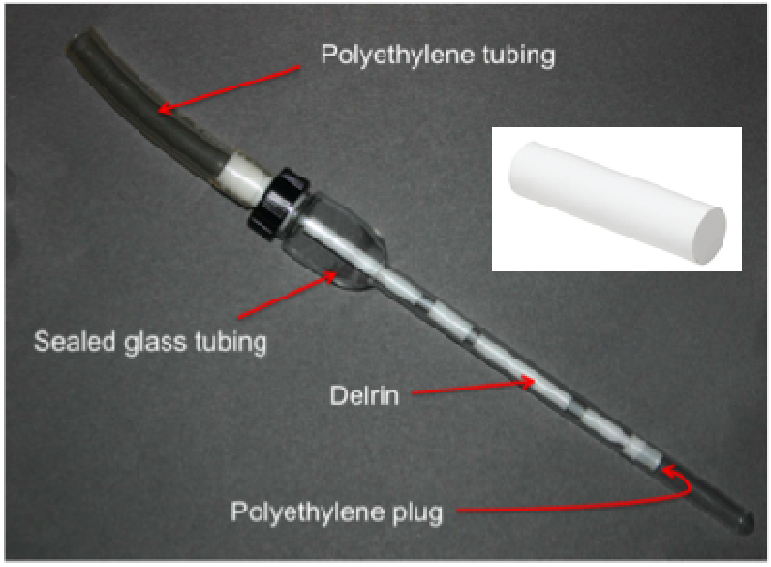

Figure 2-7: The addition of polyethylene plug acting as a flow distributor.

Although this design modification solved the channeling issue, it introduced another form of perfusion constraint. The beads began to pack up against the polyethylene plug, creating a semi-packed bed and eventually clogged most of the pours in the plug increasing

pressure and affecting outlet flow. This resulted in uneven and insufficient perfusion of media, causing both bead damage and eventual cell death due to the lack of oxygen and nutrients.

2.3.3 Fluidized-bed

The previous design attempts and experiments provided the data to fabricate a bioreactor based on a fluidized-bed principle that would allow for uniform and sufficient media flow with maximized mass-transfer of oxygen and nutrients. All heat-shrink tubing was eliminated from the design and an upper baffle was milled with outer fins and 300 μm ports (**Figure 2-8**). This allowed the beads to percolate as the perfusion media flowed from the bottom of the NMR tube to the top. The media flow pushes the beads up near the upper baffle before they begin to fall back down toward the bottom of the tube, resulting in a continuous motion of beads thus ensuring that each bead receives maximum exposure to the media. A closed loop system was used whereby only one pumphead was used to generate the media flow, and o-ring were incorporated into the cap design to guard against leaks.

Figure 2-8: The final fluidized-bed design with just a top baffle and percolating beads.

2.3.4 Flow rates

Previous studies of NMR-compatible bioreactors utilized media flow rates ranging from 2-20 mL/min (44,101), depending on the diameter of the bioreactor tube. Studies conducted with 10 mm NMR tubes were usually performed with flow rates around 8 mL/min, but these were typically packed-bed or mesh type bioreactor (Gamsick, Macuso…). Therefore, the initial studies in this research were also conducted at a media flow rate of 8 mL/min. This consistently resulted in disintegration of the beads, due to excessive shear forces, and subsequent blowing of bead debris through the ports in the baffle. A reduction in the flow rate to anywhere between 4-6 mL/min remedied the shear force issue, however, there was still the channeling problem (packed-bed designs) regardless of the flow rate.

For the fluidized-bed design, flow rates between 2-5 mL/min were utilized with differing degrees of success with the resulting degree of success being more dependent on oxygen concentration than flow rate. In addition, an interesting phenomenon was observed

when modifications were made to the length of the bioreactor insert. A shorter insert translates to a greater distance between the end cap and the bottom of the NMR tube, which then enables increased media flow rates. Therefore maximum allowable flow rate is dictated by the height of the end cap. Optimum configuration allows for minimal bead volume while ensuring sufficient media flow for maximum mass transfer of oxygen and nutrients.

2.3.5 Materials

The NMR-compatible bioreactor is made up of several types of tubing that have different attribute requirements, depending on its use in the bioreactor. One of those uses is for the delivery of media without loss of oxygen, meaning that the tubing must be oxygen impermeable. Polyethylene (PE) has long been recognized as an engineering plastic that exhibits a high degree of inertness, making it attractive for use in markets such as food and beverage, laboratories, and chemical processing where leaching or permeability would present risks. Polyethylene is also one of the lower-cost plastic materials and satisfies many requirements that call for inexpensive, lightweight tubing. Initial NMR-compatible bioreactors were constructed with PE tubing, however it presented several problems during bioreactor fabrication and use. It is one of the more pliable tubing products used in laboratories and therefore occasionally became stretched and narrowed to the point where media would no longer flow through it. In addition, it was easily crimped during repeated usage of the bioreactor. Also, it cannot be autoclaved and must be sterilized by ethanol or ethylene oxide. These problems called for a more robust tubing product that was also impermeable to oxygen.

Fluorinated Ethylene Propylene (FEP) tubing is a semi-rigid product that holds up well to usage and repeated autoclaving, in addition to having the next lowest oxygen permeability with respect to that of PE tubing. Both the input and output lines were replaced with this tubing product and various studies were conducted, with and without hepatocytes, to characterize its usage in the NMR-compatible bioreactor. Of most interest was its oxygen permeability therefore several oxygen experiments were conducted to determine the actual oxygen concentration at several points within the perfusion system, such as 1) the GEM output, 2) inside the NMR tube, and 3) bioreactor output. This enabled a true determination of potential oxygen concentration drops throughout the bioreactor loop.

A third tubing was test that was comparable to FEP, Teflon or PTFE. It too was listed as being impermeable to oxygen. Although minimal oxygen permeability was detected with FEB and PTFE compared to PE, both exhibited some decrease of permeability, and must be considered in conjunction with flow rate and tubing length from the GEM to the bioreactor for accurate oxygen concentration for the perfused cells.

2.3.6 Open vs Closed System

Initial experiments were conducted with an open-system configuration, meaning that there was not a continuous loop throughout the bioreactor perfusion system. Basically, a pump head was dedicated to each of the media lines, input and output, to operate in a push-pull fashion. Various combinations of tubing sizes and pump speeds were trialed to determine the optimum parameters. The original bioreactor loop configuration consisted of equally sized, inside diameter (ID) and outside diameter (OD), media perfusion lines. With both pump speeds set the same, the beads packed under the upper end cap and eventually

blew through its ports. A similar action was observed when the output line pump speed was set both higher and lower than the input line pump speed.

This open-system was abandoned for a closed-system configuration for the basic reasoning that if the system was truly closed, the media could be pushed through the loop with only one pump. The first attempt at this configuration proved disastrous as described above. The experiment began with observing the loop outside the NMR magnet and everything appeared to be just fine, the media was flowing through the system effortlessly and the output line was taking up the media as it flowed upward in the NMR tube. Therefore the bioreactor was placed into the NMR magnet and an overnight acquisition was setup and initiated. Upon returning to the lab the next morning, a pool of media was discovered directly beneath the probe of the magnet. Apparently the media had flowed completely to the top of the NMR tube and began dripping down the outside of the tube and inside the probe. Unfortunately the 400 MHz 10 mm NMR probe had been damaged beyond repair and was destroyed – a $5K experiment. My advisor was very unhappy. Further investigation of the loop revealed that the system was not truly closed afterall. The top of the NMR tube was not sealed completely therefore air was escaping, allowing the media to rise without being exported through the output line. A subsequent design change that incorporated two o-rings around the top cap of the NMR tube remedied this problem and all of the remaining studies were ran without any overflow issue. Several iterations of input/output line sizes and pump speeds were tried before coming up with the final closed-system design, described in the next section. This made for a more convenient, streamline perfusion system to be used, with just one one pump head with associated tubing used to generate the perfusion.

2.4 Concluding Remarks and Final Design

NMR-compatible bioreactor experiments enable the detection of intracellular metabolites. This is of particular importance because some charged species can not pass from the cytoplasm into the extracellular space thereby preventing detection in media-only analysis – or footprinting. The media analysis can demonstrate viability and functionality but a more complete understanding of metabolic outcomes will require NMR analysis of *in vitro* cell extract preparations.

The final NMR-compatible, fluidized-bed bioreactor consists of a 10-mm NMR tube with a milled Delrin^{TM} fixture containing an end cap with 300 μm ports that retain the encapsulated cells. The top cap is sealed with two o-rings and is connected to two water-jacketed (norprene) lines with internal FEP or PTFE tubing that is maintained at 37º C via a water bath. FEP or PTFE tubing provides input of media, which extends to the bottom of the NMR tube and a second FEP tube is used to remove the media as it reaches the top portion of the NMR tube.

3 NMR-compatible Bioartificial Liver for Real-Time Toxicokinetics and Toxicodynamics

The difference between pharmaco- and toxico- dynamics/kinetics is one of dose. Conventional approaches to determine the pharmaco- or toxico- kinetics of drugs consists of the use of body fluids (urine, plasma) and tissue to obtain drug and metabolite concentrations. These concentrations can be measured using HPLC, GC/MS and NMR (102). However, it requires samples to be collected at pre-determined intervals and often sacrifice of the animals (103). *In vivo* NMR enables the noninvasive monitoring of ^{13}C-labeled xenobiotics to determine the pharmaco-kinetics and/or toxico-kinetics of drug action (104). This can be accomplished with the use of surface coils for *in vivo* measurements in rat (82,105). However, this technique is limited by coil positioning and signal detection depth. The use of NMR-compatible bioartificial livers (BALs) provides a controlled environment of cell culture that allows for greater SNR. Unfortunately there are limitations on longevity (~2hrs) due to non-physiological conditions (25°C) and the temporal resolution (~33min) is not frequent enough to capture dynamic toxicokinetic activity (49). Subsequent designs have improved on the longevity and temporal resolution, however these improvements are still not sufficient enough to capture real-time toxico-kinetics over the entire course of drug activity. We have developed an NMR-compatible BAL that sustains primary rat hepatocytes in physiological conditions for at least 28 hours, with a cell density of 3.5x107cells/mL (see Chapter 4).

In this study, a rat hepatoma cell line (JM1) was utilized to observe real-time toxicodynamics and toxicokinetics of bromobimane (BrBi) and acetaminophen (APAP). Glutathione (GSH) is a tripeptide (γ-glutamyl-cysteinyl-glycine) as shown in **Figure 3-1A**, wherein cysteine is the rate-limiting amino acid for GSH synthesis. Glutathione is a primary anti-oxidant, protecting cells from toxicants (i.e. free radicals) and is also the major non-protein thiol in many biological systems. Bromobimane is a highly reactive compound used as a derivatizing agent in HPLC analysis of glutathione. **Figure 3-1B** illustrates the conjugation of BrBi with GSH. Once GSH is depleted beyond 70% of steady-state levels, BrBi attacks proteins inactivating enzymes essential for normal cellular function, and ultimately will kill the cell. Glutathione has been shown to be a key component of drug resistance in cancer (106). Isotope-labeled, [3,3'-$^{13}C_2$]cystine was utilized in the perfusion media to follow the accumulation of GSH, then various doses of BrBi were administered to the cells to observe its effect on GSH and GS-Bi conjugates. Previous ^{13}C NMR studies of GSH metabolism in cancer cells were conducted with 41-min temporal resolution (107). Our study reports the first time a 1-min temporal resolution has been achieved with ^{13}C NMR for toxicokinetic and toxicodynamic studies. This model will have significant impact on predictive toxicology experiments, as it will enable the real-time observation of drug activity and metabolism that has been previously undetectable.

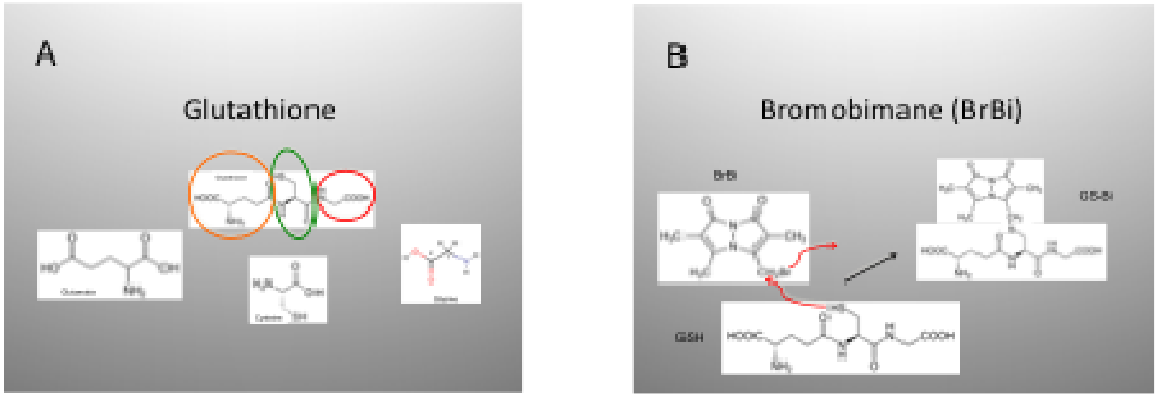

Figure 3-1 (**A**) Glutathione, a tripeptide (γ-glutamyl-cysteinyl-glycine). (**B**) Bromobimane, a highly reactive compound.

The new fluxomic method that is non-invasively and dynamically obtained was also applied to study acetaminophen (APAP) toxicity and the APAP-induced cascade of toxic events (**Figure 3-2**). Cytochrome P450 enzyme activity is required for NAPQI formation from APAP and there are no previous reports of P450 in JM1s. Three APAP doses were tested, 10, 20, and 40 mM dissolved in the culture media, and the the fluxome and metabolome analyzed to determine the sub-lethal effects of APAP toxicity. The cascade of toxic biochemical events were elucidated from the difference in the uptake curves of u-^{13}C-glucose between controls and the different APAP doses. At the end of the experiment, the cells were extracted and analyzed by high resolution 1D ^{1}H and 2D ^{1}H-{^{13}C} HSQC NMR spectroscopy to determine if P450 activity was triggered by the toxic dose of APAP.

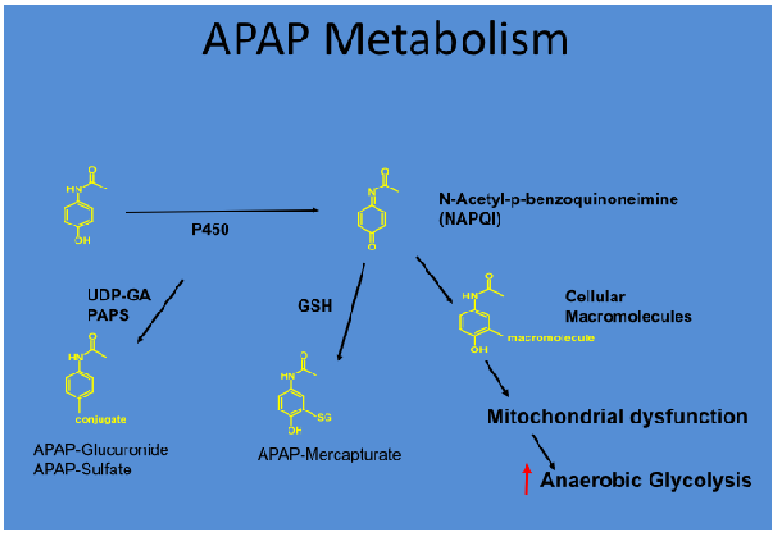

Figure 3-2 Acetaminophen metabolism and toxicity pathways.

3.1.1 Acetaminophen (APAP)

APAP is one of the most commonly used nonprescription analgesics in the United States. Of the 76% of Americans that reported using nonprescription products in the Third National Health and Nutrition Examination Survey (NHANES III), 36% reported using APAP (108). An estimated 2,000 cases of acute liver failure occur per year and APAP is the most common identifiable cause. Although spontaneous recovery is highest with APAP caused morbidity compared to other drugs and other causes of acute liver failure, the mortality from APAP induced severe hepatotoxicity remains at 20% and 10% require liver transplantation. Thus, despite high rates of spontaneous recovery and the availability of an antidote (N-acetylcysteine) APAP induced liver failure remains an important healthcare problem. The nutritional status of cysteine is important to investigate because it is a nutrient prodrug of the antioxidant, glutathione (GSH). Fasting exacerbates APAP toxicity by depleting GSH that is required for detoxication of APAP-derived reactive metabolites (109).

3.1.2 Fluxomics

Metabolism is dynamic and can be characterized by mass balance equations, which depend on the flux rates and concentration of the various metabolites, defined by the boundary conditions of the biological system. The comprehensive measurement of the flux rates is fluxomics. Intermediary metabolism is the first detector of change with a phosphorylation-driven reaction during signaling with consumption of ATP, or a toxic inhibitor of specific reactions blocking flux, and therefore, is very sensitive to non-lethal effects of drugs. In addition, most flux rates are determined at steady-state, while most toxicants, by definition, affect metabolism and perturb steady-state. In fact, the mechanism of toxic action of xenobiotics is defined by a cascade of pathological events leading to cell death. This can be comprehensively elucidated using fluxomics, non-invasively, in real-time.

3.1.3 Methods

NMR supplies were obtained from multiple vendors. Sodium alginate, calcium chloride, perchloric acid, sodium citrate, sodium chloride, potassium chloride, magnesium sulfate, HEPES, bovine serum albumin, and 3-(trimethylsily)propionic-2,2,3,3-d_4 acid (TSP) were purchased from Sigma Chemical company (St. Louis, MO). Mono and dibasic phosphate, and barium chloride was purchased from Mallinckrodt (Paris, KY). DMEM, insulin, penicillin, streptomycin, and fetal bovine serum was purchased from Invitrogen (Carlsbad, CA). The 10 mm NMR tubes were purchased from Wilmad Labglass Inc. (Miamisburg, OH), while Norprene™ and Silastic™ tubing, tube connector, peristaltic pump, were from Cole Parmer (Vernon Hills, Illinois). The water bath and 500 ml Gibco™ reservoir culture bottles were from Fisher (Pittsburgh, PA). Bioreactor end pieces were

manufactured from Delrin™ and assembled as previously described (110). Materials for the bioreactor life support units were previously described in earlier work (44).

3.1.4 JM1 Cell Culture

JM1 rat hepatoma cells (Michalopoulos Lab, University of Pittsburg) were cultured in DMEM medium (Invitrogen, 3 g/L glucose) supplemented with 10% fetal calf serum, 100 units/mL penicillin and 100 μg/mL streptomycin (Invitrogen). Cells were grown in T150-flasks (Fisher) at 37°C in a 95% air/5% CO_2 incubator. For bioreactor experiments, cells were trypsinized, washed in PBS and electrostatically encapsulated.

3.1.5 Encapsulation

Cells were encapsulated using an electrostatic bead generation apparatus described previously (111) with modifications (110). Briefly, JM1 cells at density of 1 x 10^9 cells/ml were suspended in 2% sodium alginate solution at a 1:1 ratio. The resulting 1% alginate solution containing 5 x10^8 cells/ml was put in a 1cc syringe fitted with a 24 gauge angiocatheter. The angiocatheter was pierced at the hub with a 27-gauge needle, which served as the positive electrode for the electrostatic casting process. The syringe was placed in a syringe pump (Braintree Scientific BS-8000, Braintree, MA) and arranged such that as droplets were ejected from the angiocatheter they would fall orthogonally into the 150mM $CaCl_2$ or $BaCl_2$ saline solution bath (6.7 mM KCl, 142 mM NaCl, HEPES 10 mM at pH 7.4) at 4°C. Encapsulates were transferred to culture media within two minutes to avoid excessive exposure to calcium. The distance from the angiocatheter tip to the surface of the $CaCl_2$ or $BaCl_2$ solution was fixed at 2.5 cm. Pump flow rates were set within the range of

0.75 to 1.5 mL/min. A grounded electrode was immersed in the $CaCl_2$ receiving bath. When the syringe pump was turned on, in the presence of the high electrostatic potential (ca 4-6 kV), the sodium alginate solution was pulled away from the angiocatheter tip as tiny droplets that polymerized into solid calcium alginate immediately upon contact with the $CaCl_2$ saline solution.

3.1.6 In Vivo ^{31}P and ^{13}C NMR Spectroscopy

In vivo ^{31}P and ^{13}C NMR experiments of the JM1 cells were performed on a narrow-bore 14.1T Varian INOVA equipped with a 10mm broadband probe (Venus Probes, Livermore, CA). The receiver frequency of the probe was tuned to ^{31}P at 242.78 MHz and ^{13}C at 150.92 MHz. ^{31}P time courses were acquired before and after the drug treatment using a TR=2s, nt=2028 and a 90° flip angle. ^{31}P spectra were zero filled to 40,000 points and line broadened 15 Hz using Gauss-Lorentz apodization. NMR data was processed off-line with ACD/Specmanager software (ACD/Labs, Toronto, Ontario, Canada). ^{31}P metabolites were identified using α-NTP (-7.5 ppm) as an internal reference. ^{13}C time courses at 1.2 min temporal resolution were acquired during the drug treatment using a TR=2s, nt=256 and a 90° flip angle.

3.1.7 Drug Treatment

A 2 mM solution of bromobimane was prepared by bringing 45 mg of BrBi into solution with 500 µl of DMSO. 100µl of BrBi was added to 50ml of perfusion media to produce a 400 µM dose (50 µM in figures). A 2M dose (500 µM in figures) was prepared in 50ml of media in a similar fashion by adding the appropriate amount of 2mM BrBi solution.

Figure 3-3 illustrates the experimental protocol whereby an initial 15-min ^{31}P NMR spectrum was acquired to determine the viability of the JM1 cells, followed by 30-min ^{13}C spectra while glutathione was synthesized overnight. Another 15-min ^{31}P NMR spectrum was acquired, prior to the drug treatment to ensure the cells were still viable, then the input media stream was switched from the non-drug media to the BrBi-dosed media for 10 minutes then switched back to the non-drug media. ^{13}C NMR spectra were obtained, at 1-min resolution, throughout the dosing time period, up to 2 hours total acquisition of the time course with this temporal resolution, afterwards a final ^{31}P NMR spectrum was acquired to determine the effects of the drug treatment.

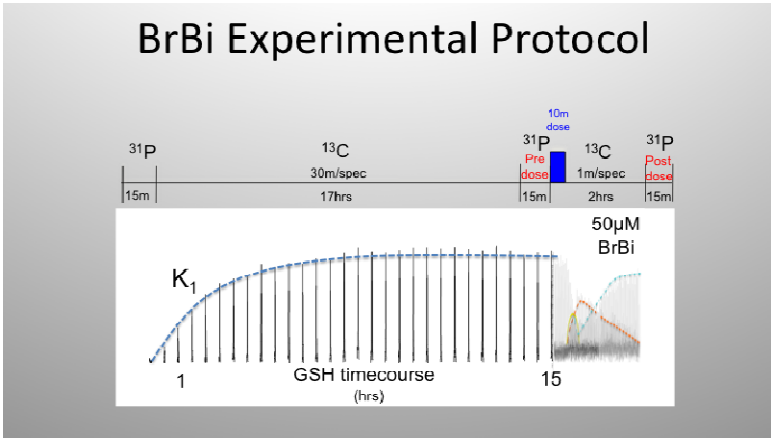

Figure 3-3 Experimental protocol (top): 30-min spectra obtained over nite for 15 hrs followed by 1-min drug treatment temporal resolution (bottom spectral time course).

APAP experiments were conducted with three doses, 2.5 mM, 25 mM, and 50 mM. A 1 M solution of APAP was prepared by bringing 302 mg of acetaminophen into solution with 2 ml of DMSO. The 2.5 mM dose was produced by adding 18.75 µl of APAP and 357.25 µl of DMSO to 75 ml of DMEM, resulting in a 0.5% DMSO concentration. The other two doses, 25 mM and 50 mM, were prepared in a similar fashion. The experiments protocol

(**Figure 3-4**) was similar to that of the bromobimane experiment except three dosing protocols were concatenated one behind the other, over the course of three days. Each dose was administered in 75 ml of perfusion media for 3 hours then the perfusion was switched back to the non-drug media to allow the glutathione to reach steady state before administering the next dose of APAP.

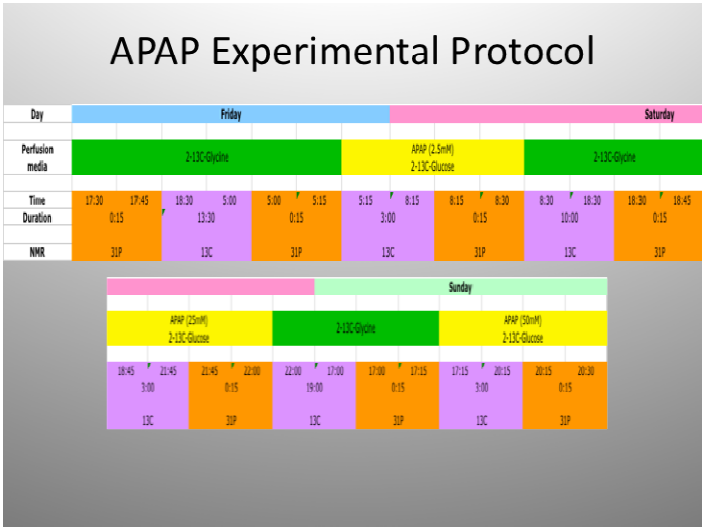

Figure 3-4 Three doses of acetaminophen drug treatment with ^{31}P and ^{13}C NMR acquisitions.

3.2 Results

The bioreactor is inoculated with encapsulated JM1 cells and perfused with media containing L-[3,3'-^{13}C2]cystine. The metabolic model of glutathione synthesis and bromobimane-glutathione conjugation is shown in **figure 3-5**, along with the various rate constants. Glutathione is synthesized in two adenosine triphosphate-dependent steps:

- First, gamma-glutamylcysteine is synthesized from L-glutamate and L-cysteine via the enzyme gamma-glutamylcysteine synthetase (*a.k.a.* glutamate cysteine ligase, GCL). This reaction is the rate-limiting step in glutathione synthesis.

- Second, glycine is added to the C-terminal of gamma-glutamylcysteine via the enzyme glutathione synthetase.

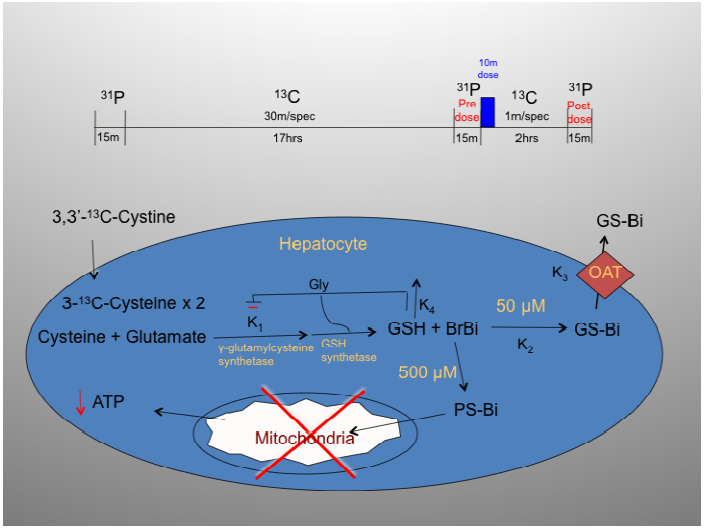

Figure 3-5 The metabolic model of bromobimane-glutathione conjugation and excretion showing the various rate constants involved. GSH, glutathione; K1b, GSH synthetic rate; K1b resynthesis, K2, GS-Bi conjugation rate, K3, GS-Bi excretion; BrBi dose, AUC.

The toxicodynamics for the two doses of bromobimane (50 µM, 500 µM) is shown in **Figure 3-6**. A 15 min ^{31}P spectrum is obtained prior (pre-dose) to switching the perfusion media to ^{13}C-cystine and bromobimane (BrBi) showing that the cells are still viable after the overnight perfusion. A subsequent 15 min ^{31}P spectrum is also acquired after (post-dose) the drug treatment and as can be seen for the 50 µM drug treatment, the viability of the cells has not changed, indicating that the 50 µM BrBi dose is non-lethal. The bar graph shows no significant change in ATP and a little change in glycerophosphocholine (GPC), which reflects the lipids of the cell membrane. However, the toxicity of the 500 µM BrBi dose results in significant cell death as represented its post-dose spectrum. The x-NTP peaks are

no longer visible, thus indicating that the 500 μM dose is lethal. This is also reflected in the bar graph and the change in GPC indicates there is major cell membrane damage.

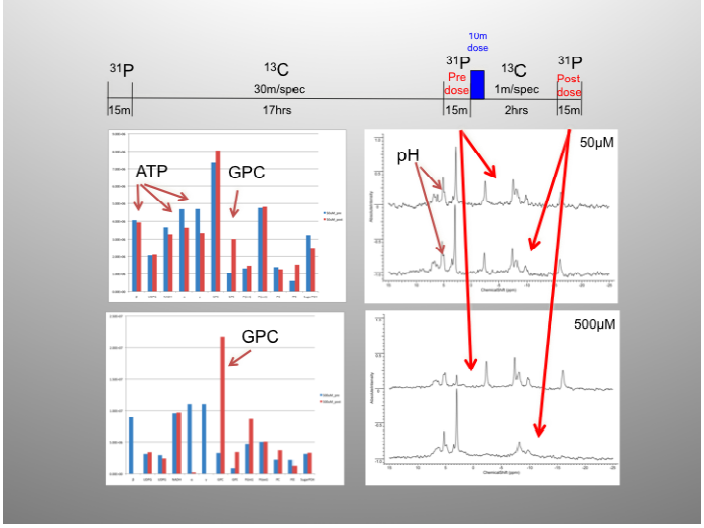

Figure 3-6 Experimental protocol and ^{31}P NMR spectra of each bromobimane treatment. Bar graphs illustrate change in metabolites.

The ^{13}C spectra are obtained at 30 min intervals to observe the uptake of L-[3,3'-$^{13}C_2$]cystine, a precursor to glutathione (GSH), which reached *^{13}C isotopic* steady-state (i.e., no change in ^{13}C fractional enrichment) in 7 hrs during overnight perfusion as shown in **figure 3-7**. The differential equations (107) are solved for *metabolic* steady-state (i.e., no change in metabolite concentrations) resulting in the ^{13}C labeled GSH concentration equation. The uptake curve, K_1, is therefore fit with the equation $y = (1-e^{-kt})$, resulting in GSH-$k_{1a} = 0.4263h^{-1} \pm 0.785$ for both time courses used in the 50 μM BrBi doses since equivalent media concentrations are used in both experiments. A representative time course is shown in **figure 3-7** and the associated curve fit from which the kinetic parameter, K_1 was obtained. Unfortunately the 500 μM dose had a decrease in GSH signal after a plateau was

reached and was not used. This rate constant can then be utilized to determine the flux, which is reported in μM/h/10^6 cells. The total glutathione concentration, $[GSH]_T$, could not be determined from this experimental protocol as the study would have to be terminated once GSH reached steady-state, to obtain the cell extracts, which is a destructive process, and would not permit the entire dosing phase of the protocol (**Fig. 3-5**, top) to be performed. The $[GSH]_T$ shown was previously determined for JM1 cells (62), however it was conducted with a 2D cell culture which does not translate to the 3D perfusion environment of the fluidized-bed bioreactor utilized in the present experiment.

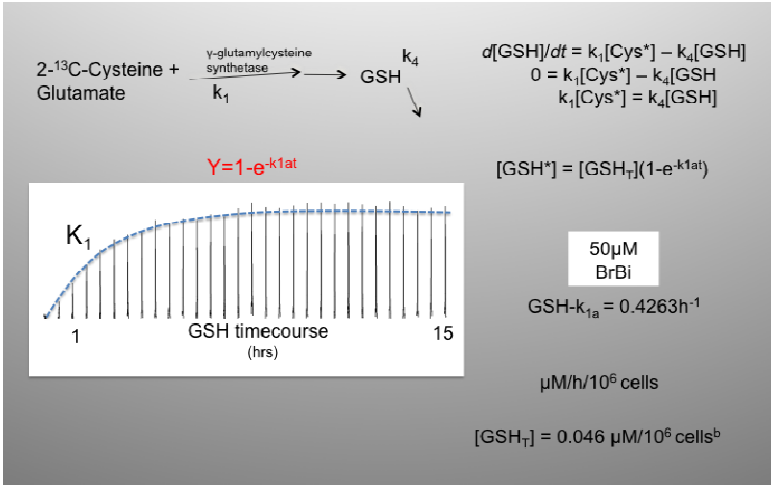

Figure 3-7 Overnight ^{13}C timecourse and equations utilized to fit the uptake curve of of L-[3,3'-$^{13}C_2$]cystine and its subsequent incorporation into [3-^{13}C-cysteinyl]glutathione (GSH).

The flux is fit from the growth and decay curves depicted in **figure 3-8**. The solid line represents the pulse-chase experiment of BrBi and ^{13}C-cysteine, lasting about 20 mins, as well as the concentration of BrBi. The cells were perfused for 10 min with the toxicant then the perfusion was switched to media containing L-[3,3'-^{13}C2]cystine only. During the pulse-chase experiment, ^{13}C spectra are obtained at 1 min temporal resolution which is sufficient to

determine the toxicokinetics of diffusion of the toxicant, bromobimane, bromobimane dose, glutathione-bimane conjugation, and gluthione-bimane excretion in real-time. The area under the curve (AUC) was utilized to calculate the 50µM and 500µM BrBi dosage concentrations of 114 and 418, respectively. The reaction is spontaneous and represents the diffusion of BrBi into the bioreactor and the bead taking about 6 mins to fully react with all of the GSH. For the 50µM dose the decay curve, k_2, is fit with the equation $y = e^{-kt}$ resulting in GSH-k_2 = 2.17h^{-1} whereas the glutathione-bromobimane conjugation curve, k_{3a}, is fit with the growth equation, $y = 1- e^{-kt}$, resulting in GS-Bi- k_{3a} = 2.74h^{-1}. The decay curve, k_3, is found experimentally and represents the export of the GSH conjugate from the cells and fitting the curve with the same decay equation, $y = e^{-kt}$, results in GS-Bi-k_{3b} = 1.1469h^{-1}. The L-[3,3'-^{13}C2]cystine label is taken up again as illustrated by GSH-k_{1b}. This curve was fit with the previous growth equation, $y = 1-e^{-kt}$, resulting in GSH-k_{1b} = 1.3501h^{-1} which is faster than the initial rate of growth, GSH-k1a, by a factor of 3. As indicated previously the 500 µM dose resulted in cell death therefore none of the subsequent rates can be determined for that experiment.

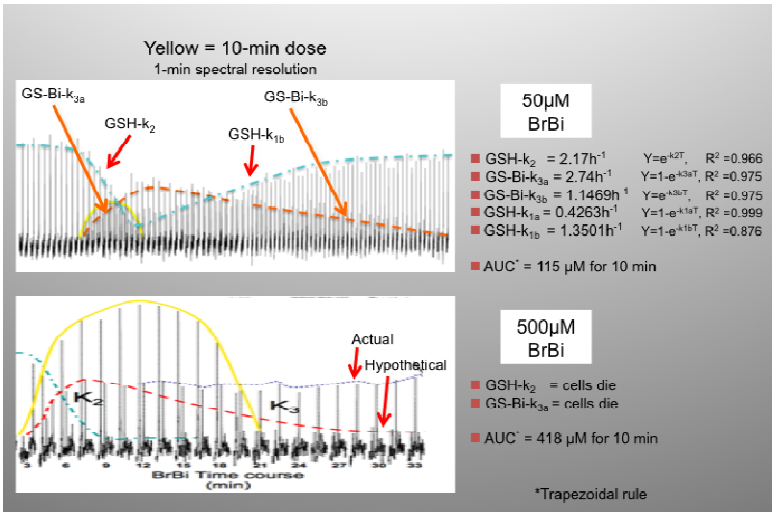

Figure 3-8 Toxicokinetics of bromobimane drug treatments.

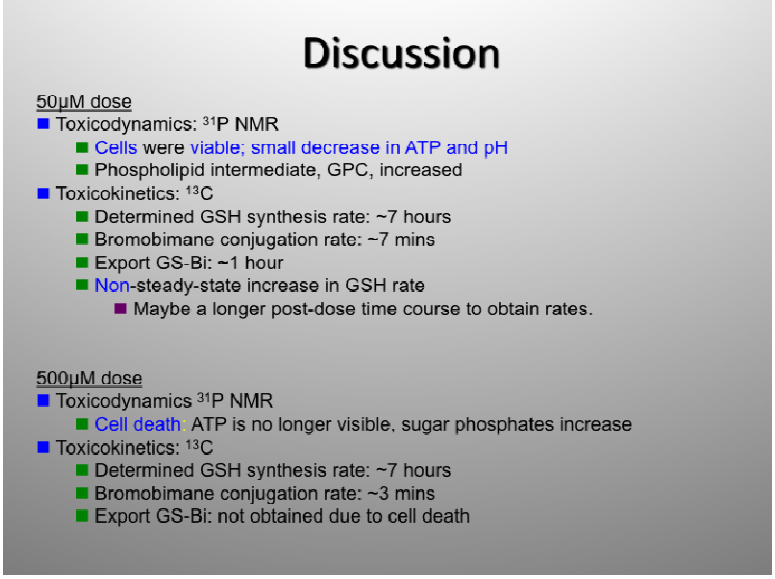

Figure 3-9 Summary of toxicokinetics study

For the acetaminophen study, the bioreactor is inoculated with encapsulated JM1 cells and perfused with media containing L-[3,3'-^{13}C2]cystine just like that of the bromobimane study. However, the experimental results are in dark contrast to that of the bromobimane experiment. **Figure 3-10** shows the 31P NMR spectra for all three dosing regimes, **A)** 2 mM, **B)** 25 mM and **C)** 50 mM. As seen in the pre-dose and post-dose spectra (**Fig. 3-10A**), there is no effect for the 2 mM APAP treatment and little effect for both the 25 mM and 50 mM APAP treatments (**Fig. 3-10B,C**). For the latter two treatments x-NTP concentrations drop a bit after dosing.

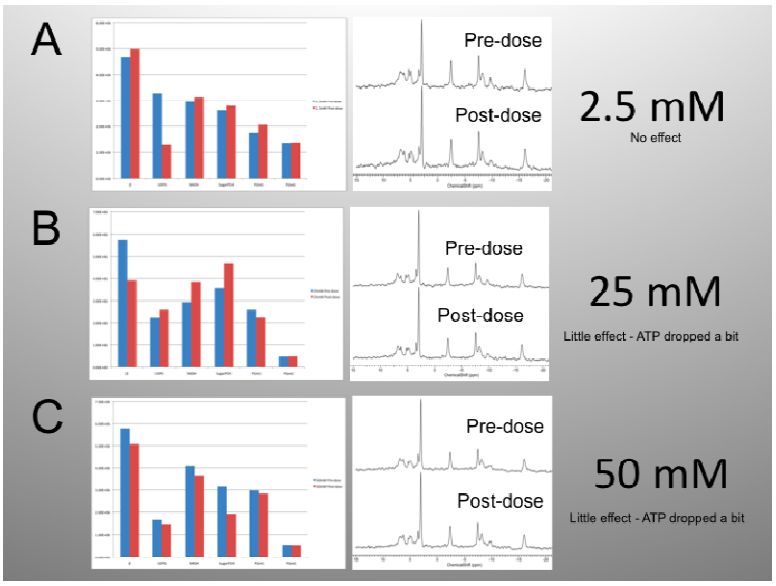

Figure 3-10 ^{31}P NMR spectra pre/post APAP dosing, A) 2 mM, B) 25 mM and C) 50 mM.

Figure 3-11 illustrates the ^{13}C NMR toxicokinetics of glutathione during the various acetaminophen treatments. Since the APAP treatment media contains ^{12}C-cystine and not L-[3,3'-^{13}C2]cystine, what is shown is the washout of the ^{13}C-labeled [GSH]. The equations are with respect to GSH synthesis and conjugation with N-acetyl-p-benzoquinone imine (NAPQI). The GS-NAPQI conjugate will only be formed if there is cytochrome P450 enzyme activity. Since there is no P450 activity, the rate constant, K_3, is negligible and therefore the rate of ^{13}C-labeled[GSH] washout is equal to the rate, K_1, of ^{12}C-cysteine incorporation. An interesting observation is the sinusoidal dampened oscillation of the washout that is attributable to either the peristaltic motion of the perfusion pump or homeostasis. However, the oscillation was still present after stopping the pump therefore a future investigation into homeostatis of GSH synthesis is warranted.

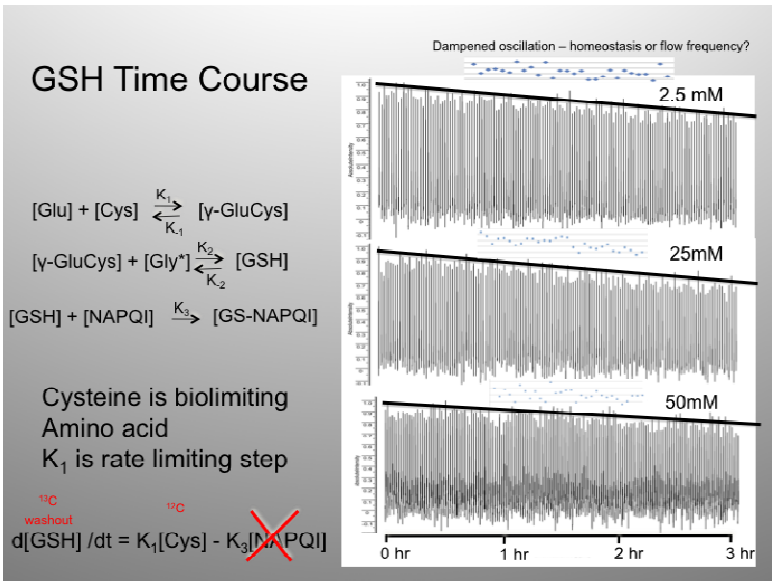

Figure 3-11 Toxicokinectics of APAP drug treatment and equations representing GSH-NAPQI conjugation.

The aim of this study is to determine if JM1 hepatoma cells have sufficient P450 activity to metabolize APAP through its toxic pathways. Several pathways are targeted as shown in **figure 3-12** to determine how JM1s are metabolizing acetaminophen. Analysis of the media with ^{1}H NMR indicates that the toxic reaction, #1, does not occur implying no P450 activity. The effect of NAPQI on the TCA cycle, #2, is negligible as shown in the ^{31}P spectra (**Fig. 3-10**) indicating no drop in ATP. A drop in ATP would result in a positive feedback on glucose that would then be converted to pyruvate, ultimately feeding into the TCA cycle to produce more ATP. However this does not occur during APAP dosing and pyruvate is converted to lactate instead. Glucose consumption and lactate production rates are determined from the ^{13}C NMR spectra of the bioreactor during drug treatment.

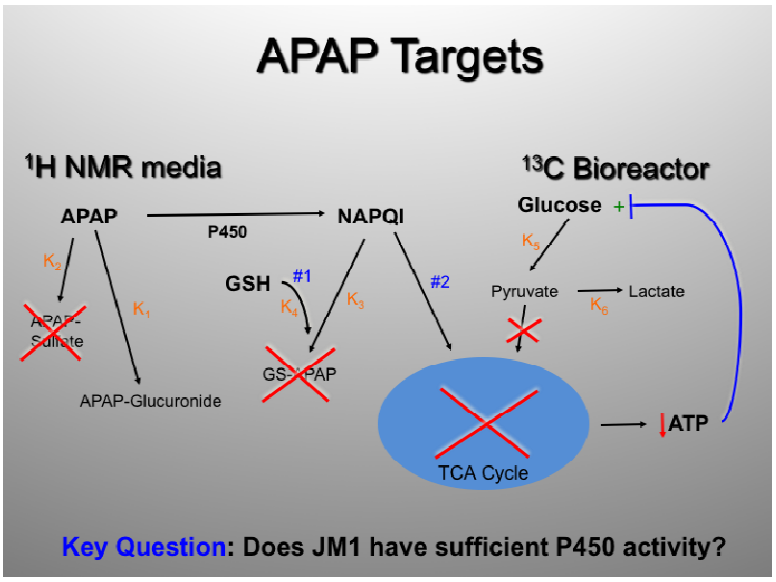

Figure 3-12 Targeted pathways of acetaminophen metabolism.

The media is also analyzed for the APAP-Glucuronide conjugate that is formed during non-toxic metabolism of APAP. **Figure 3-13A** is a ^{1}H NMR spectrum of the 50 mM APAP control media. The single peak represents the 1 proton of β-glucose (22.5 mM), whereas the two peaks represent the 2 protons of APAP (7.8 mM). Of interest is the glucuronide peak that is due to the effect of albumin binding as a result of the 10% fetal bovine serum (FBS) in the media (112). There is no increase in the glucuronide concentration, as seen in **figure 3-13B,** thus indicating there is no measureable metabolism of APAP. There is also a delayed washout of APAP (~ 1hr) when switching to non-drug media. This is unexpected and could be due to APAP binding somewhere in the bioreactor perfusion system.

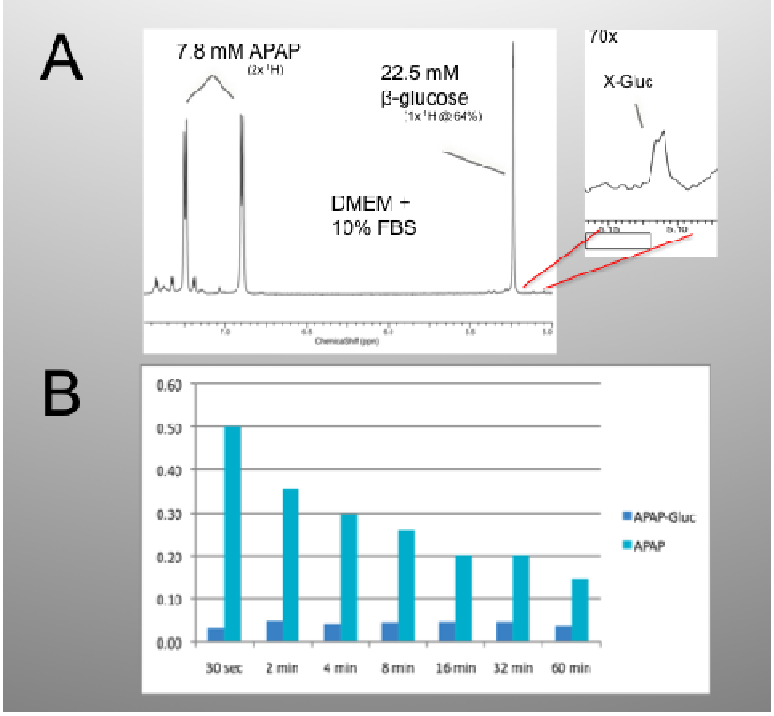

Figure 3-13 Media analysis of APAP metabolites by ^{1}H NMR.

The glucose consumption and lactate production rates are determined by fitting the plots shown in **figure 3-14A**. Of initial notice is that the slope of the lactate plot appears to be fairly equal and opposite to the slopes of α-glucose and β-glucose. There also appears to be no significant difference in rates between the three APAP treatments. The actual rates, given in **figure 3-14B**, confirm that the lactate production rates are approximately equal to the sum of the two glucose consumption rates for each of the treatments. These rates are also in alignment with that found in a previous study of JM1 cells (62).

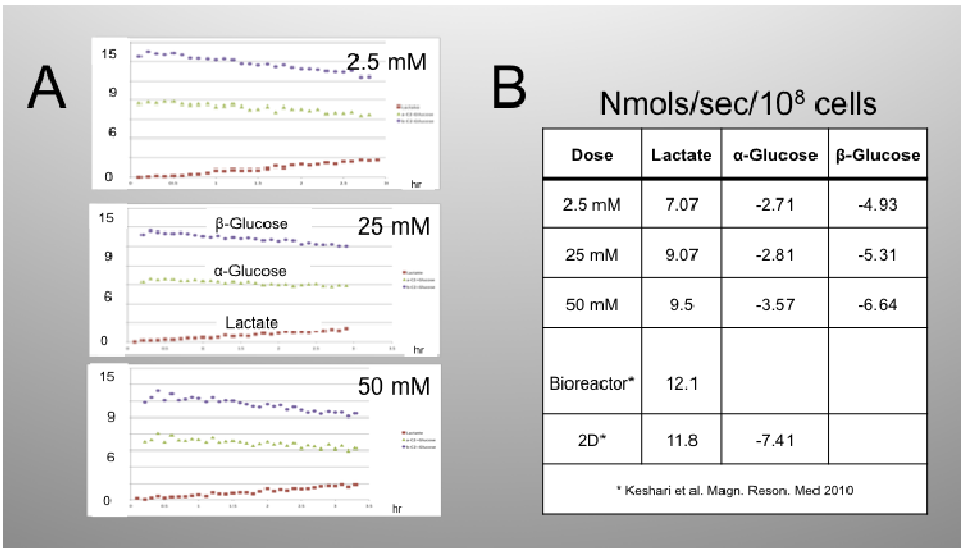

Figure 3-14 Glucose consumption and lactate production

3.3 Discussion

The before and after ^{31}P NMR spectra of the 50μM BrBi dose indicate that the cells are viable and their biochemistry has not changed over the course of the experiment (~28hrs). The JM1s were just as viable at 28hrs as they were at the beginning of the experiment, which indicates that subsequent drug-dose studies could have been conducted with the same cells. The toxicokinetics obtained from the ^{13}C NMR spectra determined the glutathione synthesis rate to be 7hrs, whereas the bromobimane conjugation and GS-Bi export rates are 7mins and 1hr, respectively. The glutathione synthesis rate of the 500μM experiment is the same as that of the 50μM experiment whereas the bromobimane conjugation rate was approximately twice as fast (3mins). However, the toxic effects of the 500μM dose resulted in cell death as is shown by the ^{31}P spectra, where the ATP is no longer visible, therefore the GS-Bi export rate could not be determined. The ATP/ADP concentration in ^{31}P NMR spectra is a major pharmacodynamic measure in toxicology, because it allows for the direct observation of cell bioenergetics over the course of the drug dose experiment. For the first time, the metabolism

of a xenobiotic, bromobimane is determined with 1 minute temporal resolution, sufficient to determine the toxicokinetics of diffusion of the xenobiotic doses, and glutathione-bimane conjugation and excretion in real-time. The study shows previously uncaptured, non-steady-state kinetics of the glutathione feedback mechanism that rapidly repletes the glutathione pool. Within the same study, pharmacokinetic parameters of adenosine charge, intracellular pH indicative and sugar phosphates indicative of glycolysis, and phospholipids intermediates indicative of membrane synthesis are obtained as toxicodynamic parameters quantifying metabolic effects of the xenobiotics. This biotechnology will permit rapid discovery of toxicology in a realistic model of liver toxicology.

4 Effect of Oxygen in a NMR-compatible Fluidized-bed Bioartificial Liver

4.1 Introduction

NMR studies of cell preparations permit the monitoring of cell composition, and contributions from immune, endocrine, paracrine, and physico-chemical parameters not afforded in intact or perfused organ systems [for reviews (34-39)]. Since 1973, four categories of NMR-compatible mammalian cell perfusion systems have evolved (9): (1) suspension (40), (2) entrapment (41-43), (3) microcarrier (37,45), and (4) membrane (46). The most widely applied method is the entrapment technique whereby cells are immobilized in threads of agarose (61) or alginate (41,43). Initially, NMR-compatible bioreactors for hepatocytes, or bioartificial liver (BAL), used hepatocyte suspensions, but function and viability only persisted for several hours before hypoxia caused cell death (5,40,49,50). This simple BAL evolved to perfusion systems where hepatocytes were encapsulated in collagen threads (51-57), alginate spherical encapsulates (58-60), or inoculated into membrane bioreactors (7). All early BAL studies used non-physiological concentrations of oxygen, typically 95:5 oxygen:carbon dioxide (carbogen) (47) in order to overcome hypoxia, whereby in vivo, the blood has hemoglobin, acting as an oxygen buffer, to reduce the oxygen gradient across the liver.

Although NMR-compatible BALs have been used for three decades (47,48), the lack of long-term cell viability and simplicity of bioreactor operation has hindered its widespread application. In this work, a simple fluidized-bed NMR-compatible bioreactor is described containing sodium alginate encapsulated hepatocytes with a uniform spherical radii of 250

μm, the limit of oxygen diffusion in BALs (113), which is a function of its diffusion coefficient and consumption rate. In previous studies, diffusion distances were on the order of 500-1000 μm (51-60)and entrapped cells were in a stationary packed-bed, which is subject to channeling causing heterogeneous perfusion and oxygenation (47). Channeling is eliminated in the fluidized-bed bioreactor where encapsulates are in constant free fall similar to the NMR-compatible spheroid bioreactor (73). Percolating the encapsulates and minimizing the diffusion distance insures homogenous perfusion achieving robust nutrient mass transfer.

In this study, an existing life support system, and bioreactor (107) were modified by inoculating with alginate-encapsulated hepatocytes. Four oxygen treatments were tested for maintaining viability: (1) carbogen, (2) 75:20:5 nitrogen:oxygen:carbon dioxide, (3) 60:35:5 nitrogen:oxygen:carbon dioxide and (4) 2 hr carbogen followed by 25 hr of 75:20:5 nitrogen:oxygen:carbon dioxide. *In vivo* ^{31}P NMR spectroscopy non-invasively monitored ß-NTP levels, a direct measure of viability (39), which were also validated by histology. Lastly, *in silico* modeling predicted the profile of oxygen concentration across the encapsulate, and oxygen concentrations were empirically determined for each treatment using oxygen electrodes placed inside the bioreactor. The goal of the present study is to maintain hepatocyte viability for at least 24 hr, which is longer than the 8 hr that is currently the longest published time of survival (114). In addition, hepatocytes are exquisitely tuned to oxygen tension, induced to produce erythropoietin in low oxygen, and overproducing reactive oxygen species in the mitochondria at higher oxygen tensions. Therefore, *in vivo* ^{13}C NMR labeled nutrient included in the media was used to characterize metabolism once the optimum oxygen tension was determined.

4.2 Methods

NMR supplies were obtained from multiple vendors. Sodium alginate, calcium chloride, perchloric acid, sodium citrate, sodium chloride, potassium chloride, magnesium sulfate, 4-(2-hydroxyethyl)-1-piperazineethanesulfonic acid (HEPES), bovine serum albumin, and 3-(trimethylsily)propionic-2,2,3,3-d_4 acid (TSP) were purchased from Sigma Chemical company (St. Louis, MO). Mono and dibasic phosphate, and barium chloride were purchased from Mallinckrodt (Paris, KY). Dulbeco's modified Eagle's medium (DMEM), insulin, penicillin, streptomycin, and fetal bovine serum were purchased from Invitrogen Corp. (Carlsbad, CA). Gibco Inc., a subsidiary of Invitrogen Corp., also made custom DMEM media for the ^{13}C NMR studies, without glucose, glutamine, glycine, and phenol red, which also has no alanine in the standard formulation (formulation No. 07-5058EB; Cat. No. 12100-046). For the Clark electrode, saturated potassium chloride solution was purchased from Mettler Toledo AG (Schwerzenbach Switzerland), and silver and platinum wire were purchased from Goodfellow Corp. (Oakdale, PA). The 2+1 channel PC digital oscilloscope (DS1M12 "Stingray") with accompanying software was purchased from USB Instruments (Hillsboro, OR). Deuterium oxide was from Cambridge Isotope Laboratories (Andover, MA). The 5 and 10 mm NMR tubes were purchased from Wilmad Labglass Inc. (Miamisburg, OH), while Norprene™ and Silastic™ tubing, tube connector, peristaltic pump, were from Cole Parmer (Vernon Hills, Il). The water bath and 500 mL Gibco™ reservoir culture bottles were from Fisher (Pittsburgh, PA). Bioreactor end pieces were manufactured from Delrin™ and assembled as previously described (110). Materials for the bioreactor life support units were previously described in earlier work (44).

4.2.1 Bioreactor Design and Life Support System

Alginate-encapsulated hepatocytes were perfused in a 10-mm screw-cap NMR tube (**Fig. 1**). A DelrinTM fixture provided aseptically-sealed input and output ports. The encapsulated cells were retained in the BAL by a fabricated finned baffle with 300 μm holes. FEP Teflon® tubing (0.8 mm I.D. x 1.6 mm O.D.; Cole Parmer, Vernon Hills, IL) was used to transport medium to the bottom of the NMR tube. A second FEP Teflon® line (1.6 mm I.D. x 3.2 mm O.D) was used to remove the medium above the end piece. To maintain the temperature at 37º C, both the input and output lines were water-jacketed with Norprene® tubing (9.525 mm I.D. x 15.875 mm O.D.; Cole Parmer, Vernon Hills, IL).

Perfusion media oxygenation was provided with a previously described (44) gas exchange module (GEM). Clark electrodes for dissolved oxygen measurements were fabricated from DelrinTM using platinum and silver wire contained in a solution of saturated potassium chloride position behind a semi-permeable membrane. Two electrodes were located in the inlet and outlet lines and interfaced to a laptop computer through a 2+1 channel PC digital oscilloscope, DS1M12 "Stingray" analog to digital converter. The recorded oxygen measurements were utilized to calculate the oxygen concentration in the various oxygen treatments. Culture medium was re-circulated at 3 mL/min through the encapsulated cells with a peristaltic pump (Masterflex, Cole Parmer, Vernon Hills, IL).

4.2.2 Hepatocyte Isolation Procedure

All animals were humanely housed and treated in accordance with guidelines set by the Institutional Animal Use and Care Committee of the University of North Carolina.

Sprague Dawley rats (Charles Rivers, Frederick, Md) were housed with a 12 hr dark cycle and allowed water and food ad libitum. The rats were anesthetized with Nembutal (0.5 μg/g body weight), and the hepatocytes were isolated following a two-step collagenase perfusion of the liver (115). After isolation, the hepatocytes were incubated at 37° C in Krebs-Ringer-HEPES (KRH) (116 mM NaCl, 5mM KCl, 1mM $KH2PO_4$, 2.5 mM $MgSO_4$, 2.5 mM $CaCl_2$, 25 mM HEPES, 1% BSA, pH 7.4) for 10 min. While at 37° C, the cells were gently mixed every 2 min. Next, the hepatocytes were settled for 15 min on ice and the top layer was removed. Lastly, the cells were washed in KRH and pelleted at 50 x g three times. After the final spin the hepatocytes were resuspended in KRH and cell number and viability was assessed by trypan blue exclusion.

4.2.3 Encapsulation Methods

Cells were encapsulated using an electrostatic bead generation apparatus described previously (111) with modifications (110). Briefly, rat hepatocytes at density of 7 x 10^7 cells/mL were suspended in 2% sodium alginate solution at a 1:1 ratio. The resulting 1% alginate solution containing 3.5 x107 cells/mL was put in a 1cc syringe fitted with a 24 gauge angiocatheter. The angiocatheter was pierced at the hub with a 27 gauge needle which served as the positive electrode for the electrostatic casting process. The syringe was placed in a syringe pump (Braintree Scientific BS-8000, Braintree, MA) and arranged such that as droplets were ejected from the angiocatheter they would fall orthogonally into the 150mM $CaCl_2$ or $BaCl_2$ saline solution bath (6.7 mM KCl, 142 mM NaCl, HEPES 10 mM at pH 7.4) at 4°C. Use of barium rather than calcium in cross-linking the carboxylate groups of alginate, results in stronger and firmer encapsulates (116). This was tested to investigate if

encapsulates would maintain structure better over the 28hr period. Ultimately $CaCl_2$ was used. Encapsulates were transferred to culture media within two minutes to avoid excessive exposure to calcium or barium. The distance from the angiocatheter tip to the surface of the $CaCl_2$ or $BaCl_2$ solution was fixed at 2.5 cm. Pump flow rate were set within the range of 0.75 to 1.5mL/min. A grounded electrode was immersed in the $CaCl_2$ or $BaCl_2$ receiving bath. When the syringe pump was turned on, in the presence of the high electrostatic potential (ca 6 kV), the sodium alginate solution was pulled away from the angiocatheter tip as tiny droplets that polymerize into solid calcium alginate immediately upon contact with the $CaCl_2$ or $BaCl_2$ saline solution.

4.2.4 *In Vivo* ^{31}P and ^{13}C NMR Spectroscopy and BAL Operation

The 10 mm NMR tube and loop was autoclaved or sterilized with ethanol and laid out to dry in a laminar flow hood. The entire loop volume is 50 ml and about three volumes, or 150 ml, of DMEM were rinsed through the entire loop prior to inoculation of 1.5 ml of encapsulates. The cell density is 3.5×10^7 hepatocytes/ml of encapsulate and perfused at 3 ml/min. The waterbath for the GEM and water-jacketed lines, and the temperature of the air-heated NMR probed were set to 37° C, and the spinner and the 10 mm NMR tube containing encapsulates was inserted into a 10 mm fiberglass spinner and lowered into the magnet. A ^{1}H one-pulse was used to shim on water and line widths of typically 25 Hz were routinely achieved prior to start of *in vivo* ^{31}P NMR spectroscopy. The 13C media contained 25 mM 2-^{13}C-glucose, 4 mM U-^{13}C-glutamine, and 2 mM 2-^{13}C-glycine, and was switched with the ^{12}C media after 20 hrs of ^{31}P NMR monitoring, and *in vivo* ^{13}C NMR spectroscopy was

acquired for 3.5 hrs prior to ending the study and extracting the hepatocytes for high resolution NMR analysis.

In vivo ^{31}P NMR experiments of the primary rat hepatocytes were performed on a narrow-bore 14.1T Varian INOVA NMR spectrometer equipped with a 10mm broadband probe (Venus Probes, Livermore, CA). The receiver frequency of the probe was tuned to ^{31}P at 242.78 MHz. A one-pulse sequence with a sweep width of 10,000 Hz and 16K complex data points, using a calculated Ernst angle of 77° (22μs) and a 2 s repetition time. NMR data were processed off-line with ACD/Specmanager software (ACD/Labs, Toronto, Ontario, Canada). The signal-to-noise function in ACD software was used to calculate the signal-to-noise ratio of the ß-NTP peak in the various in vivo ^{31}P NMR spectra. ^{31}P metabolites were identified using α-NTP (-7.5 ppm) as an internal reference. Spectra were peak-fitted using the Gauss-Lorentz apodization and plotted as ratios of their absolute peak area at each time point relative to total ^{31}P peak area or relative other individual peak area in the ^{31}P spectrum for each given time point. The chemical shift of inorganic phosphate (Pi) relative to α-NTP was used to calculate intracellular pH (117).

For the optimal oxygen concentration, *in vivo* ^{13}C NMR studies were performed for 3.5 hrs, after 18 hrs of *in vivo* 31P NMR monitoring of viability, in order to characterize metabolism. The 10 mm broadband NMR probe was tuned to 150 MHz, the ^{13}C frequency, and a 90 degree flip angle with WALTZ ^{1}H decoupling during acquisition with a 50% duty cycle. That is, acquisition time was 1s and interpluse delay was 1s, resulting in a 2s repletion time.

4.2.5 High Resolution ^{1}H NMR Spectroscopy

^{1}H NMR of the metabolomic footprint was performed as previously described (72) using a 14.1 T INOVA NMR spectrometer equipped with a 5 mm inverse detection probe (Nalorac Corp., Martinez, CA). The samples were prepared with 540 µl of media and 60 µl of deuterium oxide containing a final concentration of 1.43 mM TSP. A one-pulse sequence with a 1.5 s presaturation pulse was used with a sweep width of 8192 Hz and 32K complex data points, resulting in an acquisition time of 4 s. This sequence used a 90º flip-angle with an 11 s inter-pulse delay, and therefore a total repetition time of 15 seconds with 32 transients. The FIDs were processed with a 0.5 Hz exponential, zero-filled to 64K datapoints, and Fourier transformed into the frequency domain. Absolute sample concentrations were determined using Chenomx NMR processing software (Alberta, Canada) using TSP as the concentration reference. Consumption and production rates were calculated as the millimolar difference between the beginning and end of the experimental time resulting in units of mM/hr/106 cells.

4.2.6 Histology *In Vivo* ^{31}P NMR Spectroscopy

Encapsulated hepatocytes were fixed for 24 h at 4 ºC in 1.5% paraformaldehyde in phosphate buffer (30 mM NaH2PO4, 45 mM Na2HPO4). After fixation, the encapsulated hepatocytes were washed twice with PBS (137 mM NaCl, 2.7 mM KCl, 8.10 mM Na2HPO4, 2 mM KH2PO4 , 0.49 mM MgSO4 and a pH of 7.4) followed by three washes with 70% ethanol, 95% ethanol, and 100% ethanol. Lastly, the encapsulated hepatocytes were washed for 45 min with toluene. After transferring the encapsulated hepatocytes to small open-ended metal containers in a warming box, paraffin wax was added to the metal container, and

allowed to sit for 15 min at 55 ºC. The melted wax was aspirated and fresh paraffin was put into the metal container. After 15 min, the encapsulates were put into a plastic mold which was refilled with paraffin wax. After cooling to room temperature, the wax block was removed from the mold and cut into 9 µm sections and put onto charged slides.

The slides were regressively stained by hemotoxylin and eosin. Briefly, the slides were washed twice for 10 min in toluene, twice for 3 min in 100% ethanol, twice for 3 min in 95% ethanol, and once in 70% ethanol for 3 min. After rinsing the slides for 3 min in water, they were put for 3 min into Gil's 1x Hemotoxylin and rinsed twice in an acid-alcohol solution (10 mM HCl in 70% ethanol). The slides were rinsed for 5 min in water, and soaked for 1 minute in ammonium hydroxide (35 mM). After a brief rinse in water, the slides were stained for 1 min with picro eosin (1.6 g Eosin Y in 144 80% ethanol with 16 mL of saturated 1.22% picric acid) for 1 min. Lastly, slides were dipped twice in 70% ethanol, twice in 95% ethanol, once in 100% ethanol, and soaked for 6 min in xylenes. A cover slip was added with permount glue.

4.2.7 Oxygen Electrode Construction and Measurement

An improved Clark micro-electrode (118,119) was constructed using materials described above. Continuous recording of oxygen tensions was conducted by polarography (118,119), which is effective especially for oxygen measurement in slow-flowing liquids. The size of Pt-Ag sensor was reduced to 1 mm in diameter, and the chamber was filled with saturated KCI electrolyte and covered with a latex membrane, instead of Teflon. Examined liquid flowed through a tiny gap (~0.5 mm); the sensor’s latex membrane was integrated in one wall of this gap. The flow rate (3 mL/min) was fast enough to equilibrate diffusion of

oxygen through the membrane into the electrolyte. To eliminate failures, we used two consecutive sensors and averaged outputs. Oxygen micro-electrode calibration was performed before each experiment using 95% and 20% oxygen mixes and nitrogen as the calibrate for 0% oxygen. The same procedure was repeated after each experiment and the averaged data was used as the calibration. Several experiments were conducted, without cells, to determine the actual oxygen concentration of the input media. This was achieved by placing the oxygen micro-electrode in-line at the end of the input media line to measure oxygen concentrations where the media is first delivered to the beads. Temperature was controlled at 37°C and the oxygen micro-electrodes were insulated to prevent a drop in temperature. Results of these measurements indicated that the media contained 20%, 35%, and 95% oxygen concentration upon delivery to the beads for the respective experiments.

4.2.8 Modeling of Oxygen Gradients in the Encapsulates

To make a steady state approximation of the oxygen diffusion, the one-dimensional heat equation was fit by Dr. Kayvan Keshari (University of California at San Francisco) using Matlab 7.5 (Mathworks) using the equation below (113):

$$\frac{\partial C}{\partial t} = D_{normal}\left(\frac{\partial^2 C}{\partial x^2}\right) - q \qquad \textbf{Eq. 4}$$

Where Dnormal is the diffusion coefficient and assumed to be 0.6 x 10-9 m2/s (47) and q is the cellular utilization rate assumed to be 0.4 nmols/s/106 cells (87), assuming for liver, 1 cm3 is equivalent to 2.5 x 108 liver cells (47). Although consumption rates in 2D hepatocyte cultures have ranged from 0.2 to 0.7 nmols/s/106 cells, 0.4 nmols/s/106 (87) has been used in previous in silico studies to derive oxygen profiles (47) in 3D bioreactors (113). Cell volume was obtained knowing the number of cells per encapsulate volume in the bioreactor. These

were plotted versus time and diffusion distance for each of the three conditions (20%, 35%, and 95% oxygen).

4.3 Results

Encapsulates are suspended in the bioreactor (**Figure 1-6**) and perfused with oxygenated cell culture media. In this suspension, encapsulates are perfused at a rate that causes them to percolate to avoid stagnation and then future channeling. Encapsulates are kept in a fixed volume and a closed system, so the fluidization results from the density difference between the encapsulates and the fluid. The downward pressure from the closed system and gravity is counter to the upward velocity of the laminar fluid flow causing a convective motion of encapsulates.

Figure 4-1 depicts stack plots of the in vivo ^{31}P NMR spectral time courses of encapsulated rat hepatocytes perfused with 20%, 35%, 55%, and 95% oxygen from t=0 (bottom) to t=28hr or until the β-NTP resonance was undetectable. The signal-to-noise ratios (SNR) of β-NTP from the first spectrum of the series are 4.9, 5.9, 7.2, and 6.9 for 20%, 35%, 55%, and 95%, respectively. With 20 % oxygen (**Figure 4-1A**), the hepatocytes never recovered from the hypoxic shock of isolation and β-NTP was not visible at 10 hr as shown in the graph of β-NTP in figure . Interestingly, the intracellular Pi peak decreased over time (**Figure 4-1A**) and a plot of intracellular Pi versus extracellular Pi (**Figure 4-3A**) paralleled the β-NTP time course (**Figure 4-2A**) suggesting that this is also a measure of cell viability. The beginning of the β-NTP time course shows a period of increased signal intensity indicative of recovery to hypoxic shock as a result of the isolation procedure. In addition, anaerobic glycolysis likely increased due to lack of

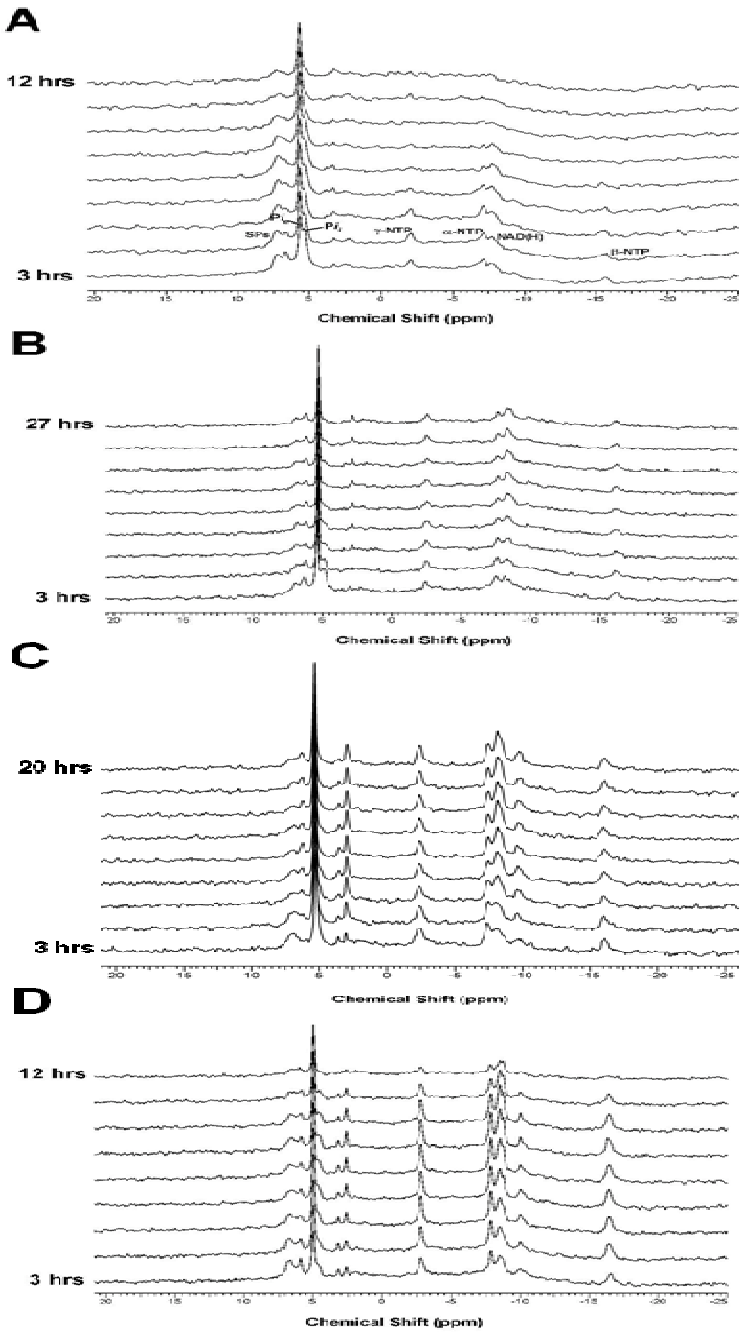

Figure 4-1 Stack plot of in vivo ^{31}P NMR spectra time course of encapsulated rat hepatocytes perfused with 20% from 0 to12 hr (**A**), 35% from 0 to 27hr (**B**), 55% from 0 to 20 hr (**C**) and 95% oxygen from 0 to t=12hr (**D**).

oxygen as supported by the relatively low intracellular pH of ca 7.0 (**Figure 4-4A**) resulting from lactic acid accumulation. The decrease of intracellular Pi over time (**Figure 4-3A**) indicates cell death without recovery from the hypoxic insult during the isolation process (**Figure 4-2A**). The relatively high sugar phosphate peak area can also be a measure of anaerobic glycolysis since sugar phosphates are used in glycolysis (120), and was highest in the 20% treatment (**Figure 4-1A**).

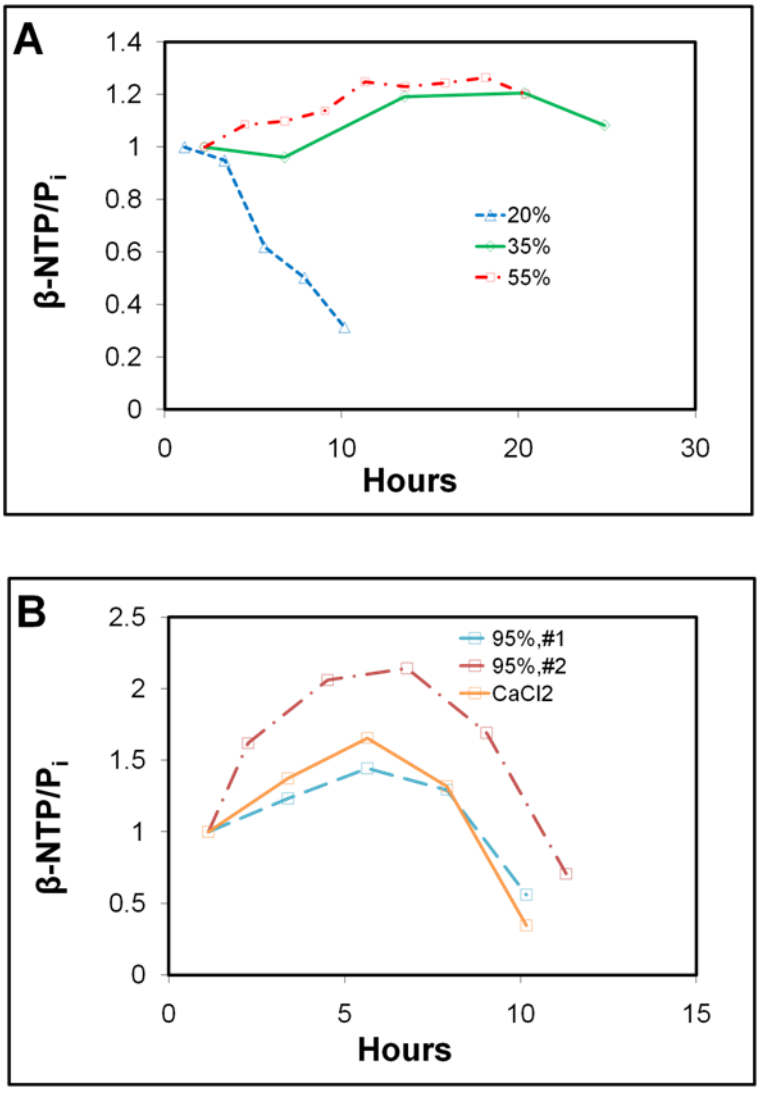

Figure 4-2 Graphs of β-NTP/Pi from hepatocytes perfused with media subjected to 20%, 35%, and 55% oxygen (A), and 95% oxygen (B) treatments. Note that "95%, #1" and "95%, #2" are hepatocytes that were encapsulated using barium rather than calcium.

With 95% oxygen (**Figure 4-1D**), the hepatocytes gave a robust β-NTP signal, and the spectral SNR was superior to the other treatments. The beginning of the β-NTP time course shows that the cells had already recovered from the hypoxic isolation process, and in fact, β-NTP was still increasing (**Figure 4-1D**). The cells were perfused with a media volume of 500 mL, and there were minimal nutrient concentration variations over the course of the experiment as verified by 1H NMR analysis of the media samples. However, the cells abruptly died by 11 hrs as shown in **figure 4-2B** indicated by a dramatic drop in β-NTP levels starting at the 7 hr time point. Overall, there was no difference in the ^{31}P NMR time courses between BaCl2 and CaCl2. To avoid possible toxicity that would not be detected by ^{31}P NMR, CaCl2 was used with the other oxygen treatments, although it has been suggested that the chelated barium in alginate encapsulates is not available to the cells due to its relatively high affinity for the carboxylates in alginate (116). In addition, unlike the 20% oxygen treatment where the intracellular Pi peak was always present, one appeared at 5 hrs (**Figure 4-1D**) and the intracellular Pi versus extracellular Pi peak area ratio tracked the β-NTP time course after 5 hrs, indicating cell death as in the 20% treatment (**Figure 4-2B**). The intracellular pH was initially similar to that of the media, pH 7.4, but shifted to pH 7.1 at 5 hrs (**Figure 4-4B**), and paralleled the trend of intracellular Pi versus extracellular Pi peak area ratio (**Figure 4-3B**). Interestingly, there was a relatively large sugar phosphate peak area initially during recovery from isolation, which decreased until 7 hrs when it reversed and increased until the end of the experiment (**Figure 4-1D**). This same pattern was also seen in the two studies of barium encapsulates. This indicates that glycolysis initially was high due to the hypoxic isolation process as indicated by the high sugar phosphate peak area (**Figure 4-1D**), but rapidly recovered its normal pH by the first spectrum, and maintained normal pH

(7.4) for 5 hrs when it shifted to pH 7.1 (**Figure 4-4B**). The glucose, pyruvate, and glutamine consumption rates and lactate and alanine production rates (72) in the calcium encapsulates were 46.7, 13.1, and 24.0, and 28.4 and 5.9 pM/s/106 cells, respectively, demonstrating that only 37% of glucose formed the anaerobic glycolytic end-products, lactate and alanine. This data suggests that aerobic metabolism was prominent during the first 7 hrs and minimal lactate and alanine was formed. Then, hepatocytes switched to anaerobic glycolysis, and ultimately by 11 hrs, even glycolysis was not sufficient to maintain viability. The SNR of β-NTP in the ^{31}P NMR spectra (**Figure 4-1D**) was higher than the 35% treatment (**Figure 4-1B**) suggesting a higher energy charge per unit cell in the first 7 hr of perfusion with 95% oxygen perhaps due to a higher mitochondrial metabolic rate resulting in higher levels of β-NTP.

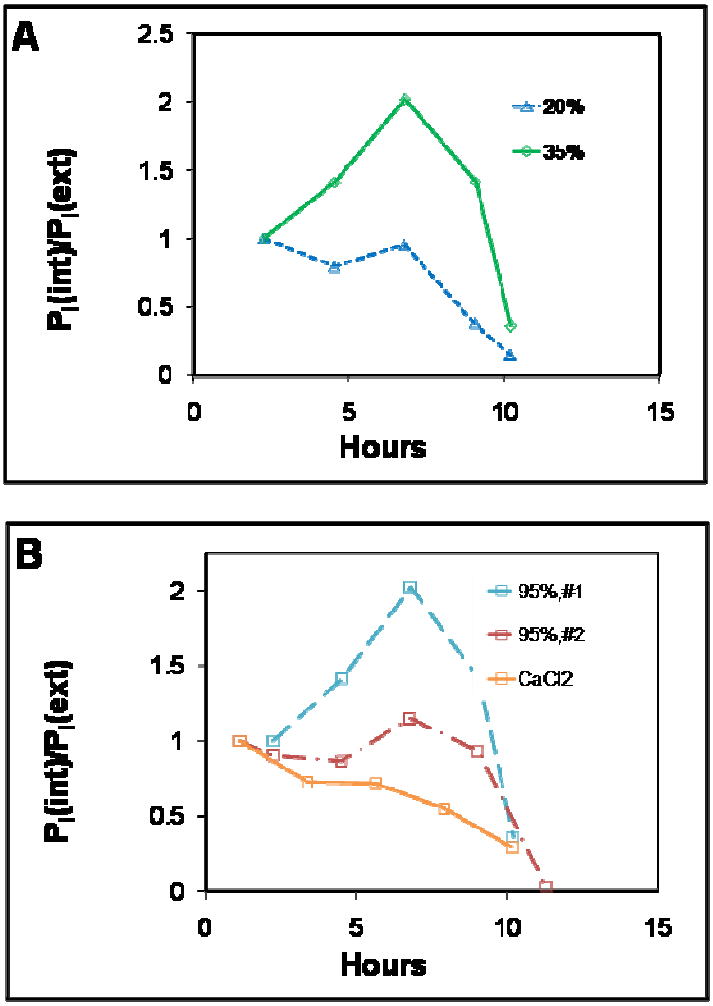

Figure 4-3 Graph of Pi(int)/Pi(ext) from hepatocytes perfused with media subjected to 20% and 35% oxygen (A), and 95% oxygen (B) treatments. Note that "95%, #1" and "95%, #2" are hepatocytes that were encapsulated using barium rather than calcium.

The second best oxygen treatment for maintaining viability was 35%. The β-NTP signal-to-noise ratio (SNR= 5.9) was similar to that of the 95% oxygen treatment (SNR=6.9), by comparing the first few spectra from **Figure 4-1B** and **Figure 4-1D**. The β-NTP time course proved that 35% oxygen treatment achieved our goal of maintaining hepatocyte viability for 24 hrs and the trend was linear and could have gone longer.

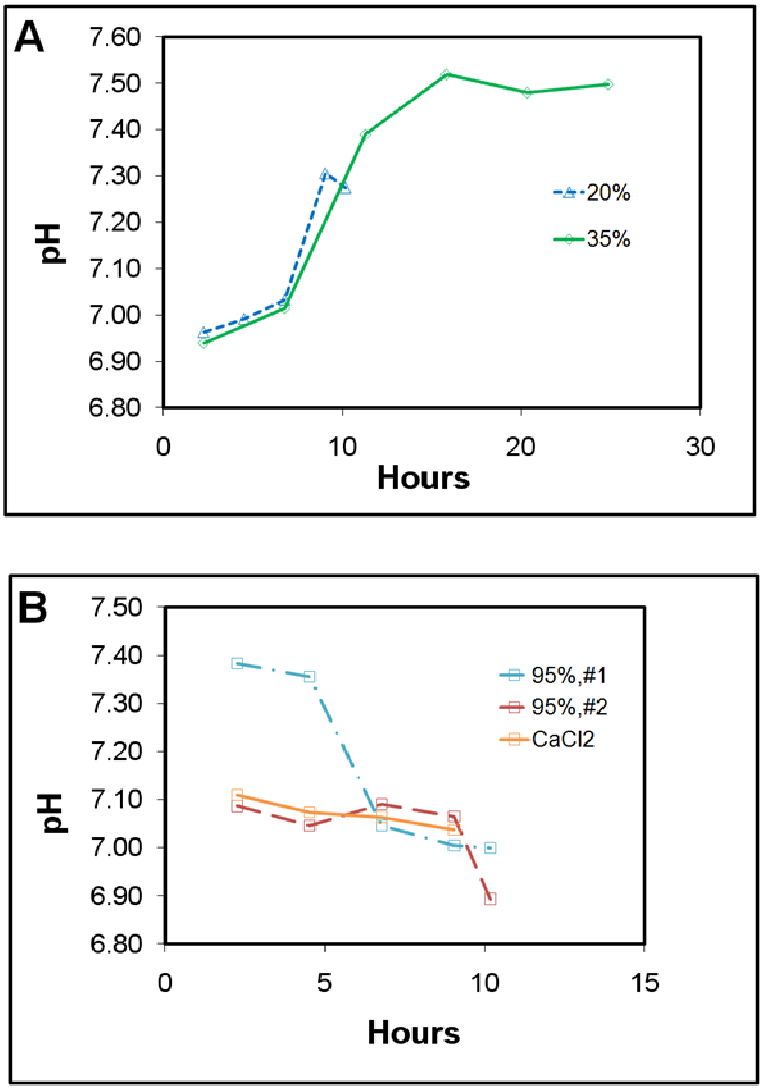

Figure 4-4 Graph of intracellular pH of hepatocytes perfused with media subjected to 20% and 35% oxygen (A), and 95% oxygen (B) treatments. Note that "95%, #1" and "95%, #2" are hepatocytes that were encapsulated using barium rather than calcium.

The intracellular Pi to extracellular Pi peak area ratio decreased, and eventually becomes indistinguishable from the extracellular peak suggesting a full recovery from the isolation procedure by 12 hrs (**Figure 4-3A**). The intracellular pH of the 35% treatment was initially similar to that of the 20% treatment (pH 7.0) becoming normal (pH 7.4) by 8 hrs (**Figure 4-4A**). In addition, there is a relatively high sugar phosphate peak that decreases over time paralleling the decrease in intracellular pH (**Figure 4-1B**). These data indicate an initial

reliance on glycolysis, which dissipates by 8 hrs. The glucose, pyruvate, and glutamine consumption rates and lactate and alanine production rates (72) were 24.6, 15.5, and 4.7, and 48.0 and 4.6 pM/s/106 cells respectively. This is a lower glucose consumption rate compared to 95% oxygen (46.7 pM/s/106 cells), suggesting that 95% oxygen treatment results in a higher metabolic rate with more oxygen availability. Both values of glucose consumption are within the normal range for hepatocyte cultures (Macdonald et al., 1999). In the 95% oxygen treatment, lactate and alanine production was about half that of the 35% oxygen treatment. However, 37% and 100% of the glucose consumed in hepatocytes from the 95% and 35% oxygen treatments, respectively, resulted in anaerobic glycolytic end-products. This suggests that the majority of 35% oxygen treated encapsulates were hypoxic even though the intracellular pH returned to normal, 7.4, by 11hrs (**Figure 4-4A**).

Figure 4-5 is a representative 15 minute *in vivo* 13C NMR spectrum after 30 min of perfusion in **A**. This is the second spectrum of the time series shown in **B**. The large signal from media are shown in **figure 4-5B**, but one can observe the increase of two peak, 2-^{13}C-lactate (~69ppm) and [2-^{13}C-glycyl]glutathione peaks, resulting from 2-^{13}C-glucose and 2-13C-glycine, respectively. **Figure 4-5C** shows how the lactate production rate is obtained from the time series. The peak is referenced to the 25 mM glucose peaks (α and β) and the slope is then multipled by two since two moles of lactate (one labeled that we observed, and another unlabeled that we do not observe) are produced from one mole of 2-^{13}C-glucose, but the ^{13}C NMR only detects the ^{13}C labeled lactate, not the mole of ^{12}C-labeled lacate.

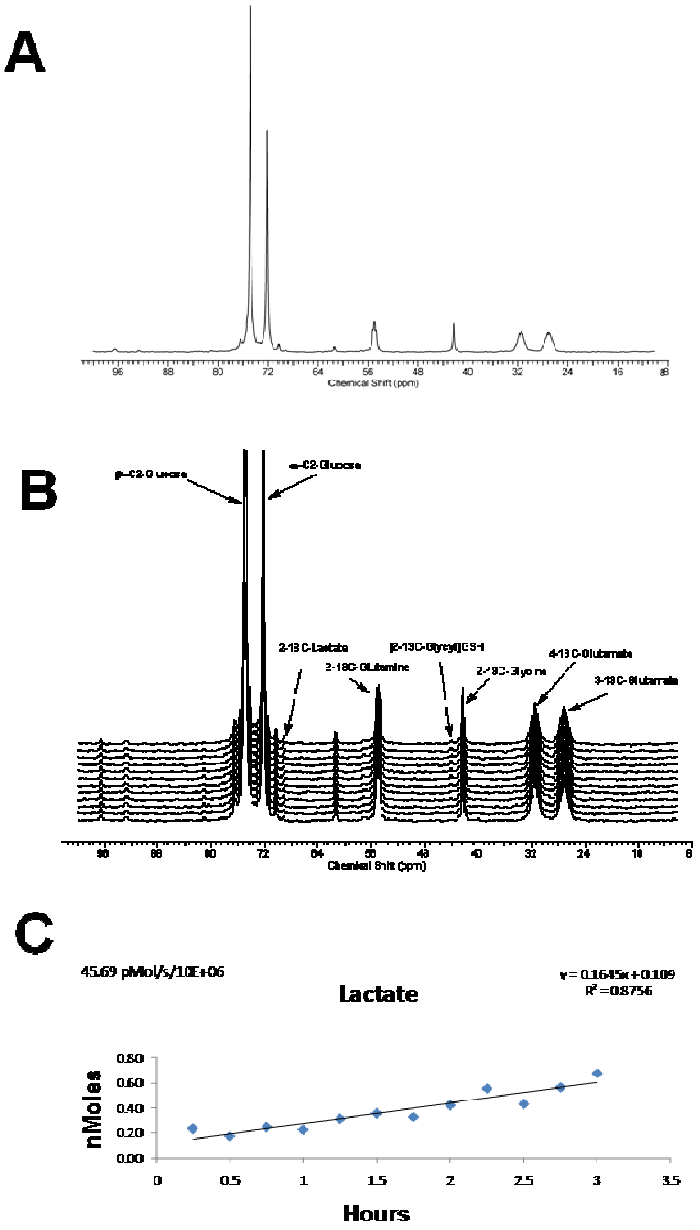

Figure 4-5 Representative ^{13}C NMR spectrum of rat hepatocytes perfused with DMEM containing 25 mM 2-^{13}C-Glucose, 4 mM U-^{13}C-Glutamine, and 2 mM 2-^{13}C-Glycine at time = 30 min (**A**), and the respective time series uptake showing primarily 2-^{13}C-lactate (~69ppm) and [2-13C-glycyl]glutathione peaks increasing ober the 3.5 hrs (**B**). The lactate production rate is derived from fitted peak area (**C**).

Figure 4-6 shows the histological sections of a representative encapsulate perfused with media at 35% (A) and 95% (B) oxygen concentration demonstrating the difference in

appearance and viability of the cells. One can observe cellular debris and some blebs in the encapsulates treated with 95% oxygen (**Figure 4-6B**). Higher magnification of the hepatocytes in **Figure 4-6A** treated with 35% oxygen revealed nicely stained nuclei with some dividing, punctate mitochondria, and bleb-free cell membranes on nearly all the

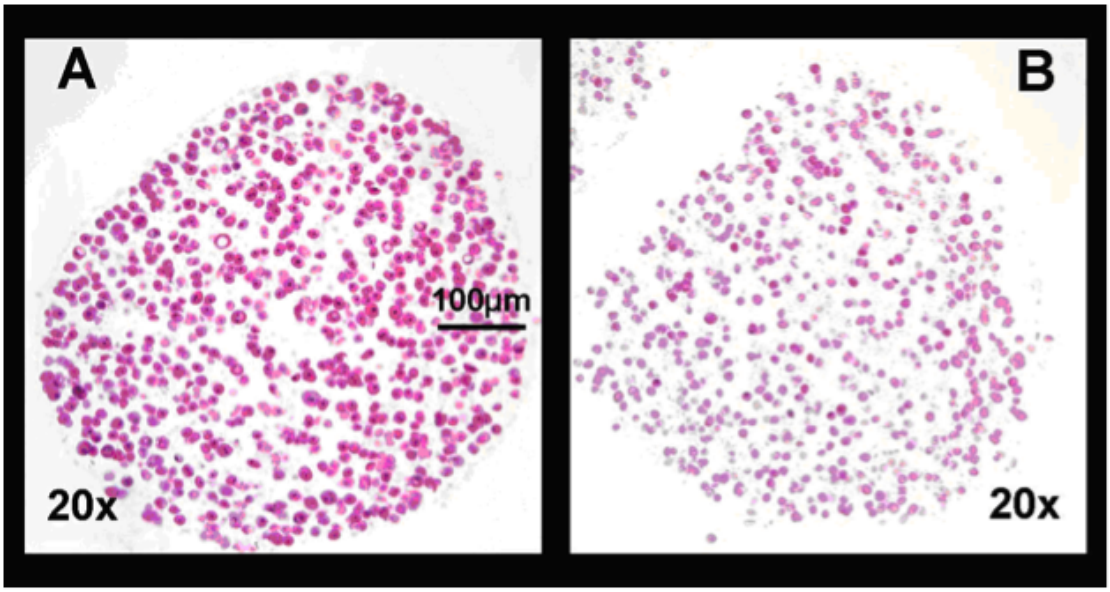

Figure 4-6 The histology of the encapsulates with 35% (A) and 95% (B) oxygen treatments demonstrating the appearance of the cells, and the distribution of viable cells. Note the abundance of cell debris in the 95% treatment.

hepatocytes. Hepatocytes were similar in appearance to other viable hepatocytes in histological images of collagen-encapsulated hepatocytes in long-term culture inside a bioartificial liver (99,121,122). Also, both encapsulates are spherical and approximately 500 µm diameter.

Figure 4-7 shows the difference in the in silico oxygen concentration out to a radius of 1 mm for 20%, 35%, and 95% oxygen. Rather than presenting standard dimensionless

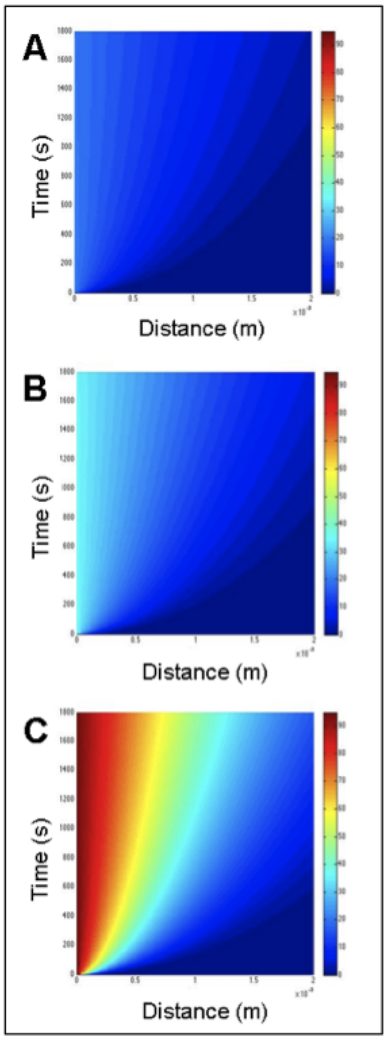

Figure 4-7 The in silico oxygen concentrations for 20% (**A**), 35% (**B**), and 95% (**C**) across the encapsulates showing the radius in mm along the x axis and time along the y-axis.

parameters, such as the Theile moduli (47), to illustrate the oxygen mass transfer in encapsulates of different diffusion distances, this presentation of oxygen concentration profiles versus time relates two points important for the study: (1) the time to oxygen

equilibration in the encapsulate, and (2) the oxygen concentration for a given diffusion distance. The y-axis is time and the x-axis is distance with 10% oxygen having a concentration of 0.1 mM. Immediately one observes a major difference in the time required to reach a steady oxygen concentration. For example, for 0.5 mm and 1 mm distance in the 95% oxygen treatment (**Figure 4-7C**) requires 200 s (3.7min), and 1000 s (16.7 min), respectively, for a stable 35% oxygen concentration to be reached. However, the primary point of these graphs is to compare the three different oxygen concentrations at 0.25 mm, the diffusion distance of encapsulates used in this study. For example, at 200 s, the oxygen concentration for 20%, 35%, and 95% at 0.25mm is 7%, 15%, 60%, respectively. For this study the radius was 0.25 mm, and one can see that the estimation of oxygen concentration gradient for the 95% oxygen treatment results in a toxic level of oxygen throughout the bead or hyperoxic, whereas the 20% oxygen treatment may become hypoxic in the center of the encapsulate. This in silico model of oxygen concentration across encapsulates supports the empirical data, which demonstrate 95% oxygen causes hyperoxic and toxic oxygen concentrations resulting in hepatocyte death. The model shows it takes about two minutes for the oxygen levels to reach a fairly steady plateau throughout the encapsulate.

4.4 Discussion

Although NMR-compatible BAL technology was first introduced three decades ago, there is still no report of a long-term device, longer than 8 hr (58-60), for primary hepatocytes. The primary reason for this is insufficient oxygenation of the hepatocytes. Hepatocytes require relatively high amounts of oxygen. The oxygen buffering capacity of hemoglobin, which increases oxygen concentration nearly two orders-of-magnitude,

maintains an oxygen gradient across the acinus of 8% to 3% where blood exits the liver (47). To date, there is no publication on a NMR-compatible BAL describing the viability and longevity of cells with systematic increments of oxygen concentration in the perfusate. All studies report durations of 8 hr or less after inoculation in the BAL.

According to our data, these cells likely would have died at ca 10 hr after inoculation in the bioreactor due to hyperoxemia (**Figure 4-2**). Our data suggests that during the first 5 hr of perfusion with 95% oxygen the hepatocytes recover from the hypoxic isolation process (**Figure 4-2B** and **Figure 4-3B**) and the ^{31}P NMR spectra (**Figure 4-1D**) are similar to ^{31}P NMR spectra from intact liver (7). However, by 8 hrs the ß-NTP decreases (**Figure 4-2B**), while the intracellular pH decreases (**Figure 4-4B**) and sugar phosphates increases (**Figure 4-1D**) indicating an increase in anaerobic glycolysis. This increase in anaerobic glycolysis is likely due to oxidative damage to mitochondria affecting aerobic metabolism, and the hepatocyte then turns to cytosolic production of ATP. This is supported by the appearance of an intracellular Pi peak at pH 7.0 at 5 hrs (**Figure 4-3B**) that increased relative to Pi from media. Our in silico model (**Figure 4-7C**) and others (87,123) predict hyperoxemia throughout the encapsulate with 95% oxygen. Also supportive of the initial aerobic metabolism is the finding that only 37% of the glucose consumed formed the anaerobic glycolytic end-products, lactate and alanine

One interesting finding was that there was no clear evidence that barium encapsulation is toxic to the hepatocytes as supported by the fact that there was no difference between the ß-NTP (**Figure 4-2B**) or pH (**Figure 4-4B**) time courses of barium or calcium encapsulates, and both treatments survive the perfusion for the same period of time. Calcium was used for the other oxygen treatments since previous alginate encapsulated bioartificial livers systems

more commonly used calcium (59,71), and potential barium toxicities could be avoided. Although calcium is an extremely potent intracellular secondary messenger, both calcium and barium have such high affinities for the carboxylate groups that they are relatively unavailable, or the encapsulate would lose integrity and disintegrate.

Many extracorporeal bioartificial liver systems use 95% oxygen, and hepatocytes are purported to have survived for weeks (20,47,124). This is likely due to the larger diffusion distances of these bioreactors and the ability for the hepatocytes that survive the initial hyperoxic stress and move within the bioreactors to a region of optimal oxygen concentration, as it is well known that hepatocytes can move via philopodia (125). For example, rat hepatocytes grown in a multicoaxial bioreactor (63), were shown to migrate and form organoid structures at an optimal distance from the oxygen sources after several days of culture (121). Although the NMR-compatible coaxial bioreactor design maintains a homogeneous diffusion distance and has been shown to maintain hepatocyte viability for weeks (121), the amount of biomass is much less than the encapsulation and suspension bioreactors and therefore, the temporal NMR spectral resolution will never match that of the fluidized-bed bioreactor (7) and therefore, generates inferior kinetic data (Table 1).

The suspension bioreactor suffers the worse mass transfer being packed in a 5 mm NMR tube with a diffusion distance of ca 30 mm from the cell mass surface to the bottom of the NMR tube (5,40,49,50). However, the suspension BAL has the most biomass resulting in the best signal-to-noise ratio and excellent spectral resolution and lineshape (**Table 1**). In addition, these have utilized air, or 20% oxygen. From our results, 20% oxygen did not permit full recovery of the ß-NTP. In addition, reports of bioartificial liver surviving with 20% oxygen require diffusion distances less than 200 µm (99,121,122). There has never been

a NMR-compatible bioreactor published that utilizes liver cells with microcarriers. This is most likely due to aggregation of cells caused by cell-to-cell surface binding through calcium-dependent adhesion molecules causing channels to form between aggregates and resulting in large diffusion distance (unpublished results). In fact, liver spheroid cultures depend on this aggregation effect to be formed (63), and to avoid this, spheroids (44) and microcarrier (45) are typically immobilize in a packed-bed bioreactor. Similar to this study, the agarose thread encapsulation BAL (51-57) and a packed-bed bioreactor (58-60) gave a sufficient ^{31}P NMR signal with 15 min temporal and similar spectral resolution as shown in figure 2C. However, channels can form with gel threads and a packed-bed bioreactor (47)and in addition, the diffusion distance was about 0.5 mm (52) and 1 mm (59). The NMR-compatible BAL study, using a coaxial membrane bioreactor, compared two bioreactors with 0.2 and 0.5 mm diffusion distance and found that only the former bioreactor maintained viability (7). The maximum diffusion distance for a BAL was found to be about 0.2 mm (126). Therefore, due to the excessive diffusion distance, it may have been necessary to use 95% oxygen with these NMR-compatible gel thread and packed-bed bioreactors (**Table 1**), but then hyperoxemia causing oxygen toxicity ultimately limits long-term use.

The fluidized-bed BAL described herein has enough biomass to yield a sufficient signal-to-noise ratio in 30 min (**Figure 4-1B**), yet maintains the maximum diffusion distance of ca 0.2 mm resulting in the best characteristic of the various bioreactor types (**Table 1**). The oxygen studies showed that use of 35% or 55% oxygen was required to maintain viability for the duration of the study, 28 hrs (**Figure 4-1B** and **Figure 4-2B**), and likely beyond. The bioreactor is versatile and designs have been constructed to fit conventional 5 mm NMR probes, although a 10 mm NMR tube was used in this study. The life support

system (44) and oxygen electrode permit defined gas concentrations and in-line monitoring, similar to other systems (45).

Although the hepatocytes were maintained for 28 hours with little change in the ß-NTP peak area (**Figure 4-2B**), they exhibited a high degree of anaerobic glycolysis not typical in liver. For example, the intracellular pH (**Figure 4-4A**) and sugar phosphates (**Figure 4-1B**) were relatively similar to the 20% oxygen treatment rather than the 95% oxygen treatment. Also, 100% of the consumed glucose could be accounted for by the production rates of lactate and alanine. The *in silico* oxygen concentration model confirmed that the core of the encapsulates would be hypoxic with 35% oxygen (**Figure 4-7B**). The use of oxygen carriers incorporated into the alginate matrix would likely permit the use of a lower oxygen concentration closer to the 8% found in vivo (47), and eliminate the hypoxic core of the encapsulate. However, the hepatocytes were viable for 28hr, suggesting sufficient oxygenation. Higher concentrations of oxygen, such as 55%, was tested and would result in a higher level of oxygen toxicity than the 35% treatment, but still lactate was produced (**Fig. 4-5C**), indicating anaerobic glycolysis and hypoxia is still prevalent, or hepatocytes are acting more undifferentiated.

In short, this is the first comprehensive study of oxygen treatment with NMR-compatible BALs to determine conditions for long-term cultures. Soluble factors and oxygen carriers will likely help extend the viability and function of the hepatocytes, however, certainly the diffusion distance is optimum with the fluidized-bed bioreactor. This NMR-compatible BAL will be an ideal model to test soluble and insoluble factors for toxicology testing and regenerative medicine.

5 Conclusions

5.1 Future Studies

5.1.1 Problems and changes to existing hardware (APAP sticking)

Of particular interest during the acetaminophen experiments was that of the effect, or lack thereof, of the three doses. Normally a concentration of 25-50 mM is extremely toxic to rat hepatocytes and although JM1 cells have not previously been known to have significant cytochrome P450 activity, some degree of APAP metabolism was expected. However, there were no signs of hepatotoxicity or xenobiotic metabolism in any of the APAP treatments. Further investigation of the media revealed that the actual concentration of the 50 mM control dose was only 7.8 mM. This was mainly due to binding with albumin that is present in the fetal bovine serem that is added to the media. In addition, the concentration of APAP upon exiting the gas exchange module and was even less (0.5 mM). A possible reason for this significant reduction in concentration could be attributed to acetaminophen binding to the silastic tubing in the GEM, just as the silica tubing in HPLC columns has been known to react with xenobiotics causing them to bind. Future xeniobiotic studies will incorporate a drug injection port directly between the GEM and bioreactor loop. This will enable the bypass of the silastic tubing inside the GEM and ensure the full desired concentration of xenobiotic to be administered to the cells within the bioreactor.

5.1.2 Pulse sequence and elimination of media signal (Software)

Another factor introduced by perfusion of media in the fluidized-bed bioreactor is motion, both that of the media and that of the percolating beads. NMR samples are usually comprised of urine, serum, proteins and other stationary mediums. These are prepared with a known concentration of a standard such as TSP and then sealed within an NMR tube. The NMR tube is then inserted into the probe and spun to ensure a homogenous magnetic field is obtained. This is not the case with NMR-compatible bioreactors because the sample cannot be spun and media is also being constantly perfused within the NMR tube. This constant motion causes problems during the acquisition of the signal coming from the bioreactor, such as reduced resolution and loss of signal. One of the ways to address this issue is to utilize custom pulse sequences to provide a gradient that will suppress the effect of the motion. Moment nulling gradient waveforms can accomplish refocussing of spins moving with constant velocity, acceleration, and/or higher orders of motion. Futher investigation into modified pulse sequences and their effect on the motion experienced in the NMR-compatible fluidized-bed BAL will be conducted to improve the resulting NMR spectra.

5.1.3 Calibration of in vivo data (Extracts)

As mentioned previously, a known concentration of a standard is usually utilized to determine the actual concentration of the metabolites of interest in an NMR sample. The NMR-compatible fluidized-bed BAL does not utilize a standard therefore the determination of metabolite concentrations is not straightforward. A means of obtaining the concentrations is provided by analyzing the cell extracts from the experiment however this is a destructive process therefore this cannot be conducted until the experiment has been terminated. Cell

extracts were obtained from the experiments conducted in this research project and will therefore be processed to back calculate the actual in vivo concentrations of the various metabolites of interest. This data will be provided in a future publication of this research.

5.1.4 Data analysis and metabolic model

One of the main benefits of a fluidized-bed bioreactor is that it attains maximum mass transfer of nutrients compared to the other types of NMR-compatible bioreactor. Questions regarding mass transfer in encapsulations in this form of bioreactor should be further explored through modeling. The toxicokinetic experiments of Chapter 3 demonstrate the power of the fluidized-bed BAL in that this is the first time 1-min temporal resolution has ever been attained with real-time, in-vivo NMR. This resolution enabled the capture of the dynamic feedback mechanism of glutathione regulation and the increased flux rate of its resynthesis after a toxic reduction with bromobimane. Mathemathetical modeling of one-carbon metabolism of glutathione has been conducted by Reed et al. (127) consisting of the transsulfuration pathway, and glutathione synthesis, transport, and breakdown. The model is based on known properties of the enzymes and the regulation of those enzymes by oxidative stress. They explored the half-life of glutathione, the regulation of glutathione synthesis, and its sensitivity to fluctuations in amino acid input. As is usually the case with most mathematical models, numerous assumptions had to be made due to the lack of experimental data to validate the model. However, this is no longer the case as the experimental data from the bromobimane experiment can now be utilized to validate the model and in turn, the model can provide ‘what-if’ scenarios that truly reflect the biological mechanisms of glutathione regulation. A future collaboration with Dr. Reed and Dr. Nijhout will also enable

additional experiments to be designed and simulated to predict outcome with significantly increased accuracy prior to conducting the study.

6 References

1. Rothman DL. 1H NMR studies of human brain metabolism and physiology. In: Gillies RJ, editor. NMR in Physiology and Biomedicine. San Diego: Academic Press; 1994.

2. Degani H, Ronen SM, Furman-Haran E. Breast cancer: spectroscopy and imaging of cells and tumors. NMR in Physiology and Biomedicine. San Diego: Academic Press; 1994.

3. Gillies RJ, Barry JA, Ross BD. In vitro and in vivo 13C and 31P NMR analyses of phosphocholine metabolism in rat glioma cells. Magn Reson Med 1994;32(3):310-318.

4. Ronen SM, Volk A, Mispelter J. Comparative NMR study of a differentiated rat hepatoma and its dedifferentiated subclone cultured as spheroids and as implanted tumors. NMR Biomed 1994;7(6):278-286.

5. Nicholson JK, Timbrell JA, Bales JR, Sadler PJ. A high resolution proton nuclear magnetic resonance approach to the study of hepatocyte and drug metabolism. Application to acetaminophen. Mol Pharmacol 1985;27(6):634-643.

6. Sanders JKM, Hunter BK. Modern NMR Spectroscopy: A Guide for Chemists. USA: Oxford University Press; 1993.

7. Macdonald JM, Grillo M, Schmidlin O, Tajiri DT, James TL. NMR spectroscopy and MRI investigation of a potential bioartificial liver. NMR Biomed 1998;11(2):55-66.

8. Quistorff B. Metabolic heterogeneity of liver parenchymal cells. Essays Biochem 1990;25:83-136.

9. Moon RB, Richards JH. Determination of intracellular pH by 31P magnetic resonance. J Biol Chem 1973;248(20):7276-7278.

10. Gorenstein DG. Phosphorous-31 NMR: Principles and Applications. Gorenstein DG, editor. New York: Academic Press; 1984.

11. Devlin TM. Textbook of biochemistry : with clinical correlations: Wiley-Liss; 2006.

12. Pico C, Puigserver P, Oliver P, Palou A. 2-Methoxyestradiol, an endogenous metabolite of 17beta-estradiol, inhibits adipocyte proliferation. Mol Cell Biochem 1998;189(1-2):1-7.

13. Fiehn O. Combining genomics, metabolome analysis, and biochemical modelling to understand metabolic networks. Comp Funct Genomics 2001;2(3):155-168.

14. Boros LG, Brackett DJ, Harrigan GG. Metabolic biomarker and kinase drug target discovery in cancer using stable isotope-based dynamic metabolic profiling (SIDMAP). Curr Cancer Drug Targets 2003;3(6):445-453.

15. Goodacre R, Vaidyanathan S, Dunn WB, Harrigan GG, Kell DB. Metabolomics by numbers: acquiring and understanding global metabolite data. Trends Biotechnol 2004;22(5):245-252.

16. Yang C, Hua Q, Shimizu K. Metabolic flux analysis in Synechocystis using isotope distribution from 13C-labeled glucose. Metab Eng 2002;4(3):202-216.

17. Raamsdonk LM, Teusink B, Broadhurst D, Zhang N, Hayes A, Walsh MC, Berden JA, Brindle KM, Kell DB, Rowland JJ, Westerhoff HV, van Dam K, Oliver SG. A functional genomics strategy that uses metabolome data to reveal the phenotype of silent mutations. Nat Biotechnol 2001;19(1):45-50.

18. Underwood BR, Broadhurst D, Dunn WB, Ellis DI, Michell AW, Vacher C, Mosedale DE, Kell DB, Barker RA, Grainger DJ, Rubinsztein DC. Huntington disease patients and transgenic mice have similar pro-catabolic serum metabolite profiles. Brain 2006;129(Pt 4):877-886.

19. Brown KM, von Weymarn LB, Murphy SE. Identification of N-(hydroxymethyl) norcotinine as a major product of cytochrome P450 2A6, but not cytochrome P450 2A13-catalyzed cotinine metabolism. Chem Res Toxicol 2005;18(12):1792-1798.

20. Allen JW, Bhatia SN. Formation of steady-state oxygen gradients in vitro: application to liver zonation. Biotechnol Bioeng 2003;82(3):253-262.

21. Kaderbhai NN, Broadhurst DI, Ellis DI, Goodacre R, Kell DB. Functional genomics via metabolic footprinting: monitoring metabolite secretion by Escherichia coli tryptophan metabolism mutants using FT-IR and direct injection electrospray mass spectrometry. Comp Funct Genomics 2003;4(4):376-391.

22. Howard MD, Mirajkar N, Karanth S, Pope CN. Comparative effects of oral chlorpyrifos exposure on cholinesterase activity and muscarinic receptor binding in neonatal and adult rat heart. Toxicology 2007;238(2-3):157-165.

23. Henriques ID, Aga DS, Mendes P, O'Connor SK, Love NG. Metabolic footprinting: a new approach to identify physiological changes in complex microbial communities upon exposure to toxic chemicals. Environ Sci Technol 2007;41(11):3945-3951.

24. Lazebnik Y. Can a biologist fix a radio? -- Or, what I learned while studying apoptosis, (Cancer Cell. 2002 Sep;2(3):179-82). Biochemistry (Mosc) 2004;69(12):1403-1406.

25. Devantier R, Scheithauer B, Villas-Boas SG, Pedersen S, Olsson L. Metabolite profiling for analysis of yeast stress response during very high gravity ethanol fermentations. Biotechnol Bioeng 2005;90(6):703-714.

26. Ideker T, Galitski T, Hood L. A new approach to decoding life: systems biology. Annu Rev Genomics Hum Genet 2001;2:343-372.

27. Kitano H. Computational systems biology. Nature 2002;420(6912):206-210.

28. Mendes P, Kell D. Non-linear optimization of biochemical pathways: applications to metabolic engineering and parameter estimation. Bioinformatics 1998;14(10):869-883.

29. Mendes P, Kell DB. On the analysis of the inverse problem of metabolic pathways using artificial neural networks. Biosystems 1996;38(1):15-28.

30. Robertson DG, Reily MD, Sigler RE, Wells DF, Paterson DA, Braden TK. Metabonomics: evaluation of nuclear magnetic resonance (NMR) and pattern recognition technology for rapid in vivo screening of liver and kidney toxicants. Toxicol Sci 2000;57(2):326-337.

31. Gavaghan CL, Wilson ID, Nicholson JK. Physiological variation in metabolic phenotyping and functional genomic studies: use of orthogonal signal correction and PLS-DA. FEBS Lett 2002;530(1-3):191-196.

32. Warne MA, Boyd EM, Meharg AA, Osborn D, Killham K, Lindon JC, Nicholson JK. Quantitative structure-toxicity relationships for chlorophenols to bioluminescent lux-marked bacteria using atom-based semi-empirical molecular-orbital descriptors. SAR QSAR Environ Res 1999;10(5):473-495.

33. Bundy JG, Papp B, Harmston R, Browne RA, Clayson EM, Burton N, Reece RJ, Oliver SG, Brindle KM. Evaluation of predicted network modules in yeast metabolism using NMR-based metabolite profiling. Genome Res 2007;17(4):510-519.

34. Dale BE, Gillies RJ. Nuclear magnetic resonance spectroscopy of dense cell populations for metabolic studies and bioreactor engineering: a synergistic partnership. Biotechnology 1991;17:107-118.

35. Ruiz-Cabello J, Cohen JS. NMR and the study of pathological state in cells and tissues. Int Rev Cytol 1993;145:1-63.

36. Kaplan O, Cohen JS. Metabolism of breast cancer cells as revealed by non-invasive magnetic resonance spectroscopy studies. Breast Cancer Res Treat 1994;31(2-3):285-299.

37. Szwergold BS. NMR spectroscopy of cells. Annu Rev Physiol 1992;54:775-798.

38. Zupke C, Foy B. Nuclear magnetic resonance analysis of cell metabolism. Curr Opin Biotechnol 1995;6(2):192-197.

39. Mancuso A, Glickson JD. Applications of NMR spectroscopy and imaging to the study of immobilised cell physiology. V. N, R. W, editors: Kluwer Academic Publishers; 2004. 439-467 p.

40. Cohen SM, Ogawa S, Rottenberg H, Glynn P, Yamane T, Brown TR, Shulman RG. P nuclear magnetic resonance studies of isolated rat liver cells. Nature 1978;273(5663):554-556.

41. Narayan KS, Moress EA, Chatham JC, Barker PB. 31P NMR of mammalian cells encapsulated in alginate gels utilizing a new phosphate-free perfusion medium. NMR Biomed 1990;3(1):23-26.

42. Macdonald JM, Kurhanewicz J, Dahiya R, Espanol MT, Chang LH, Goldberg B, James TL, Narayan P. Effect of glucose and confluency on phosphorus metabolites of perfused human prostatic adenocarcinoma cells as determined by 31P MRS. Magn Reson Med 1993;29(2):244-248.

43. Constantinidis I, Mukundan NE, Gamcsik MP, Sambanis A. Towards the development of a bioartificial pancreas: a 13C NMR study on the effects of alginate/poly-L-lysine/alginate entrapment on glucose metabolism by beta TC3 mouse insulinoma cells. Cell Mol Biol (Noisy-le-grand) 1997;43(5):721-729.

44. Gamcsik MP, Millis KK, Colvin OM. Noninvasive detection of elevated glutathione levels in MCF-7 cells resistant to 4-hydroperoxycyclophosphamide. Cancer Res 1995;55(10):2012-2016.

45. Mancuso A, Beardsley NJ, Wehrli S, Pickup S, Matschinsky FM, Glickson JD. Real-time detection of 13C NMR labeling kinetics in perfused EMT6 mouse mammary tumor cells and betaHC9 mouse insulinomas. Biotechnol Bioeng 2004;87(7):835-848.

46. Gillies RJ, Galons JP, McGovern KA, Scherer PG, Lien YH, Job C, Ratcliff R, Chapa F, Cerdan S, Dale BE. Design and application of NMR-compatible bioreactor circuits for extended perfusion of high-density mammalian cell cultures. NMR Biomed 1993;6(1):95-104.

47. Macdonald JM, Griffin J, Kubota H, Griffith L, Fair J, Reid LM. Bioartificial Livers. In: Kuhtreiber W, Lanza RP, Chick WL, editors. Cell Encapsulation Technology and Therapeutics. Cambridge, MA: Birkhauser Boston; 1999. p 252-286.

48. Macdonald JM, Xu ASL, Kubota H, LeCluyse E, Hamilton G, Liu H, Rong YW, Moss N, Lodestro C, Luntz T, Wolfe SP, Reid LM. Epithelial Cell Culture: Liver. In: Lanza WL, Langer R, Vacanti J, editors. Methods of Tissue Engineering. San Diego: Academic Press 2001. p 151-201.

49. Cohen SM, Ogawa S, Shulman RG, Ardenkjaer-Larsen JH. 13C NMR studies of gluconeogenesis in rat liver cells: utilization of labeled glycerol by cells from euthyroid and hyperthyroid rats. Proc Natl Acad Sci U S A 1979;76(4):1603-1609.

50. Moxon LN, Field J, Irving MG, Doddrell DM. In vitro metabolism of [2-13C]-ethanol by 1H NMR spectroscopy using 13C decoupling with the reverse dept polarization-transfer pulse sequence. Biochem Biophys Res Commun 1985;128(1):107-112.

51. Gasbarrini A, Borle AB, Caraceni P, Colantoni A, Farghali H, Trevisani F, Bernardi M, Van Thiel DH. Effect of ethanol on adenosine triphosphate, cytosolic free calcium, and cell injury in rat hepatocytes. Time course and effect of nutritional status. Dig Dis Sci 1996;41(11):2204-2212.

52. Gasbarrini A, Borle AB, Farghali H, Bender C, Francavilla A, Van Thiel D. Effect of anoxia on intracellular ATP, Na+i, Ca2+i, Mg2+i, and cytotoxicity in rat hepatocytes. J Biol Chem 1992;267(10):6654-6663.

53. Gasbarrini A, Borle AB, Farghali H, Caraceni P, Van Thiel D. Fasting enhances the effects of anoxia on ATP, Cai2+ and cell injury in isolated rat hepatocytes. Biochim Biophys Acta 1993;1178(1):9-19.

54. Gasbarrini A, Borle AB, Farghali H, Francavilla A, Van Thiel D. Fructose protects rat hepatocytes from anoxic injury. Effect on intracellular ATP, Ca2+i, Mg2+i, Na+i, and pHi. J Biol Chem 1992;267(11):7545-7552.

55. Farghali H, Caraceni P, Rilo HL, Borle AB, Gasbarrini A, Gavaler J, Van Thiel DH. Biochemical and 31P-NMR spectroscopic evaluation of immobilized perfused rat Sertoli cells. J Lab Clin Med 1996;128(4):408-416.

56. Farghali H, Sakr M, Gasbarrini A, Williams DS, Dowd SR, Ho C, Van Thiel DH. A biochemical and 31P-NMR investigation of the effect of FK 506 and cyclosporine pretreatment on immobilized hepatocytes perifused with ethanol. Transplant Proc 1991;23(6):2805-2808.

57. Farghali H, Williams DS, Caraceni P, Borle AB, Gasbarrini A, Gavaler J, Rilo HL, Ho C, Van Thiel DH. Effect of ethanol on energy status and intracellular calcium of Sertoli cells: a study using immobilized perfused cells. Endocrinology 1993;133(6):2749-2755.

58. Miccheli A, Tomassini A, Capuani G, Di Cocco ME, Sartori E, Falasca L, Conti Devirgiliis L, Manetti C, Conti F. Energy metabolism and re-establishment of intercellularadhesion complexes of gel entrapped hepatocytes. Cytotechnology 2000;32(3):219-228.

59. Falasca L, Miccheli A, Sartori E, Tomassini A, Conti Devirgiliis L. Hepatocytes entrapped in alginate gel beads and cultured in bioreactor: rapid repolarization and reconstitution of adhesion areas. Cells Tissues Organs 2001;168(3):126-136.

60. Murtas S, Capuani G, Dentini M, Manetti C, Masci G, Massimi M, Miccheli A, Crescenzi V. Alginate beads as immobilization matrix for hepatocytes perfused in a

bioreactor: a physico-chemical characterization. J Biomater Sci Polym Ed 2005;16(7):829-846.

61. Foxall DL, Cohen JS, Mitchell JB. Continuous perfusion of mammalian cells embedded in agarose gel threads. Exp Cell Res 1984;154(2):521-529.

62. Keshari KR, Kurhanewicz J, Jeffries RE, Wilson DM, Dewar BJ, Van Criekinge M, Zierhut M, Vigneron DB, Macdonald JM. Hyperpolarized (13)C spectroscopy and an NMR-compatible bioreactor system for the investigation of real-time cellular metabolism. Magn Reson Med 2010;63(2):322-329.

63. Wolfe SP, Hsu E, Reid LM, Macdonald JM. A novel multi-coaxial hollow fiber bioreactor for adherent cell types. Part 1: hydrodynamic studies. Biotechnol Bioeng 2002;77(1):83-90.

64. Kelce WR, Monosson E, Gamcsik MP, Laws SC, Gray LE, Jr. Environmental hormone disruptors: evidence that vinclozolin developmental toxicity is mediated by antiandrogenic metabolites. Toxicol Appl Pharmacol 1994;126(2):276-285.

65. Barry JA, McGovern KA, Lien YH, Ashmore B, Gillies RJ. Dimethyl methylphosphonate (DMMP): a 31P nuclear magnetic resonance spectroscopic probe of intracellular volume in mammalian cell cultures. Biochemistry 1993;32(17):4665-4670.

66. Gueven N, Becherel OJ, Howe O, Chen P, Haince JF, Ouellet ME, Poirier GG, Waterhouse N, Fusser M, Epe B, de Murcia JM, de Murcia G, McGowan CH, Parton R, Mothersill C, Grattan-Smith P, Lavin MF. A novel form of ataxia oculomotor apraxia characterized by oxidative stress and apoptosis resistance. Cell Death Differ 2007;14(6):1149-1161.

67. Judd RM, Rottman GA, Forder JR, Yin FC, Blackband SJ. Feasibility of 19F imaging of perfluorochemical emulsions to measure myocardial vascular volume. Magn Reson Med 1992;28(1):129-136.

68. Goecke-Flora CM, Reo NV. Influence of carbon chain length on the hepatic effects of perfluorinated fatty acids. A 19F- and 31P-NMR investigation. Chem Res Toxicol 1996;9(4):689-695.

69. Macdonald JM, LeBlanc DA, Haas AL, London RE. An NMR analysis of the reaction of ubiquitin with [acetyl-1-13C]aspirin. Biochem Pharmacol 1999;57(11):1233-1244.

70. Simpson NE, Grant SC, Blackband SJ, Constantinidis I. NMR properties of alginate microbeads. Biomaterials 2003;24(27):4941-4948.

71. Joly A, Desjardins JF, Fremond B, Desille M, Campion JP, Malledant Y, Lebreton Y, Semana G, Edwards-Levy F, Levy MC, Clement B. Survival, proliferation, and

functions of porcine hepatocytes encapsulated in coated alginate beads: a step toward a reliable bioartificial liver. Transplantation 1997;63(6):795-803.

72. Seagle C, Christie MA, Winnike JH, McClelland RE, Ludlow JW, O'Connell TM, Gamcsik MP, Macdonald JM. High-throughput nuclear magnetic resonance metabolomic footprinting for tissue engineering. Tissue Eng Part C Methods 2008;14(2):107-118.

73. Freyer JP, Fink NH, Schor PL, Coulter JR, Neeman M, Sillerud LO. A system for viably maintaining a stirred suspension of multicellular spheroids during NMR spectroscopy. NMR Biomed 1990;3(5):195-205.

74. Van Zijl PC, Moonen CT, Faustino P, Pekar J, Kaplan O, Cohen JS. Complete separation of intracellular and extracellular information in NMR spectra of perfused cells by diffusion-weighted spectroscopy. Proc Natl Acad Sci U S A 1991;88(8):3228-3232.

75. O'Leary DJ, Hawkes SP, Wade CG. Indirect monitoring of carbon-13 metabolism with NMR: analysis of perfusate with a closed-loop flow system. Magn Reson Med 1987;5(6):572-577.

76. Ugurbil K, Guernsey DL, Brown TR, Glynn P, Tobkes N, Edelman IS. 31P NMR studies of intact anchorage-dependent mouse embryo fibroblasts. Proc Natl Acad Sci U S A 1981;78(8):4843-4847.

77. Catapano G, Euler M, Gaylor JDS, Gerlach J. Characterization of the distribution of matter in hybrid liver support devices where cells are cultured in a 3-D membrane network or on flat substrata. Int J Artif Organs 2001;24(2):102-109.

78. Aiken J, Cima L, Schloo B, Mooney D, Johnson L, Langer R, Vacanti JP. Studies in rat liver perfusion for optimal harvest of hepatocytes. J Pediatr Surg 1990;25(1):140-144; discussion 144-145.

79. Gonzalez-Mendez R, Wemmer D, Hahn G, Wade-Jardetzky N, Jardetzky O. Continuous-flow NMR culture system for mammalian cells. Biochim Biophys Acta 1982;720(3):274-280.

80. Hrovat M, Wade C, Hawkes S. A space-efficient assembly for NMR experiments on anchorage-dependent cells. J Magn Reson 1985;61:409-417.

81. McClelland GB, Brooks GA. Changes in MCT 1, MCT 4, and LDH expression are tissue specific in rats after long-term hypobaric hypoxia. J Appl Physiol 2002;92(4):1573-1584.

82. Macdonald JM, Schmidlin O, James TL. In vivo monitoring of hepatic glutathione in anesthetized rats by 13C NMR. Magn Reson Med 2002;48(3):430-439.

83. Custer L. Physiological Studies of Hybridoma Cultivation in Hollow Fiber Bioreactors. Berkeley: University of California; 1988.

84. Leblond FA, Simard G, Henley N, Rocheleau B, Huet PM, Halle JP. Studies on smaller (approximately 315 microM) microcapsules: IV. Feasibility and safety of intrahepatic implantations of small alginate poly-L-lysine microcapsules. Cell Transplant 1999;8(3):327-337.

85. Seagle CM, University of North Carolina at Chapel Hill. Dept. of Biomedical Engineering. Development of an electrostatic device for the encapsulation of cells in gel matrix and a novel NMR method for comparative analysis of media streams from bioreactors [Thesis (M S)]: University of North Carolina at Chapel Hill, 2005.; 2005. xv, 73 leaves p.

86. Glacken MW, Fleischaker RJ, Sinskey AJ. Large-scale production of mammalian cells and their products: engineering principles and barriers to scale-up. Ann N Y Acad Sci 1983;413:355-372.

87. Rotem A, Toner M, Tompkins RG, Yarmush ML. Oxygen uptake rates in cultured rat hepatocytes. Biotechnol Bioeng 1992;40(10):1286-1291.

88. Trivedi N, Keegan M, Steil GM, Hollister-Lock J, Hasenkamp WM, Colton CK, Bonner-Weir S, Weir GC. Islets in alginate macrobeads reverse diabetes despite minimal acute insulin secretory responses. Transplantation 2001;71(2):203-211.

89. Uludag H, De Vos P, Tresco PA. Technology of mammalian cell encapsulation. Adv Drug Deliv Rev 2000;42(1-2):29-64.

90. Martin Y, Vermette P. Bioreactors for tissue mass culture: design, characterization, and recent advances. Biomaterials 2005;26(35):7481-7503.

91. Riley MR, Muzzio FJ, Reyes SC. Effect of oxygen limitations on monoclonal antibody production by immobilized hybridoma cells. Biotechnol Prog 1997;13(3):301-310.

92. Wolfle D, Jungermann K. Long-term effects of physiological oxygen concentrations on glycolysis and gluconeogenesis in hepatocyte cultures. Eur J Biochem 1985;151(2):299-303.

93. Wolfle D, Schmidt H, Jungermann K. Short-term modulation of glycogen metabolism, glycolysis and gluconeogenesis by physiological oxygen concentrations in hepatocyte cultures. Eur J Biochem 1983;135(3):405-412.

94. Nishikawa M, Uchino J, Matsushita M, Takahashi M, Taguchi K, Koike M, Kamachi H, Kon H. Optimal oxygen tension conditions for functioning cultured hepatocytes in vitro. Artif Organs 1996;20(2):169-177.

95. Ohno K, Maier P. Cultured rat hepatocytes adapt their cellular glycolytic activity and adenylate energy status to tissue oxygen tension: influences of extracellular matrix components, insulin and glucagon. J Cell Physiol 1994;160(2):358-366.

96. Fenge C, Klein C, Heuer C, Siegel U, Fraune E. Agitation, aeration and perfusion modules for cell culture bioreactors. Cytotechnology 1993;11(3):233-244.

97. Emery AN, Jan DC, al-Rubeai M. Oxygenation of intensive cell-culture system. Appl Microbiol Biotechnol 1995;43(6):1028-1033.

98. Mehmetoglu U, Ates S, Berber R. Oxygen diffusivity in calcium alginate gel beads containing Gluconobacter suboxydans. Artif Cells Blood Substit Immobil Biotechnol 1996;24(2):91-106.

99. De Bartolo L, Jarosch-Von Schweder G, Haverich A, Bader A. A novel full-scale flat membrane bioreactor utilizing porcine hepatocytes: cell viability and tissue-specific functions. Biotechnol Prog 2000;16(1):102-108.

100. Roy P, Baskaran H, Tilles AW, Yarmush ML, Toner M. Analysis of oxygen transport to hepatocytes in a flat-plate microchannel bioreactor. Ann Biomed Eng 2001;29(11):947-955.

101. Mancuso A, Fernandez EJ, Blanch HW, Clark DS. A nuclear magnetic resonance technique for determining hybridoma cell concentration in hollow fiber bioreactors. Biotechnology (N Y) 1990;8(12):1282-1285.

102. James MO, Yan Z, Cornett R, Jayanti VM, Henderson GN, Davydova N, Katovich MJ, Pollock B, Stacpoole PW. Pharmacokinetics and metabolism of [14C]dichloroacetate in male Sprague-Dawley rats. Identification of glycine conjugates, including hippurate, as urinary metabolites of dichloroacetate. Drug Metab Dispos 1998;26(11):1134-1143.

103. Garbow JR, Ridley WP, Bork V, Pan Y, Schaefer J. Milacemide metabolism in rat liver and brain slices by solids NMR. Drug Metab Dispos 1994;22(2):298-303.

104. Nihlen A, Sumner SC, Lof A, Johanson G. 13C(2)-Labeled methyl tert-butyl ether: toxicokinetics and characterization of urinary metabolites in humans. Chem Res Toxicol 1999;12(9):822-830.

105. Muller HJ, Lanens D, de Cock Buning TJ, van de Vyver FL, Alderweireldt FC, Dommisse R, Spanoghe M, Mulder GJ, Lugtenburg J. Noninvasive in vivo 13C-NMR spectroscopy in the rat to study the pharmacokinetics of 13C-labeled xenobiotics. Drug Metab Dispos 1992;20(4):507-509.

106. Tew KD. Glutathione-associated enzymes in anticancer drug resistance. Cancer Res 1994;54(16):4313-4320.

107. Gamcsik MP, Bierbryer RG, Millis KK. Noninvasive monitoring of glutathione turnover in perfused MCF-7 cells. Free Radic Biol Med 2004;37(7):961-968.

108. Zhang J, Huang W, Chua SS, Wei P, Moore DD. Modulation of acetaminophen-induced hepatotoxicity by the xenobiotic receptor CAR. Science 2002;298(5592):422-424.

109. Rumack BH. Acetaminophen misconceptions. Hepatology 2004;40(1):10-15.

110. Jeffries R, Keshari, K., Seagle, C., Pediaditakis, P., Gamcsik, M., Kurhanewicz, J.,, Macdonald J. A Vesatile NMR-compatible Bioreactor for Alginate-Encapsulated Liver Cells.; 2008; Toronto, Ontario, Canada.

111. Chandrasekaran P, Seagle C, Rice L, Macdonald J, Gerber DA. Functional analysis of encapsulated hepatic progenitor cells. Tissue Eng Chandrasekaran, P 2006;12(7):2001-2008.

112. Kriat M, Confort-Gouny S, Vion-Dury J, Sciaky M, Viout P, Cozzone PJ. Quantitation of metabolites in human blood serum by proton magnetic resonance spectroscopy. A comparative study of the use of formate and TSP as concentration standards. NMR Biomed 1992;5(4):179-184.

113. McClelland RE, MacDonald JM, Coger RN. Modeling O2 transport within engineered hepatic devices. Biotechnol Bioeng 2003;82(1):12-27.

114. Capuani G, Miccheli A, Tomassini A, Falasca L, Aureli T, Conti F. Cellular volume determination of alginate-entrapped hepatocytes by MRI diffusion measurements. Artif Cells Blood Substit Immobil Biotechnol 2000;28(4):293-305.

115. Jirtle RL, Michalopoulos G, McLain JR, Crowley J. Cancer Res 1981;41:3512–3518.

116. Dulieu C, Poncelet D, Neufeld R. Encapsulation and Immobilization Techniques. In: Kuhtreiber W, Lanza R, Chick W, editors. Cell Encapsulation Technology and Therapeutics, Tissue Engineering. Boston: Birkhauser; 1999. p 3-17.

117. Seo Y, Murakami M, Watari H, Imai Y, Yoshizaki K, Nishikawa H, Morimoto T. Intracellular pH determination by a 31P-NMR technique. The second dissociation constant of phosphoric acid in a biological system. J Biochem 1983;94(3):729-734.

118. Clark LC, Jr., Helmsworth JA, Kaplan S, Sherman RT, Taylor Z. Polarographic measurement of oxygen tension in whole blood and tissues during total by-pass of the heart. Surg Forum 1953;4:93-96.

119. Clark LC, Jr., Wolf R, Granger D, Taylor Z. Continuous recording of blood oxygen tensions by polarography. J Appl Physiol 1953;6(3):189-193.

120. Barany M, Glonek T. Identification of Diseased States by Phosphorus-31 NMR. In: Gorenstein DG, editor. Phosphorus-31 NMR: Principles and Applications: Academic Press; 1984. p 512-545.

121. McClelland RE, Coger RN. Effects of enhanced O(2) transport on hepatocytes packed within a bioartificial liver device. Tissue Eng 2004;10(1-2):253-266.

122. Kusumi T, Ishihara K, Mizumoto H, Nakazawa K, Ijima H, Funatsu K, Kajiwara T. Evaluation of a bioreactor with stacked sheet shaped organoids of primary hepatocytes. J Biosci Bioeng 2009;107(5):552-555.

123. Nahmias Y, Kramvis Y, Barbe L, Casali M, Berthiaume F, Yarmush ML. A novel formulation of oxygen-carrying matrix enhances liver-specific function of cultured hepatocytes. Faseb J 2006;20(14):2531-2533.

124. Catapano G, Patzer JF, 2nd, Gerlach JC. Transport Advances in Disposable Bioreactors for Liver Tissue Engineering. Adv Biochem Eng Biotechnol 2009.

125. Powers MJ, Griffith-Cima L. Motility behavior of hepatocytes on extracellular matrix substrata during aggregation. Biotechnol Bioeng 1996;50(4):392-403.

126. McClelland RE, Coger RN. Use of micropathways to improve oxygen transport in a hepatic system. J Biomech Eng 2000;122(3):268-273.

127. Reed MC, Thomas RL, Pavisic J, James SJ, Ulrich CM, Nijhout HF. A mathematical model of glutathione metabolism. Theor Biol Med Model 2008;5(8):8.